1-1-2013

Preparation, Characterization and Application of Novel Proton Conducting Ceramics

Siwei Wang
University of South Carolina

PREPARATION, CHARACTERIZATION AND APPLICATION OF NOVEL PROTON CONDUCTING CERAMICS

by

Siwei Wang

Bachelor of Science
Xiangtan University, 2006

Master of Engineering
Tongji University, 2009

Submitted in Partial Fulfillment of the Requirements

For the Degree of Doctor of Philosophy in

Mechanical Engineering

College of Engineering and Computing

University of South Carolina

2013

Accepted by:

Fanglin (Frank) Chen, Major Professor

Kenneth Reifsnider, Committee Member

Kevin Huang, Committee Member

Kyle S. Brinkman, Committee Member

Lacy Ford, Vice Provost and Dean of Graduate Studies

ACKNOWLEDGEMENTS

I would like to thank my advisor, Dr. Fanglin (Frank) Chen who brought me to this field and offered his knowledge, experience and his character to guide my study, research and life. These treasures will go with me for the whole life.

I would also like to convey my sincerest appreciation to my thesis committee, Dr. Kenneth Reifsnider, Dr. Kevin Huang, and Dr. Kyle S. Brinkman, for their invaluable advice and continuous help during my Ph.D study.

I would also like to thank the collaborators for their assistance and contributions to my work. In Los Alamos National Laboratory, thanks to Dr. Ming Tang. In Oak Ridge National Laboratory, thanks, to Dr. Ke An. My special thanks to my current and former group members, for their active and valuable contribution and suggestions to my research. Special thanks to Dr. Fei Zhao, who led me the way into the solid oxide fuel cells area.

I finally would like to express my gratitude to my wife Lingling Zhang, who helps me, pushes me, understands me and brought me my little girl Nikki. I am much indebted to these mother and daughter to share with me the hard times. I would also like to thank my parents and parents' in law to bring us up and provided their endless support without any expectations.

Financial support from DOE Nuclear Energy University Programs (NEUP: 09-510 and 10-681), Energy Frontier Research Center: HeteroFoaM (DE-SC0001061), Seaborg Institute for Transactinium Science, Los Alamos National Laboratory are greatly acknowledged.

ABSTRACT

Due to the immediate energy shortage and the requirement of environment protection nowadays, the efficient, effective and environmental friendly use of current energy sources is urgent. Energy conversion and storage is thus an important focus both for industry and academia. As one of the hydrogen energy related materials, proton conducting ceramics can be applied in solid oxide fuel cells and steam electrolysers, as well as high temperature hydrogen separation membranes and hydrogen sensors. For most of the practical applications, both high proton conductivity and chemical stability are desirable. However, the state-of-the-art proton conducting ceramics are facing great challenges in simultaneously fulfilling conductivity and stability requirements for practical applications. Consequently, understanding the properties for the proton conducting ceramics and developing novel materials that possess both high proton conductivity and enhanced chemical stability have both scientific and practical significances.

The objective of this study is to develop novel proton conducting ceramics, either by evaluating the doping effects on the state-of-the-art simple perovskite structured barium cerates, or by investigating novel complex perovskite structured $Ba_3Ca_{1.18}Nb_{1.82}O_{9-\delta}$ based proton conductors as potential proton conducting ceramics with improved proton conductivity and enhanced chemical stability. Different preparation methods were compared, and their influence on the structure, including the bulk and grain boundary environment has been investigated. In addition, the effects of

microstructure on the electrical properties of the proton conducting ceramics have also been characterized. The solid oxide fuel cell application for the proton conducting ceramics performed as electrolyte membranes has been demonstrated.

TABLE OF CONTENTS

LIST OF TABLES

LIST OF FIGURES

CHAPTER 1

INTRODUCTION

1.1 MOTIVATION

Unlike polymer proton exchange membranes (PEM) and acid fuel cells that operate at low to intermediate temperature and use precious metal as electrode metal electrode catalyst, proton conducting ceramics can be used as high temperature range, and thus non-precious metal electrode and ceramic electrodes can be used. The proton conducting ceramics have the potential to be applied in high temperature hydrogen separation membranes and hydrogen pumps, proton conducting solid oxide fuel cells, steam electrolysers, and other proton related applications. For the application in high temperature hydrogen separation membranes, they can be employed into the field of the removal of tritium (usually accomplished at low temperatures through tritium permeable membrane or hydrogen isotope getters) from the high temperature gas stream at elevated temperatures (usually 850-900^{o}C) in order to subsequently make use of this heat in downstream processing. For the application of proton conducting solid oxide fuel cells, water forms and leaves the system on the side exposed to air, as opposed to the traditional SOFCs, where water forms on the fuel side, and consequently dilutes the fuel. In addition, the proton conductors possess lower activation energy and higher conductivity at intermediate temperature ranges compared with traditional oxide ion conductors, thus enabling them to be applied as intermediate temperature solid oxide fuel cells (IT-SOFCs)

to lower the operating temperature and thus save the cost and enhancing the durability and reliability of SOFC systems [1]. For the application of steam electrolysers, similar as proton conducting SOFCs, solid oxide electrolysis cells (SOECs) using proton-conducting electrolyte can produce pure and dry hydrogen on the hydrogen electrode, a significant advantage compared with those using oxygen-ion-conducting electrolytes where hydrogen is produced concurrently with steam requiring further drying steps [2].

The state-of-art proton conducting ceramics are barium zirconate cerate based solid solutions. Such proton conductors encounter a dilemma that a compromise should be reached between the conductivity and the stability; $BaCeO_3$-based proton conductors have demonstrated high conductivity, while $BaCeO_3$ has relatively low chemical stability in water and CO_2 atmospheres. $BaZrO_3$-based proton conductors show good chemical stability but the total conductivity is relatively low [3, 4]. In field applications both high proton conductivity and structural stability are urgently required. Consequently, understanding the two-folded properties for the proton conductors, and thus developing novel proton conducting ceramics which possess both high proton conductivity and enhanced structural stability, is an active area of research.

1.2 RESEARCH OBJECTIVES

In this thesis, two strategies have been tried to develop novel proton conducting ceramics. Firstly, we focused on the simple perovskite structured barium cerates, which possess the highest conductivity values. The impact of A site doping on the conductivity and stability for $BaCeO_3$ based materials has been investigated. $Ba_{1-x}Sr_xCe_{0.8}Y_{0.2}O_{3-\delta}$ with x varying from 0 to 1 prepared by a modified Pechini method and were investigated as

potential high temperature proton conductors. The B site co-doping method was then chosen to search novel simple perovskite structured high temperature proton conductors. Novel proton conductor $BaCe_{0.7}Zr_{0.1}Y_{0.1}Yb_{0.1}O_{3-\delta}$ has been prepared by a modified Pechini method and characterized as electrolyte for intermediate temperature solid oxide fuel cells. The sinterability and microstructure evolution of this material and the correlation between the sintering mechanism and the electrical conductivity was also investigated.

Secondly, novel double perovskite structured proton conducting ceramics based on $Ba_3Ca_{1.18}Nb_{1.82}O_{9-\delta}$ have been investigated as potential candidates which possess both high conductivity and structural stability. The effects of Ce doping on the Ca and Nb ions in complex perovskite $Ba_3Ca_{1.18}Nb_{1.82}O_{9-\delta}$ (BCN18) proton conductor have been evaluated. Further, complex-perovskite structured $Ba_3Ca_{1.18}Nb_{1.82-x}Y_xO_{9-\delta}$ were investigated as potential intermediate temperature proton conductors with improved conductivity and enhanced stability.

On the other hand, it is widely known that microstructure of the ceramics has significant impact on the performances. In many cases the mechanical and electrical properties can be readily modified just by altering the grain size distributions without changing the composition of the ceramics [5-7]. Ultra-fine grained dense proton conducting ceramics have been successfully prepared via a two-step sintering method. The effect of microstructure on the electrical properties has been evaluated. In addition, the two-step sintering method has been applied to co-sinter an anode-electrolyte bi-layer to fabricate proton conducting solid oxide fuel cells.

1.3 DISSERTATION STRUCTURE

Chapter 2 provides the background overview of the proton conducing materials. Their crystal structures and conduction mechanism is discussed. The most recent progresses on the development of proton conducting ceramics are reviewed.

Chapter 3 investigates the feasibility of the preparation of simple perovskite $BaCeO_3$ based and $Ba_3Ca_{1.18}Nb_{1.82}O_{9-\delta}$ based proton conducting ceramics via various methods. Their phase structures and microstructure evolutions have been studied.

Chapter 4 studies the corresponding the electrical conductivity, including grain and grain boundary conductivity, the chemical stability and the thermal expansion coefficient of the samples. Parameters that affect the conductivity and the discussion about chemical stability are presented.

Chapter 5 demonstrates the application of selected proton conducting ceramics as electrolyte membranes as solid oxide fuel cells. A Two-step sintering method is applied to co-sinter an anode-electrolyte bi-layer to fabricate proton conducting solid oxide fuel cells with improved electrochemical performance.

Chapter 6 summarizes the work we have done and proposes the possible recommendations for the future work.

CHAPTER 2

BACKGROUND

Literally a proton conductor is a material that can convey protons from on site to the other. Based on the different operating temperatures, we can categorize the proton conductors into low temperature proton conductors (operating at 20-120^{o}C), intermediate temperature proton conductors (operating at 120-250^{o}C), and high temperature proton conductors (500-800^{o}C). Among the low temperature proton conductors the Nafion is briefly introduced. As to the intermediate temperature proton conductors, the solid acid sulfates and selenates are introduced. We focused on the high temperature proton conducting ceramics and their structures, the proton conducting mechanisms and the development status of the high temperature proton conducting ceramics are introduced.

2.1 LOW TEMPERATURE PROTON CONDUCTORS

The classic low temperature proton conductor is the sulfonized Teflon (Nafion), which are primarily used as electrolyte membranes for Proton exchange membrane (PEM) fuel cells which are typically run at 20-120^{o}C. The Nafion can attract water from anode combined with proton, forming hydronium, H_3O^+, which thus transports from anode to cathode. As a consequence, the water molecules will be dragged form anode to cathode. The backbone of the Nafion polymer possess the extreme hydrophobicity, while the terminal sulfonic acid function show the extreme hydrophlicity. In the presence of water,

the hydrophilic part of the structure is hydrated. The hydrophobic part provides good mechanical stability while the hydrated hydrophilic domains provide the very high proton conductivity.

Since the proton conductivity is dependant on the hydration of $–SO_3H$ function group, the ptoton conductivity is thus very much depends on the presence of water. Thus for the application of the PEM membranes, the manipulation of water control is of crucial importance to the function system. This water control system is thus increase the system cost and decrease the system mobility [8].

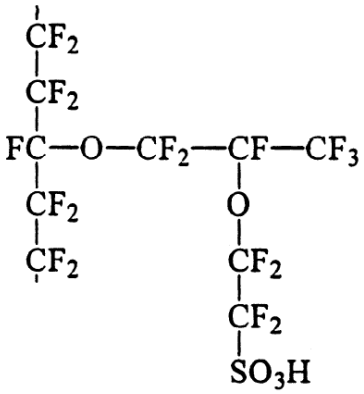

Figure 2.1The molecular structure of Nafion [8].

The Proton transport in Nafion primarily is “vehicle” mechanism. Protons on the -SO_3H (sulfonic acid) groups "hop" from one acid site to another. There is also water in the middle region of the pores, where the proton transport is predominantly via the Grotthuss mechanism [9]. The advantages for PEM fuel cells are clear: it runs in low temperature, showing good start-stop and cycling capability, and the sealing, assembly and handling is less complex in low temperature. The low-temperature operation is suitable for transportation application. However, the most challenging problem for PEM

fuel cell is that it needs precious metal catalyst to act as electrode, such as Pt. It has low tolerance to CO in the fuel stream. The future research and design directions may be in the areas of non precious metal catalyts, new electrolyte membrane with less active water management and hydrogen storage and hydrogen infracture.

2.2 INTERMEDIATE TEMPERATURE PROTON CONDUCTORS

Some proton-conducting solid acid compounds show proton conduction with proton charge carriers (H_3O^+, $H_4PO_4^+$, H_2PO4^-), their dynamics being essential for the diffusivity of such defects. Haile's group published a series of papers introducing the solid acid such as $CsHSO_4$, $CsHSeO_4$, CsH_2PO_4, etc., which exhibit super-protonic phase transitions at slightly elevated temperatures. $CsHSO_4$, for example, transforms at 140℃ into a super-ionic phase in which both protons and oxygen atoms partially occupy many sites. At the transition, the conductivity jumps by several orders of magnitude [10].

Haile's group demonstrated the first fuel cell based on a solid acid in 2001 [10], using the electrolyte $CsHSO_4$. In 2003 they reported solid acid fuel cells based on CsH_2PO_4 as the electrolyte which can perform stably for over one hundred hours of continuous operation [11], and a power density of over 400 mW cm^{-2} can be obtained.

The solid acid fuel cells have several advantages over the PEM fuel cells. First and most importantly is that the anhydrous proton transport in solid acids eliminates the need for auxiliary humidification equipment. Secondly the complete impermeability of the solid acid to H_2 and O_2 results in measurably higher open circuit voltages. A cell made of a $CsHSO_4$ electrolyte membrane operating at 150-160 ^oC in a H_2/O_2 configuration exhibits an open circuit voltages of 1.11V [10]. Also the complete

impermeability to methanol makes possible the operation of high efficiency direct methanol fuel cells and the higher temperature operation leads to greater effectiveness of the Pt catalyst [12]. Fig. 2.2 shows the conductivities of selected solid acids. It can be seen that they show s super-protonic transition characterized by an increase in conductivity by several orders of magnitude over a relatively small temperature range caused by phase transitions.

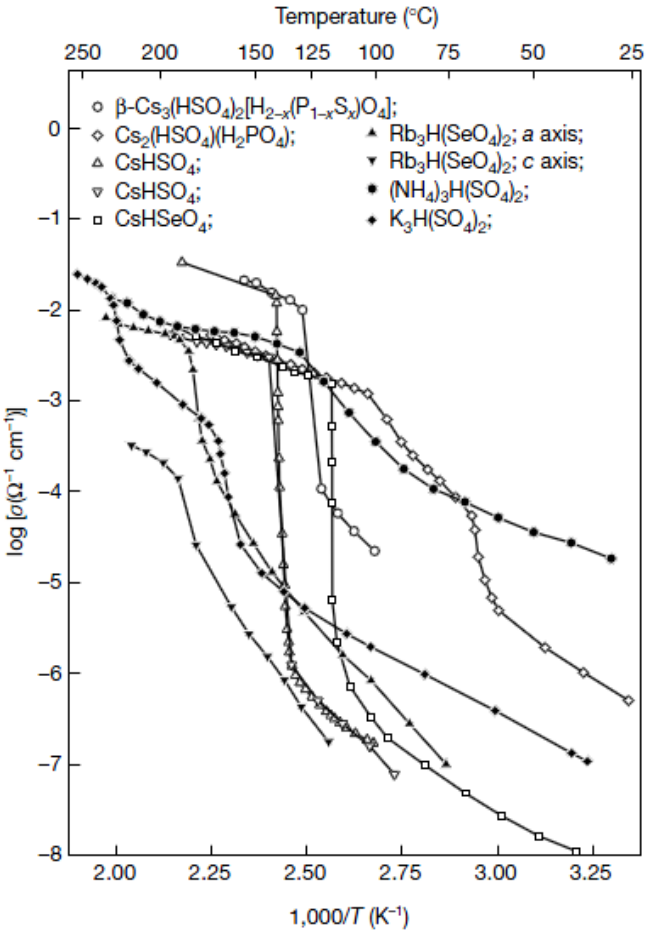

Figure 2.2 The conductivities of selected solid acids [10].

2.3 HIGH TEMPERATURE PROTON CONDUCTING CERAMICS

Unlike low temperature proton conductors that usually are organic proton permeation membranes (such as Nafion), and intermediate temperature proton-conducting solid acid, high temperature proton conductors are proton conducting ceramics in which the protons are transported through protonic defect diffusions. They can be used in the applications such as high temperature separation membranes, solid oxide fuel cells and steam electrolysers [2]. The ceramic proton conductors possess low activation energy and high proton conductivity at intermediate temperature zone (500-700^{o}C), which enables a reduced operating temperature for ceramic proton conducting devices, potentially lowering the cost and enhancing the durability and reliability of the systems.

2.4 STRUCTURES OF PROTON CONDUCTING CERAMICS

2.4.1 Simple perovskite structure

Many high temperature proton conductors possess ABO_3 perovskite structure. In an ideal perovskite structure, the A and O have comparable size and form AO_3 closed packed layers, with B atoms occupying 1/4 of the octahedral sites. It can also be normally viewed as BO_6 shared octahedra with the A atoms in the middle of 8 octahedra. Fig. 2.3 shows the crystal strucuture of a typical proton conductor $BaCeO_3$. In order to achieve appreciable proton conductivity, aliovalent ions are typically doped into the B-sites in the simple perovskite ABO_3 structure, such as Fe doped $KaTaO_3$ and Yb doped $SrZrO_3$ [13, 14]. Among them, the doped barium cerates, $BaCe_{1-x}A_xO_{3-\delta}$ (A = Y^{3+}, In^{3+}, rare-earth ions such as Nd^{3+}, Sm^{3+}, Gd^{3+}, Eu^{3+} and Yb^{3+}, $\delta = x/2$) have exhibited particularly high

proton conductivity [15-21]. As shown in Fig. 2.3, for a typical $BaCe_{1-x}Y_xO_{3-\delta}$ proton conductor, x percent of Ce is substituted by Y. Normally, the optimum doping amount should be less than 20% [22].

The ilmenite structure has the same composition as the perovskite structures. In ABO_3 composition, If the ionic sizes of A and B are small compared with O^{2-}, both A and B will fit into the oxtahedral sites in the closed packed layers of O^{2-}, forming ilmenite structure, such as $FeTiO_3$. Goldschmidt perceived a tolerant factor t to predict which structure would form with different ionic sizes for an ABO_3 structructure:

$$t = \frac{r_A + r_O}{\sqrt{2}(r_B + r_O)} \qquad (2\text{-}1)$$

where r_A, r_B, and r_O are the ionic radii of A, B and O respectivly. If $0.78<t<1.05$, the perovskite structure often forms, while for $t \geq 1.05$, the sesquioxide structures form [23].

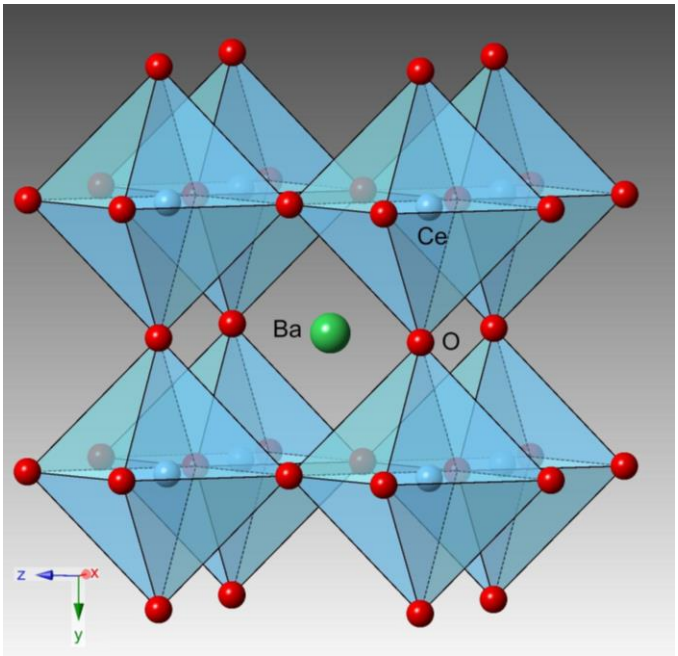

Figure 2.3 Crystal structure of $BaCeO_3$. For $BaCe_{1-x}Y_xO_{3-\delta}$, x percent of Ce is substituted by Y.

2.4.2 Complex perovskite structure

With respect to the "simple perovskite", there are complex perovskites which may also show proton conduction with the existence of oxygen ion defects. In the complex perovskites, the B sites are usually occupied by two or more different elements and can be categorized by the differences of B site cations' valences. The first category of these complex perovskites is the $A_2(B'B'')O_6$ perovskite structure. In this case the B' and B'' ions have charges 3+ and 5+, respectively [24]. While in the second category B' and B'' ions are 2+ and 5+, respectively, forming $A_3(B'B_2'')O_9$ formula, such as $Sr_3CaTa_2O_9$ based materials [25-27]. To become proton conductors they should be taken off stoichiometry to create negative charges which oxygen vacancies or protons can compensate. Take the latter case for example, the formula can be written as $A_3B'_{1+x}B''_{2-x}O_{9-\delta}$. The most famous example is $Ba_3Ca_{1.18}Nb_{1.82}O_{9-\delta}$ (BCN18), in which Ca^{2+} ions are off stoichiometry by 18%, which showed almost pure proton conduction in reduced atmospheres [24, 28-30]. BCN18 shows conductivity of 1.5×10^{-3} S cm^{-1} at 550 ^{o}C in wet H_2 in our test. The choice of 1.18 for Ca portion in BCN18 is based on the B site 1:1 mixed with random ordering status for BCN18 complex structure, which is more favored on conductivity compared with pure $Ba_3CaNb_2O_9$ which shows completely 1:2 ordered structure [31]. For 1:1 type orderd complex perovskite, alternate (111) planes of the elementary perovskite structure consit of B' ions and of B'' ions. The result is a larger cubic unit cell in which the B' and B'' ions are in a NaCl-like arrrangement. In the case of 1:2 type compounds are fully ordered, the B ions are distributed on three (111) planes of the elementary cubic structure with one plane containing B' ions and the other two containing B'' ions, with a –B'–B''–B''– stacking sequence [32]. Fig. 2.4 is a typical

complex perovskite structured $Ba_3CaNb_2O_9$, where 1/3 of Nb sites (blue polyhedral) are occupied by Ca. Compared with simple structured perovskites, where the B site-ions are randomly ordered and by applying the structure factor master equation that some diffraction peaks would dissappear, for the complex structured perovskites, due to the ordering on cation ions, it shows intensified XRD peaks.

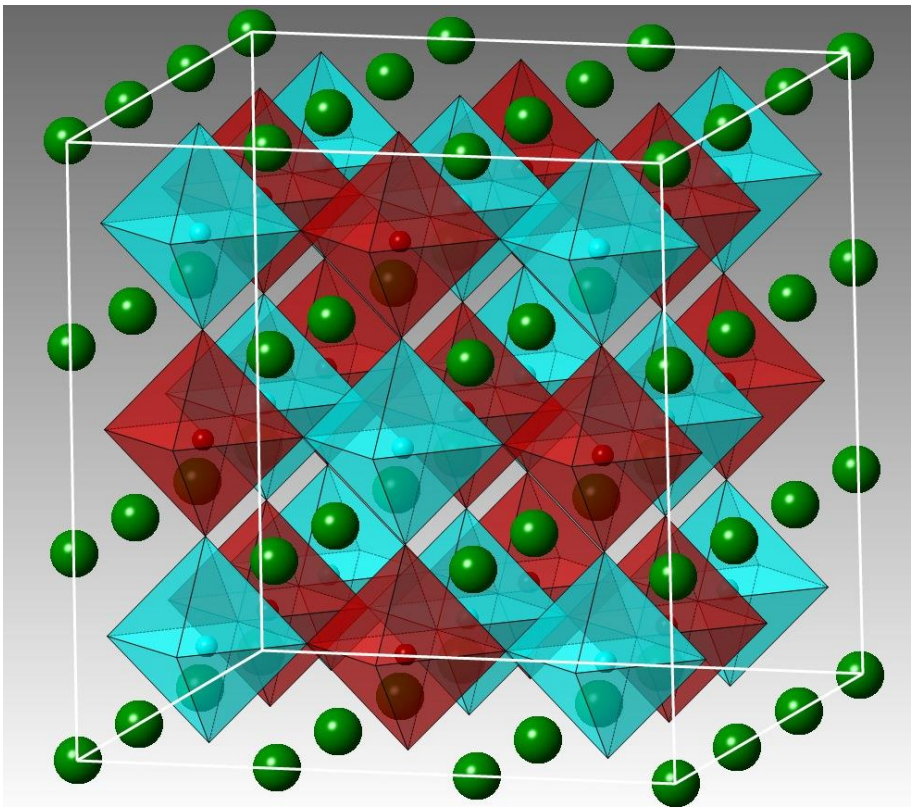

Figure 2.4 Crystal structure of $Ba_3CaNb_2O_9$, where 1/3 of Nb sites (polyhedrals) are occupied by Ca. Green balls: Ba; blue octahedrals: Nb; Red octahedrals: Ca/Nb composite; Oxygen is not shown here for clarity.

2.4.3 Other structured proton conducting ceramics

There are perovskite related compounds with general formulae $Me_4(Me_2'M_2^{5+})O_{11}$ (elpasolite) and $Me_6M_2^{5+}O_{11}$ (cryolite), where Me is alkaline-earth,

M^{5+} is either Nb or Ta. In both cases the oxygen sites are only partially filled in the stoichiometric composition, leaving oygen vacancies. Examples include $Sr_{6-2x}Ta_{2+2x}O_{11+3x}$ and $(Ba_{1-x}Ca_x)_6Nb_2O_{11}$ [33, 34].

Brownmillerite is also belonged to perovskite-related structure, example of which is the proton conductor $Ba_2In_2O_5$. The brownmillerite structure can be viewed as a perovskite-type structure in which one sixth of the oxide ions are missing. At room temperature, the oxygen vacancies order in alternating perovskite layers, with the associated trivalent cations exist in both tetrahedral and octahedral coordination, resulting in orthorhombic symmetry [35]. It is initially been proposed as an oxide-ion conductor, with temperature above 900^{o}C showing higher oxide-ion conductivity than YSZ [36]. However, the presence of intrinsic oxygen vacancies also means that it may support proton conduction. $(Ba_{1-x}La_x)_2In_2O_{5+x}$ has shown increased proton conduction with increasing La content [37]; $Ba_2(In_{1-x}Ti_x)_2O_{5+x}$ system aslo show promising proton conductivity [38].

Other high temperature proton conductors include phosphates without structural protons such $LaPO_4$. In this phosphate systems, the structure consists of chains of corner-sharing PO_4 tetrahedra separated by layers of rare earth. With Ca and Sr doped into La sites, it exhibits predominantly protonic conductivity up to 800^{o}C. However, the conductivity is relatively low, with values of 6×10^{-5} S cm^{-1} and 3×10^{-4} S cm^{-1}, respectively [39]. In these materials, water vapor enter into the crystals to create proton condution, in the form of extrinsic defects, compensating the acceptor dopants and replaceing the intrinsic positive defects [35]. Several acceptor doped rare-earth orthoniobates and orthotantalates with formula $Re_{1-x}A_xMO_4$, where Re = La, Gd, Nd, Tb,

Er or Y; M = Nb or Ta; A = Ba, Sr or Ca; x = 0.01-0.05, also show pure proton conduction up to 700^{o}C, with conductivity values of the order of 10^{-3} S cm^{-1}. This class of materials is monoclinic fergusonite-type structure at low temperatures, followed with a phase change into tetragonal scheelite-type structure at high temperatures. The transistion temperature varies with chemical compositions [40]. Of the compositions investigated, $La_{0.99}Ca_{0.01}NbO_{4-\delta}$ shows the highest conductivity among the orthoniobates and orthotantalates. Some oxide ion conductors also exhibit proton condution in reduced atmospheres or in low temperatures. $La_{1-x}Ba_{1+x}GaO_{4-x/2}$, which was first reported as rapid oxide-ion conductor, also show significant proton conductivity [41]. The proton conductivities of the gallate-based compouds are among the highest level at intermediate temperatures, for example, exceeding that of Sr doped $LaPO_4$. However, the conductivity is still far less than $BaCeO_3$ based systems by almost one order.

2.5 PROTON CONDUCTION MECHANISM IN PEROVSKITES

The commonly accepted conducting mechanism is the Grotthuss mechanism. The proton transfer is conducted by OH- groups' reorientation and hopping from OH- to adjacent oxide ion, thus only the protons show long range diffusion [42]. Another explanation with minor difference is the rotational diffusion of the protonic defect and proton transferring between neighboring oxide ions (shown in Fig. 2.5) [1]. The first requires the breaking of OH- bond, showing higher activation energy than the latter. From defect chemistry standpoint, the formation of proton conducting species is originated from the following Equation

$$H_2O_{(g)} + O_O^{\times} + V_O^{\bullet\bullet} = 2OH_O^{\bullet} \qquad (2\text{-}2)$$

From Equation (2-2), we can see that if the partial pressure of water decreases, the equilibrium will shift to left, thus the $OH_O^{\bullet}$ concentration will decrease, leading to the decrease in proton conductivity. Under high oxygen partial pressure, reactions (2-3) and (2-3) will be favored:

$$V_O^{\bullet\bullet} + \frac{1}{2}O_2 = O_O^{\times} + 2h^{\bullet} \qquad (2\text{-}3)$$

$$2OH_O^{\bullet} + \frac{1}{2}O_2 = 2O_O^{\times} + H_2O + 2h^{\bullet} \qquad (2\text{-}4)$$

Consequently, increase in the oxygen partial pressure will result in consumption of oxygen vacancies and OH- groups, leading to a decrease in proton conductivity and/or an increase in electronic conductivity. Reaction (2-2) is exothermic, and the equilibrium shifts to left with increased temperature. Thus the proton conductivity will typically decrease with the increase in the sample temperature. The phenomenon happens drastically especially at temperatures higher than 500^{o}C, above which water in the crystal evaporates.

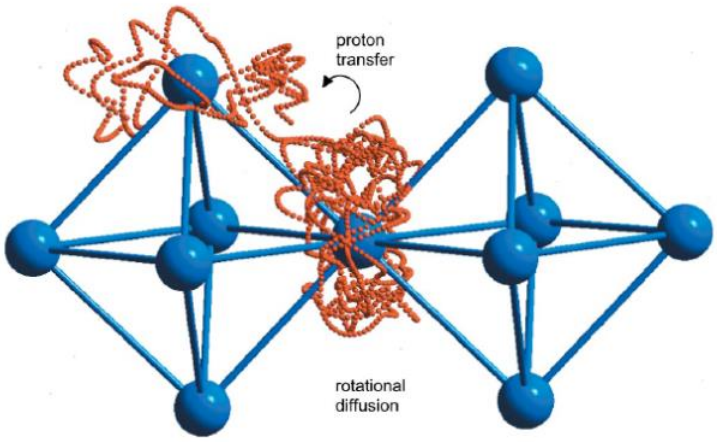

Figure 2.5 Rotational diffusion and proton transfer model proposed by K.D. Krueur [1].

The major difference between the proton transport in perovskite-structured oxides and that of Nafion is that in perovskite-structured oxides, the oxide ions associated with OH- groups do not move; while that in Nafion, the SO_3-group moves from one acid site to another to transport protons, like a vehicle.

The activation energy is an indication of the conduction mechanism and behaviors. The activation energy can be calculated through the Arrhenius Equation

$$\sigma T = A\exp(-\frac{E_a}{RT}) \qquad (2\text{-}5)$$

where A is the pre-exponential factor proportional to the charge carrier concentration, and E_a is the activation energy associated with the transport mechanism and can be determined from the slope of the Arrhenius plot. It is believed that the activation energy for electron conduction is around 0.1 eV; for proton conduction the activation energy is around 0.5 eV, For oxide ion conduction it should be around 0.8 eV, while for electronic hole conduction, the activation energy is about 1 eV. However, the activation energy can be influenced by several factors not only by major charge carriers, but also by the phase transitions, or even sample degradation [43]. In different structures, the activation energies are different even it is believed they have the same conducting mechanism. The activation energy is also correlated with the host and dopant cations and it was concluded that the activation energy for conduction should be minimum when the host and dopant cations have similar ionic radii [44]. Even in the same structure, the small difference in composition will result in deviation on activation energy. Fig. 2.6 shows that the activation energy is dependent of Ba content in $Ba_xCe_{0.90}Y_{0.10}O_{3-\delta}$ system [45].

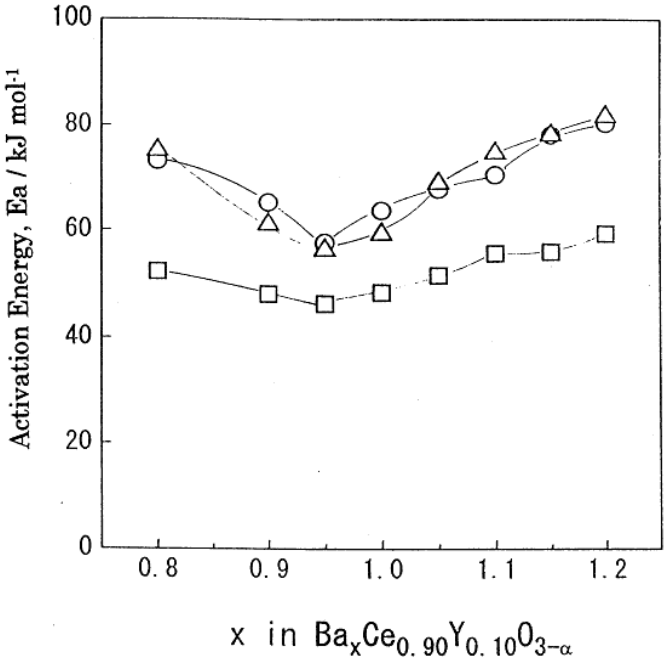

Figure 2.6 Dependence of apparent activation energy (600–1000°C) on Ba content, in (○) dry air, (Δ) wet air and (□) wet H_2, respectively [45].

2.6 DEVELOPMENT STATUS OF HIGH TEMPERATURE PROTON CONDUCTING CERAMICS

Ever since Iwahara reported the proton conductivity of $SrCe_{0.95}Yb_{0.05}O_{3-\delta}$ in 1981 [46], the proton conducting ceramics have been under widely investigations. Among them, Y^{3+} doped $BaCeO_3$ possesses the highest level of proton conductivity in acceptor-doped simple perovskite structured oxides [47, 48]. For example, Gd-doped $BaCeO_3$ exhibited a conductivity of 0.05 S cm^{-1} at 600°C in wet air [48]. However, $BaCeO_3$ (similar with $SrCeO_3$ and $CaCeO_3$) is thermodynamically not stable in water and CO_2 at specific temperature ranges:

$$BaCeO_3 + H_2O \rightarrow Ba(OH)_2 + CeO_2 \qquad (2\text{-}6)$$

$$BaCeO_3 + CO_2 \rightarrow BaCO_3 + CeO_2 \qquad (2\text{-}7)$$

In this case, people have to either avoid the contact with water and/or CO_2, or to use them in temperature ranges where the reaction is not likely to happen.

$BaZrO_3$ based materials are thermodynamically much more stable than $BaCeO_3$ based materials; they also show high bulk proton conductivity [1]. However they are difficult to sinter and show low grain boundary conductivity, which prevents their applications. Haile's group first published the reactive sintering method to prepare low temperature sintered $BaZrO_3$ with large grain-sizes [49]. They demonstrate a fabrication protocol based on the sol-gel synthesis of nanocrystalline precursor materials and reactive sintering that result in large grained, polycrystalline $BaZr_{0.8}Y_{0.2}O_{3-\delta}$ with a total conductivity of around 0.01 S cm^{-1} at 450^{o}C. O'Hayre's group also published several papers on low temperature sintering of $BaZrO_3$ with Ni doping and reactive sintering [50, 51]. In 2009, Traversa's group reported high proton conductivity in $BaZr_{0.8}Y_{0.2}O_{3-\delta}$ thin film prepared by pulsed laser deposition on different single-crystalline substrates. The highly textured, epitaxially oriented BZY films showed the largest proton conductivity ever reported for BZY samples of 0.11 S cm^{-1} at 500^{o}C [52]. They claimed the high conductivity is attributed to the absence of blocking grain boundaries. Although their results was doubted by many scientists such as Krueur, J.T.S. Irvine and Haile, the research on $BaZrO_3$ based proton conducting ceramics and their application on solid oxide fuel cells has again become a hot topic. Traversa's group have reported a series of results on the preparation of low temperature sintering of $BaZrO_3$ based materials and fabrication of $BaZrO_3$ based solid oxide fuel cells [48, 49]. Fuel cells based on a 20 μm BZY electrolyte has been reported to show a peak power density of 169 mW cm^{-2} at 600^{o}C [53].

$Ba(Ce,Zr)O_3$ solid solution based materials have been receiving much attention since they balance the conductivity and stability for $BaCeO_3$ and $BaZrO_3$ based materials. As early as 1999, Haile's group investigated compounds of general formula $BaCe_{0.9-x}Zr_xM_{0.1}O_{3-\delta,}$ where M was Gd or Nd and *x* ranged from 0 to 0.4. For the Nd-doped system, compositions with *x*=0.2 or higher did not react with CO_2, whereas for the Gd-doped system, the composition with *x*=0.4 did not react. The introduction of Zr also led to a decrease in conductivity and an increase in the activation energy for proton transport [54]. The chemical stability of $Sr(Ce_{1-x}Zr_x)_{0.95}Yb_{0.05}O_{3-\delta}$ ceramics against CO_2 attack has also been reported to improve with the increase in zirconium content: with Zr content increased to x=0.4, the X-ray diffraction pattern of the ceramic did not change after the sample was exposed to 100% CO_2 atmosphere at 900^{o}C for 1h [55]. Z. Zhong reported that $BaCe_{0.7}Zr_{0.2}Y_{0.1}O_{3-\delta}$ will discompose when either treated in boiling water for 6 h or held in carbon dioxide atmosphere for 2 h at 900^{o}C [56]; even for $BaCe_{0.3}Zr_{0.5}Y_{0.2}O_{3-\delta}$, impurity phase is formed after exposure to CO_2 at 900^{o}C for 3h [57]. $BaCe_{0.45}Zr_{0.45}Sc_{0.2}O_{3-\delta}$ has been reported to be stable in pure CO_2 up to 900^{o}C, but the total conductivity is relatively low, only 4.49×10^{-4} S·cm^{-1} at 600^{o}C in air [58].

For some applications that are not in harsh environment, however, $Ba(Ce,Zr)O_3$ based materials are kinetically stable and show high conductivity. M. Liu's group reported $BaZr_{0.1}Ce_{0.7}Y_{0.2}O_{3-\delta}$ (BZCY) possess a conductivity of 0.03 S cm^{-1} at 700 ^{o}C in wet air while maintaining a pure phase perovskite structure under H_2 with 50 vol% H_2O at 750^{o}C for 300 h [42]. In 2009 they reported $BaZr_{0.1}Ce_{0.7}Y_{0.1}Yb_{0.1}O_{3-\delta}$ (BZCYYb), which possesses higher conductivity than BZCY and remarkable stability properties. BZCYYb prepared by solid state reaction method, showed a conductivity of around 0.05

S cm^{-1} at 700°C in wet oxygen, while it remained stable after exposed to H_2 with 50 vol % H_2O or H_2 with 50 vol % CO_2 at 750°C for 300 h [59]. Fig. 2.7 shows the Conductivities of BZCYYb, BZCY, $Gd_{0.1}Ce_{0.9}O_{2-\delta}$ (GDC) and $Y_{0.15}Zr_{0.85}O_{2-\delta}$ (YSZ) measured in wet oxygen. It exhibits high ionic conductivity at intermediate temperatures (500 °to 700 ℃), which is advantageous for the application as electrolyte membrane materials for solid oxide fuel cells to lower their operation temperature. Also, its ability to resist deactivation by sulfur and coking suggest the material may also be used as a catalyst for reforming of hydrocarbon fuels and for removal of fuel gas contaminants such as sulfur [59].

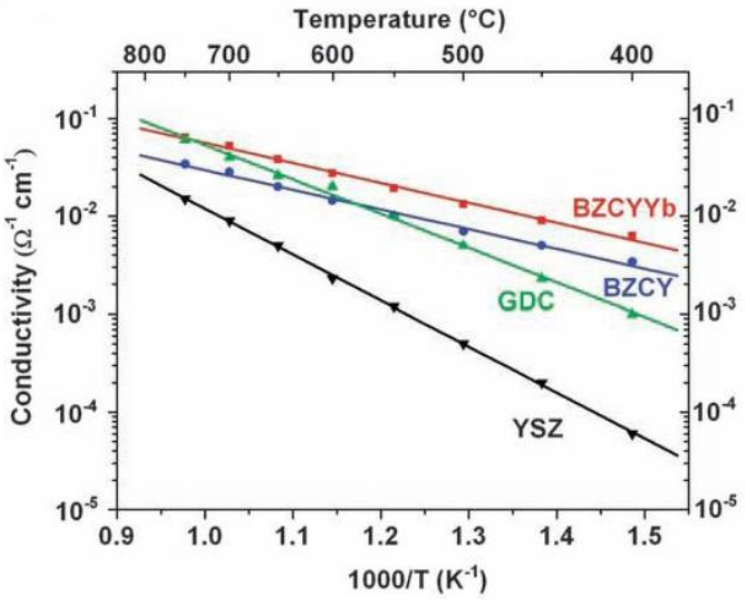

Figure 2.7 Conductivities of BZCYYb, BZCY, GDC, and YSZ as measured in wet oxygen [59].

CHAPTER 3

PREPARATION OF PROTON CONDUCTING CERAMICS

3.1 BACKGROUND

For the structure-property relationships of the materials, the preparation of the material is the first step and of crucial importance to affect the subsequent materials structures as well as the consequent properties. It is known that the electrical properties of the high temperature perovskite type protonic conducting ceramics are greatly influenced by the preparation methods, crystal structure and microstructure of the materials [5-7, 60-62]. In general, proton conductors are conventionally prepared by solid state reaction route, in which different metal oxides and/or carbonates mixed in stoichiometric ratio to yield a given composition are ball-milled, ground and then fired at high temperatures. In order to make the components homogeneously distributed, it is good experience to press the powders into pellets for calcination to maximize the contact areas and do the calcination for multiple times. The solid stare reaction method is simple, easy and reliable. However, such a synthesis method may lead to the following disadvantages: (1) a micro-homogenous phase structure is very difficult to obtain due to large and strongly bonded powder agglomerates; (2) contamination can hardly be avoided during milling and grinding, resulting in detrimental effects on the electrical conductivity; and (3) the mechanically ground mixture requires prolonged calcination at high temperatures (usually >1400 ℃), which is undesirable in the fabrication of dense fine grained ceramics due to the promotion of abnormal crystallite growth. Compared with solid state reaction

method, the wet chemistry method is an alternative to prepare metal-oxide compounds such as the modified Pechini method using a chelating wet chemistry technique and the co-precipitation method to mix the precursors in nano-scale. Compared with the conventional solid-state reaction method to synthesize high temperature protonic conductors, the advantage of a wet-chemistry technique with the help of chelating ligand is that the constituent ions are mixed at the atomic level in the solution so that nano-sized precipitates can be formed. This method will result in fine particles which promote sintering, consequently making it easier to obtain gas-tight samples for different applications. However, the control of the direction of the reactions via wet chemistry method may be difficult due to the existence of extra chemical reactions during the legandation. It is also noted that for some specific materials, the formation of the pure structure is sometimes difficult. For example, $La_{0.8}Sr_{0.2}Ga_{0.83}Mg_{0.17}O_{3-\delta}$ (LSGM) requires a very actuate composition ratios of the reactant, thus the preparation of the LSGM is usually conducted by a solid state reaction methods through rigorous control the reactant oxides [63].

In this chapter we aim to prepare several proton conducting ceramics with various methods, to prove the feasibility of these methods for the preparation of these specific materials, providing that either the materials are new, or these materials are not prepared by the specific method. The phase structures, microstructure morphologies, as well as the sintering behaviors of the prepared materials are investigated.

3.2 EXPERIMENTAL

We aim to prepare several types of proton conducting ceramics with various methods, including the preparation of A site Sr doped $BaCe_{0.8}Y_{0.2}O_{3-\delta}$ by modified Pechini method; the preparation of B site Y and Yb co-doped $BaZr_{0.1}Ce_{0.7}Y_{0.1}Yb_{0.1}O_{3-\delta}$ by Modified Pechini method; A two-step sintering method combined with co-precipitation method has been adopted to prepare ultra-fine grained dense proton conducting ceramics to look into the impact of the ceramics microstructure on the properties and performances. Preparation of Ce doped $Ba_3Ca_{1.18}Nb_{1.83}O_{9-\delta}$ by solid state reaction method, with Ce substituting either in Ca or Nb sites; $Ba_3Ca_{1.18}Nb_{1.82-x}Y_xO_{9-\delta}$ are also prepared by solid state reaction method and the phase structure are studied in detail by neutron diffraction and TEM.

Crystalline phases of the samples were recorded on a X-ray diffractometer (Rigaku, Japan) with graphite-monochromatized CuKa radiation (λ=1.5418 Å) using a scan rate of 5^o min^{-1} in a 2θ range from 20 to 80^o. In situ high-temperature X-ray diffraction study was performed using a hot-stage-equipped Rigaku D/Max 2100 Powder X-ray Diffractometer (Cu Ka radiation). Data were collected at a 0.02◦ step for 2.4 s per step over the 2θ range 10-80^o. Neutron diffraction measurement was conducted in VULAN diffractometer at Spallation Neutron Source in Oak Ridge National Laboratory. The neutron diffraction data were analyzed by the Rietveld method. The X-ray photoelectron spectroscopy (XPS) measurement was employed to obtain the bonding energy spectra of selected elements for the samples using a Kratos Axis Ultra DLD instrument equipped with a monochromated Al Ka x-ray source and hemispherical analyzer. Scanning electron microscopy (SEM, FEI Quanta and XL 30, and FESEM,

Zeiss Ultra) and transmission electron microscopy (TEM, Hitachi H-800, 200 kV, and FEI Tecnai F30 Analytical) were used to characterize the morphology and micro-structural ordering of the samples. The sintering behaviors of the materials were carried out on samples using the same sintering profiles described above by a NETZSCH DIL 402C pushrod dilatometer. Scanning calorimeter (DSC) and thermogravimetry (TG) on a NETZSCH STA 409 CD thermal analyzer was utilized to check the formation evolution of the materials. The porosities of the sintered pellets were quantified by a mercury porosimetry (Autopore IV, Micromeritics) at pressures ranging from 0.5-30000 psi.

3.3 PREPARATION OF $BA_{1-X}SR_XCE_{0.8}Y_{0.2}O_{3-\Delta}$ BY MODIFIED PECHINI METHOD

3.3.1 Introduction

Many published papers have reported on the effect of doping ions into either B site or A site for the ABO_3 structure. Besides the B site doping strategy, the impact of A site doping on the conductivity and stability issues for $BaCeO_3$ based materials have also been reported. The cerate system $BaCe_{0.9}Nd_{0.1}O_{3-\delta}$ has been investigated by Yajima *et al.* by partially substituting Ca for Ba [64]. The oxygen ion conductivity decreased with increasing Ca content although the decrease in proton conductivity was insignificant. Hung *et al*. have recently reported that the chemical stability could be improved by small amount of A site Sr doping on $BaCe_{0.8}Y_{0.2}O_{3-\delta}$ [65]. They reported that $Ba_{0.9}Sr_{0.1}Ce_{0.8}Y_{0.2}O_{3-\delta}$ was more stable than $BaCe_{0.7}Zr_{0.2}Y_{0.1}O_{2.95}$ when exposed to a water vapor-rich environment. However, there seems to be some discrepancies with this conclusion. Regarding the stability test for the $BaCe_{0.7}Zr_{0.2}Y_{0.1}O_{2.95}$ material reported [56], $BaCe_{0.7}Zr_{0.2}Y_{0.1}O_{2.95}$ was treated in boiling water; while the $Ba_{0.9}Sr_{0.1}Ce_{0.8}Y_{0.2}O_{3-\delta}$

material reported by Hung [65] was exposed to a water vapor-rich environment at 80°C. In liquid water, the kinetics of the decomposition of $BaCeO_3$ (doped or undoped) appears to be interface-controlled and is relatively fast. By contrast, in the presence of water vapor, the kinetics appears to be diffusion-controlled and is relatively sluggish [66]. Therefore the different experimental conditions utilized in literature reports on the stability of these materials have resulted in some confusion and a knowledge gap with regards to the stability of cerate perovskites under humid conditions.

This work aims to fill the knowledge gap and attempts to more completely understand the stability and the electrical properties of $(Ba,Sr)(Ce,Y)O_{3-\delta}$ materials. $Ba_{1-x}Sr_xCe_{0.8}Y_{0.2}O_{3-\delta}$ (BSCY, x=0, 0.1, 0.2, 0.5, 1, denoted as BCY, BSCY1, BSCY2, BSCY5 and SCY, respectively) were prepared, the phase structure and chemical stability were investigated, and the electrical conductivities were evaluated in chapter 4. The reactivity with water was evaluated in both liquid and gas phase conditions.

3.3.2 Preparation

The $Ba_{1-x}Sr_xCe_{0.8}Y_{0.2}O_{3-\delta}$ powder was prepared by a modified Pechini method [67]. Starting materials $Ba(NO_3)_2$ (Alfa Aesar, 99.95%), $Sr(NO_3)_2$ (Alfa Aesar, 99%), $Ce(NO_3)_3 \cdot 6H_2O$ (Alfa Aesar, 99.5%) and $Y(NO_3)_3 \cdot 6H_2O$ (Alfa Aesar, 99.9%) were dissolved in deionized water and the nitrate concentration of the metal ions was determined through titration.

Citric acid (Alfa Aesar, 99%) and ethylenediaminetetraacetic acid (EDTA, Alfa Aesar, 99%) were used as chelating and complexing agents. Ammonium hydroxide (Sigma-Aldrich, NH_3 content 28.0 to 30.0%) was added to promote the dissolution of

EDTA in deionized water. The metal precursors were then stoichiometrically added into the chelating and complexing agents with metal nitrates : citric acid : EDTA molar ratio = 1 : 1.5 : 1.2. The solution was stirred at room temperature for 24 h to achieve full complexation, followed by heat treatment in a microwave oven (Oster, Model No. OM0701N8E, output power 800W, 2450Hz) to assist in foaming. After 10 min microwave heat treatment, a batch of dry foam was formed. The dry foam was subsequently fired at 600^{o}C for 4 h in air to remove organic residue, resulting in light-colored powders, followed by calcining at 1100^{o}C for 5 h in air with a heating rate of 3^{o}C min^{-1}. The process is illustrated in Fig. 3.1. The obtained powders were pulverized with 8 wt% polyvinyl alcohol (PVA) binder and pressed into pellets Preunder 400 MPa. The green pellets were sintered at 1500^{o}C for 5 h in air.

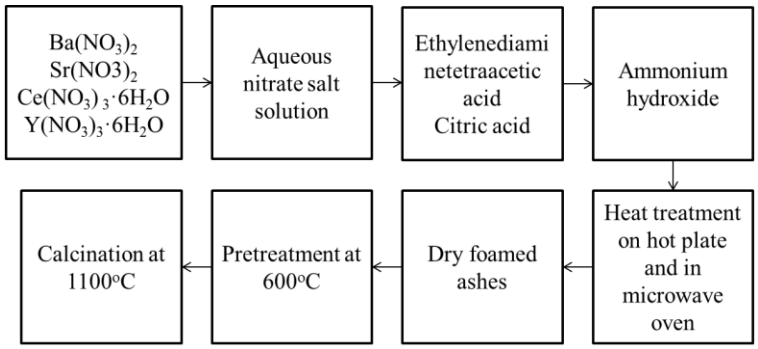

Figure 3.1Modified Pechini procedure for preparation of $Ba_{1-x}Sr_xCe_{0.8}Y_{0.2}O_{3-\delta}$.

3.3.3 Phase structure and morphology revolution

Fig. 3.2 shows the XRD patterns of the BSCY samples sintered at 1500^{o}C for 5 h. It can be seen that a predominant perovskite structure is formed for all the samples. However, secondary phases such as Sr_2CeO_4 and Y_2O_3 appear for higher Sr content since

the solubility limit of Y in $SrCeO_3$ is less than 20% [68, 69]. It is also noted that the XRD peaks split for BCY, probably due to structure changes in the perovskite phase [70]. With the increase in Sr content, the diffraction peaks shifted towards larger diffraction angles indicating a decrease in the lattice parameter. This can be easily understood by the fact that the radius of Sr^{2+} (1.12 Å) is smaller than that of Ba^{2+} (1.35 Å). After substituting Ba^{2+} with Sr^{2+}, the lattice parameter decreases, resulting in shift towards larger diffraction angles.

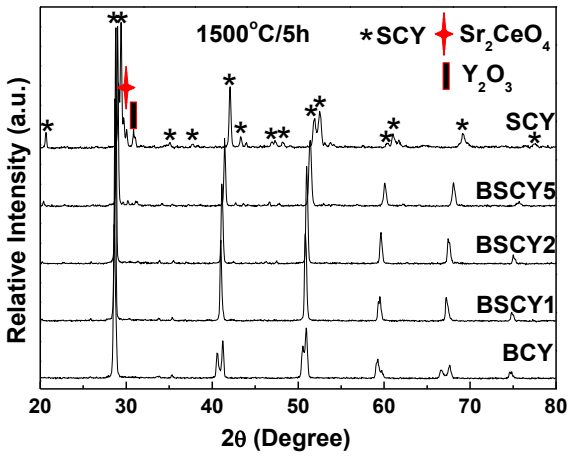

Figure 3.2 XRD patterns of $Ba_{1-x}Sr_xCe_{0.8}Y_{0.2}O_{3-\delta}$ (BSCY, x=0, 0.1, 0.2, 0.5 and 1, denoted as BCY, BSCY1, BSCY2, BSCY5 and SCY, respectively) sintered at 1500°C for 5h in air.

The microstructures of the sintered samples are shown in Fig. 3.3. The graphs marked with "BCY", "BSCY1", "BSCY2", "BSCY5" and "SCY" are the cross-sectional images for the samples. The graph marked with "SCY Surface" is a surface image for SCY sample. It can be seen from the cross-sectional views of the samples that all the sintered samples formed dense structures. Archimedes's water displacement measurements on the sintered disks indicate that all the sintered samples have relative densities greater than 95% of the theoretical values. For sample BSCY5 and SCY, it is

noticed that some small particles with average grain size of about 2 μm exist, indicating the formation of secondary phases. Surface morphology for sample SCY is presented in Fig. 3.3 and EDX patterns for selected area A (representing large grain sizes) and B (representing small grain sizes) are shown in Fig. 3.4 (a) and Fig. 3.4 (b), respectively. It is difficult to identify the highest EDX peak of Sr from that of Y in Fig. 3.4. However, when the relative EDX peak intensity for Sr and/or Y with Ce is compared in Fig. 3.4 (a) and Fig. 3.4 (b), it can be seen that the relative Sr and/or Y content is higher in Fig. 3.4 (b) (small grain sizes) than that in Fig. 3.4 (a) (big grain sizes). Based on the XRD result for SCY, it is reasonable to conclude that the big grains are $SrCe_{0.8}Y_{0.2}O_3$ while the small particles are either Sr_2CeO_4 or Y_2O_3. Similar results also exist in sample BSCY5. The results would suggest that the solubility of Y in $BaCeO_3$ is larger than that in $SrCeO_3$, consistent with previous observations [68, 69].

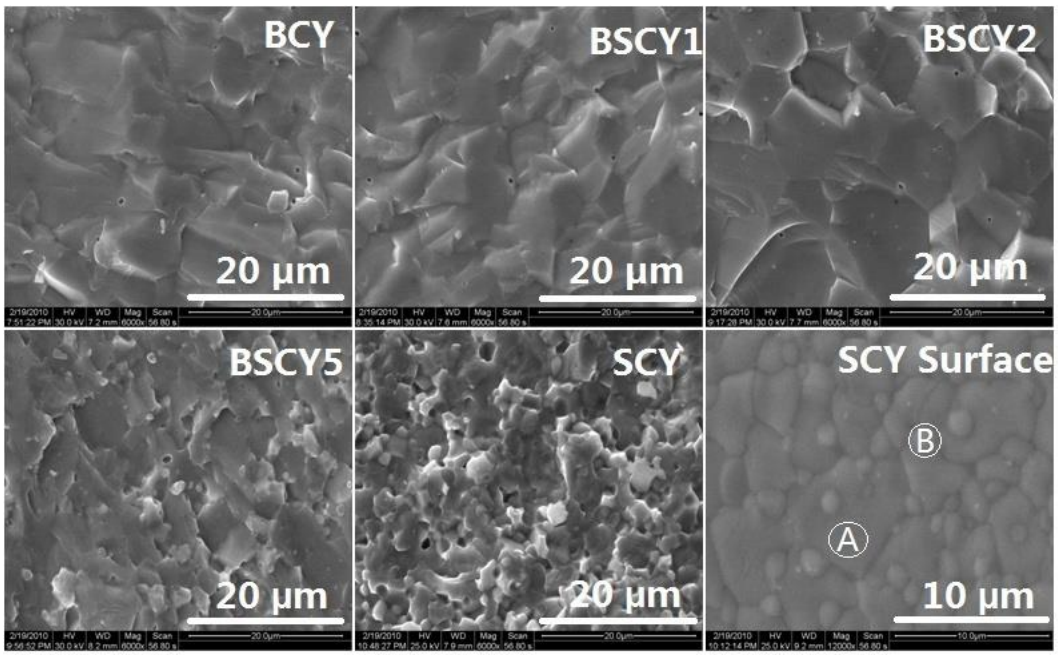

Figure 3.3 Cross-sectional views of the BSCY sample pellets and the surface view of SCY sintered at 1500^{o}C for 5h.

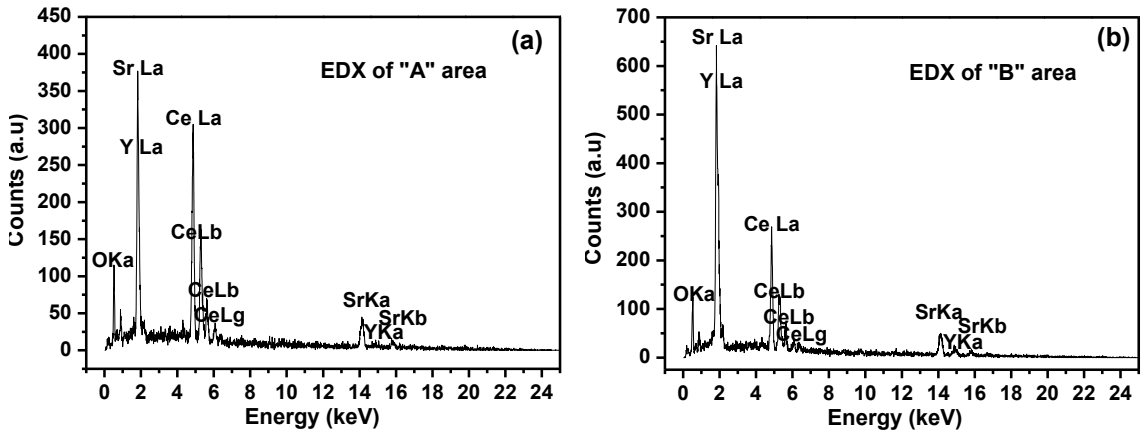

Figure 3.4 EDX patterns for selected areas in SCY Surface shown in Fig. 3.3: (a) EDX of area A (representing large grain sizes); (b) EDX of area B (representing small grain sizes).

3.4 PREPARATION OF $BAZR_{0.1}CE_{0.7}Y_{0.1}YB_{0.1}O_{3-\Delta}$ BY MODIFIED PECHINI METHOD

3.4.1 Introduction

In this part, on the conductivity issue, a "co-doping" strategy has been applied [71]. Barium zirconate and barium cerates containing multiple dopants have been demonstrated to possess higher conductivity than the ones containing only a single dopant [72-74]. It has been recently reported that the conductivity of $BaZr_{0.1}Ce_{0.7}Y_{0.1}Yb_{0.1}O_{3-\delta}$ is higher than that of $BaZr_{0.1}Ce_{0.7}Y_{0.2}O_{3-\delta}$ and $BaZr_{0.1}Ce_{0.7}Yb_{0.2}O_{3-\delta}$. Further, $BaZr_{0.1}Ce_{0.7}Y_{0.1}Yb_{0.1}O_{3-\delta}$ shows very promising property for anti-sulfur applications [59]. Compared with the conventional solid-state reaction method [59, 63, 75, 76], the advantage of a wet-chemistry technique with the help of chelating ligand is that the constituent ions are mixed at the atomic level in the solution so that nano-sized precipitates can be formed. This method will result in fine particles which may promote sintering, consequently making it easier to obtain gas-tight samples for different applications. The modified Pechini process has been reported as a better

synthesis method to obtain fine crystalline with fluffy morphology, which is suitable to fabricate thin membranes by a dry-pressing method [17, 77, 78], as well as to obtain dense electrolyte ceramics with reduced sintering temperatures [76], which will be beneficial to the fabrication of SOFCs in order to maintain the porous structure of the electrodes, especially for the electrode supported SOFCs which require co-sintering of the electrolyte membrane and the electrode support. It is also beneficial to reduce the formation of the secondary phases in grain boundaries which may adversely affect the conductivity of the electrolyte. On the other hand, reduced sintering temperature will decrease the sintered density which may raise the gas-tightness issue of the electrolyte. Therefore, it is critical to study the sintering process for a given proton conducting material in order to obtain an optimum sintering temperature.

In this study, $BaZr_{0.1}Ce_{0.7}Y_{0.1}Yb_{0.1}O_{3-\delta}$ has been chosen as a potential electrolyte material and prepared by a modified Pechini method to evaluate the sinterability and microstructure development. The correlation between the sintering mechanism and the electrical conductivity has been investigated in Chapter 4.

3.4.2 Preparation

The $BaZr_{0.1}Ce_{0.7}Y_{0.1}Yb_{0.1}O_{3-\delta}$ (denoted as BZCYYb afterwards) powder was prepared by a modified Pechini method as reported elsewhere [17, 79, 80]. $Ba(NO_3)_2$ (Alfa Aesar, 99.95%), $Ce(NO_3)_3 \cdot 6H_2O$ (Alfa Aesar, 99.5%), $ZrO(NO_3)_2 \cdot xH_2O$ (Alfa Aesar, 99.9%), $Y(NO_3)_3 \cdot 6H_2O$ (Alfa Aesar, 99.9%) and $Yb(NO_3)_3 \cdot xH_2O$ (Alfa Aesar, 99.9%) were used as starting materials and dissolved in deionized water. The concentration of the metal ions in the individual nitrate was titrated. The procedure was

the same as for the preparation of BSCY. The obtained dry foam was subsequently fired at 600^{o}C for 4 h in air to remove organic residue, resulting in light-colored powders. The powder was then calcined at different temperatures between 700 and 1200^{o}C, at 100^{o}C intervals, for 5 h in air with a heating rate of 3^{o}C min^{-1}. The obtained powder was pulverized and mixed with 8 wt% polyvinyl alcohol (PVA) binder and pressed uniaxially into pellets under 600 MPa (13 mm in diameter and about 1 mm in thickness). The green pellets were sintered from 1350 to 1550^{o}C for 5h in air with a heating rate of 2^{o}C min^{-1}, at 50^{o}C intervals. The sintered samples with different sintering temperatures of 1350^{o}C, 1400^{o}C, 1450^{o}C, 1500^{o}C and 1550^{o}C were denoted as sample 1350, 1400, 1450, 1500 and 1550, respectively.

The powder pre-treated at 600^{o}C was analyzed using differential scanning calorimeter (DSC) and thermogravimetry (TG) on a NETZSCH STA 409 CD thermal analyzer. The powder was heated from room temperature to 1250^{o}C at a heating rate of 5^{o}C min^{-1} under dynamic air atmosphere.

3.4.3 Phase structure and morphology revolution

Fig. 3.5(a) shows the XRD patterns of the BZCYYb powders calcined at different temperatures. It can be seen that when the calcination temperature is lower than 800^{o}C, the predominant phases are $BaCO_3$ and CeO_2, with only a small amount of the perovskite phase. Calcination at 900^{o}C results in a perovskite phase dominant structure, with some $BaCO_3$ and CeO_2 impurities. The formation of the $BaCO_3$ impurity is due to the reaction between Ba^{2+} ions and CO_3^{2-} ions which are the product of the reaction between citric acid and/or EDTA and O_2 during heating [75]. When calcined at T $\geq$1000^{o}C, $BaCO_3$

decomposed and a single perovskite phase was obtained. To ensure that all the carbonate impurity was completely decomposed based on the prior studies [59, 75], a calcining process of 1100°C for 5 h has been chosen. Fig. 3.5(b) shows the XRD patterns of the samples sintered at different temperatures. A predominant orthorhombic perovskite structure similar to that of $BaCeO_3$ can be observed for all the samples.

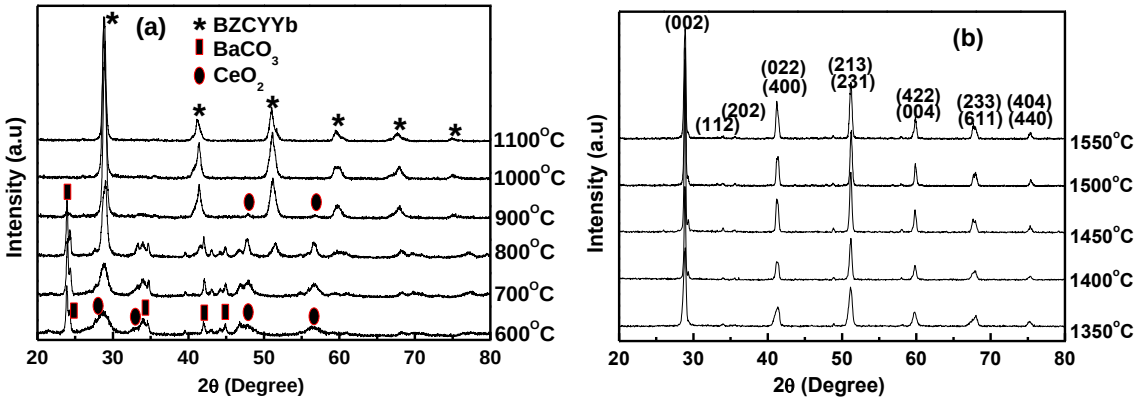

Figure 3.5 XRD patterns of BZCYYb samples: (a) XRD of BZCYYb powder calcined at different temperatures; (b) XRD patterns of BZCYYb pellets sintered at different temperatures.

To investigate the reaction during the formation of the perovskite phase structure, simultaneous TG-DSC curves of the sample conducted from room temperature to 1250°C are presented in Fig. 3.6. The sample powder was preheated at 600°C for 4 h prior to the TG-DSC measurement. From Fig. 3.6 it can be seen that the TG curve displays a drastic weight loss starting at around 750°C with a corresponding exothermic effect, which can be related to the decomposition of $BaCO_3$ and the formation of BZCYYb with the release of CO_2 [75, 81]. This is consistent to the XRD results in Fig.3.5(a) that BZCYYb phase only forms upon calcining at 800°C and above. There is no apparent weight change when the temperature is higher than 1100°C, indicating that the decomposition of $BaCO_3$ and

the formation of BZCYYb have completed, consistent with the XRD results shown in Fig.3.5(a). The total weight loss from 750 to 1100^{o}C is 11.6% calculated from TG result in Fig. 3.6. Theoretical weight loss for the decomposition of $BaCO_3$ and formation of BCYY is calculated to be 12.1% from the following reaction:

$$BaCO_3 + 0.7CeO_2 + 0.1ZrO_2 + 0.05Y_2O_3 + 0.05Yb_2O_3 = BaZr_{0.1}Ce_{0.7}Y_{0.1}Yb_{0.1}O_{3-\delta} + CO_2 \uparrow$$

(3-1)

The slight discrepancy between the observed weight loss and the calculated value indicates that most Ba^{2+} ions may be combined with CO_3^{2-} to form $BaCO_3$, while some small amount of Ba^{2+} ions may form BaO or $Ba(OH)_2$. Although undetectable in XRD due to the trace amount, they may perform as reactant to form BZCYYb. The weight losses for the BaO and $Ba(OH)_2$ to react with CeO_2 to perform $BaCeO_3$ are 0 and 5.3%, respectively, which will account for the overall weight loss to an intermediate value of 11.6%. It is also noted that a DSC endothermic peak appeared at around 120^{o}C, probably due to water evaporation above 100^{o}C. It is likely that the fine powders obtained from the solution process absorb moisture in air during the cooling process and the subsequent storage in the lab.

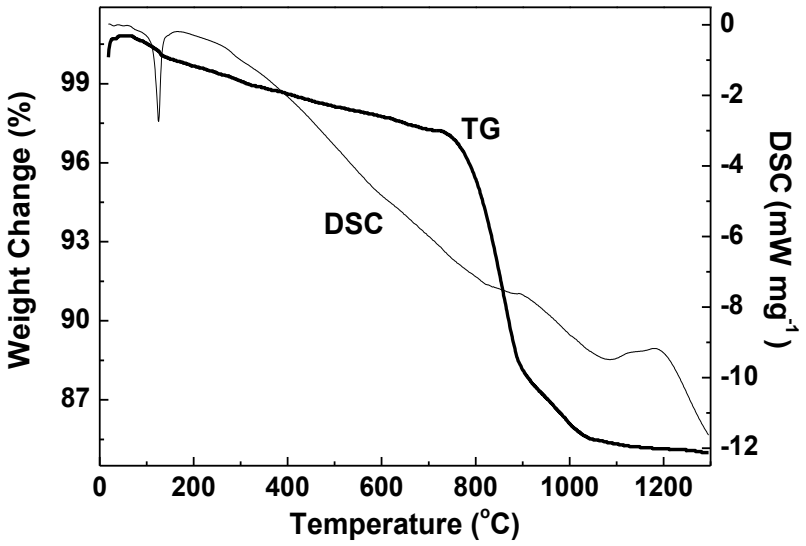

Figure 3.6 TG-DSC curves of the BZCYYb powder preheated at 600°C for 4 h.

The BZCYYb powder calcined at 1100°C for 5 h in air is presented in Fig. 3.7. It reveals a porous morphology with voids distributed inside the powder. Such powder with fluffy morphology has very low filled density and can be used for the fabrication of thin membrane electrolytes using a versatile dry-pressing method, as has been demonstrated previously [17, 77, 78]. After sintered at high temperatures, all the samples show dense structures, with relative density higher than 94% of the theoretical value. With the increase in sintering temperature, the pores between the grains and inside particles gradually diminish, resulting in a higher density, achieving a relative density higher than 99.5% at the sintering temperature of 1550°C.

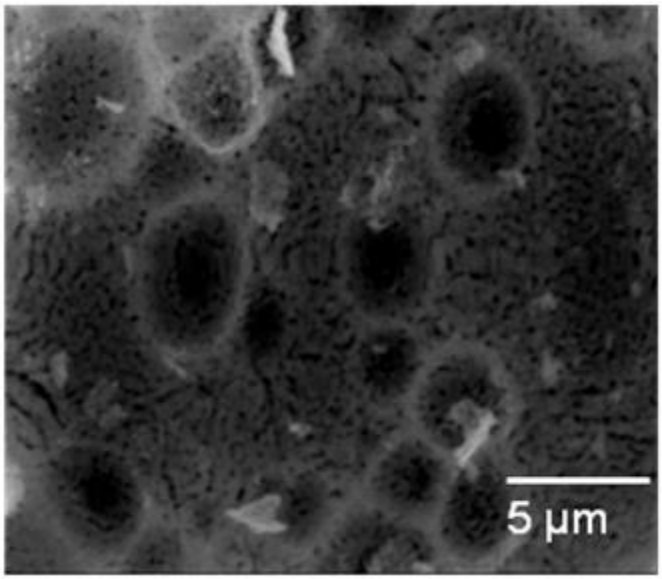

Figure 3.7 SEM photograph of BZCYYb powder calcined at 1100^{o}C for 5h in air.

To illustrate the influence of sintering temperature on the microstructure, SEM images of the samples sintered at different temperatures are presented in Fig. 3.8. The left-hand images a_1 to e_1 show the surface morphology of the sintered pellets, while the right-hand images a_2 to e_2 are cross-sectional views of the ceramics. With sintering temperature increasing from 1350^{o}C to 1400^{o}C, the grain size increases sharply, with an average grain size increased from around 0.5 µm to 1.0 µm, as can be seen from sample 1350 and sample 1400. This may be due to the rapid grain growth of the ceramic with the increase in sintering temperature, eliminating the pores and pinholes. However, with further increase in sintering temperature, no obvious grain growth can be seen from the SEM images in Fig. 3.8.

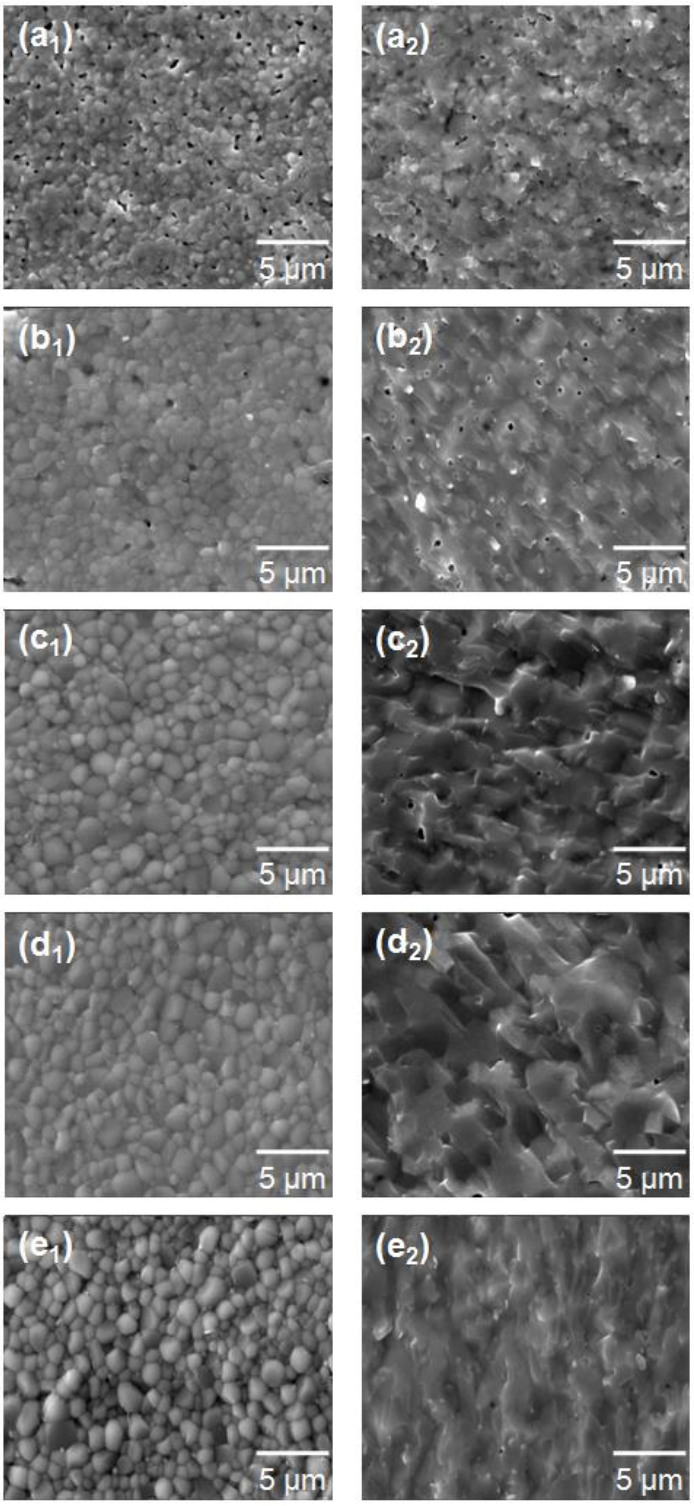

Figure 3.8 SEM photographs of samples sintered at different temperatures: a_1-e_1: surface morphology of the samples; a_2-e_2: cross-section view of the samples.

3.5 PREPARATION OF $BAZR_{0.1}CE_{0.7}Y_{0.1}YB_{0.1}O_{3-\Delta}$ BY CO-PRECIPITATION METHOD AND MICROSTRUCTURAL MODIFICATION OF PROTON CONDUCTING CERAMICS

3.5.1 Introduction

It is widely known that microstructure of the ceramics has significant impact on the performances. In many cases the mechanical and electrical properties can be readily modified just by altering the grain size distributions without changing the composition of the ceramics [5-7]. Many parameters, such as particle sizes of the reactant materials, fabrication methods, and even the microstructure of the green bodies will affect the final microstructures of the ceramics [60]. In addition, the choice of sintering profiles plays a crucial role to adjust the final microstructure, especially the grain size distributions and densities of the ceramics. To obtain refined microstructure for the ceramic samples, advanced techniques such as spark-plasma sintering and high-temperature microwave sintering have been utilized by rapidly heating the samples to high temperatures to prevent or suppress grain growth [61, 62]. However, these advanced techniques are usually not assessable or affordable to most researchers and sometimes may induce heterogeneities [82].

As a promising alternative to prepare fine microstructured dense ceramics, the recently developed two-step sintering method has been proved to be less costly and more efficient [83]. With appropriate sintering profile, the two-step sintering can produce fully densified ceramics with grains constrained down to nanometer size. The mechanism for the two-step sintering method is to suppress the grain boundary migration of the ceramics which occurs at high temperature, while enabling the grain boundary diffusion which

occurs at relatively low temperature [83]. The first-stage high temperature sintering step helps eliminate supercritical pores while the second-stage low temperature sintering step suppresses grain growth [60]. This two-step sintering method has been applied with great success in obtaining dense ceramics with unique fine microstructures, including Y_2O_3 and SiC with nanometer-sized grains [83, 84], CeO_2 and cubic structured zirconia (8 mol% Y_2O_3 stabilized) with ultrafine grains [85, 86], and the perovskite structured barium titanite compound with an average grain size below 200 nm [87].

In this study, $BaZr_{0.1}Ce_{0.7}Y_{0.1}Yb_{0.1}O_{3-\delta}$ (BZCYYb) has been chosen due to its high conductivity and good chemical stability [31]. We have demonstrated that ultrafine grained dense BZCYYb ceramics can be achieved via a two-step sintering method and further evaluated the effect of microstructure on the electrical properties. In addition, the two-step sintering method has been applied to co-sinter an anode-electrolyte bi-layer based on BZCYYb electrolyte and BCN18 electrolyte membrane to fabricate proton conducting solid oxide fuel cells with significantly improved cell output power density.

3.5.2 Preparation

Powder samples of doped barium cerates having the nominal composition of $BaZr_{0.1}Ce_{0.7}Y_{0.1}Yb_{0.1}O_{3-\delta}$ (BZCYYb) were synthesized by a co-precipitation method as reported previously [85]. $Ba(NO_3)_2$ (Alfa Aesar, 99.95%), $Ce(NO_3)_3\ 6H_2O$ (Alfa Aesar, 99.5%), $ZrO(NO_3)_2\ xH_2O$ (Alfa Aesar, 99.9%), $Y(NO_3)_3\ 6H_2O$ (Alfa Aesar, 99.9%) and $Yb(NO_3)_3\ xH_2O$ (Alfa Aesar, 99.9%) were used as starting materials and dissolved in deionized water and titrated to determine the concentration of the metal ions. Stoichiometric ratio of each metal ion was taken and mixed with deionized water as

precursors and $(NH_4)_2CO_3$ (Fisher Scientific, 95%) was used as the mineralizer. The precursors were dripped into the mineralizer at a rate of 3 ml/min under stirring. The obtained ivory-colored co-precipitate was washed with de-ionized water and ethanol to obtain a pH value of 7 and then filtered and dried. The obtained raw powders were subsequently calcined at 1100^{o}C for 5 h in air. Fig. 3.9 illustrates the co-precipitation process. The obtained powder was then pulverized and mixed with 5 wt% polyvinyl alcohol (PVA) binder and pressed uniaxially into pellets under 600 MPa (13 mm in diameter and about 1 mm in thickness) for further sintering study.

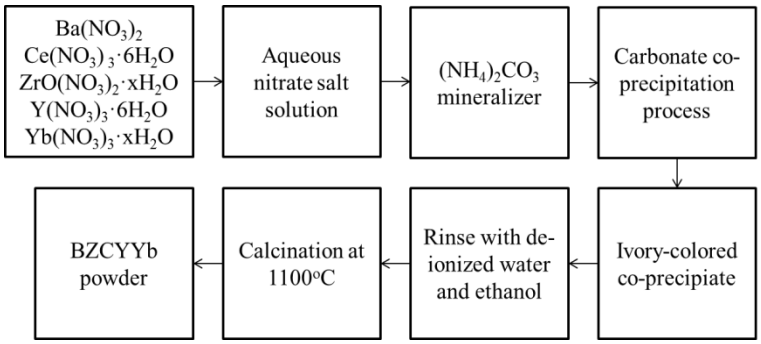

Figure 3.9 Co-precipitation procedure for preparation of BZCYYb powder.

The pressed pellets were sintered via a two-step sintering method in which the samples were heated at 5^{o}C min^{-1} to 600^{o}C and held for 2 h to remove the organic PVA bonder, followed by heating to a peak temperature at 1450^{o}C for 1 min to achieve an intermediate density, then cooled at 15^{o}C min^{-1} to 1300^{o}C and held for 20 h, during which the ceramic densification was achieved while grain growth was suppressed [83]. As comparison, some pressed pellets were sintered via a conventional sintering method in

which the pellets were heated to 600^{o}C and held for 2 h, followed by heating to 1450^{o}C at a heating rate of 5^{o}C min^{-1} and held for 5 h. Some co-precipitate raw powders were also pressed directly into pellets and sintered through a reactive sintering method in which the pellets were heated to 600^{o}C and held for 2 h, followed by heating to 1450^{o}C at a heating rate of 5^{o}C min^{-1} and held for 5 h, where the decomposition of the co-precipitate to form perovskite phase and subsequent sintering of the perovskite powders took place consecutively. The sintered pellets are named as Two-step, Conv., Reactive for samples sintered via a two-step sintering method, conventional sintering method, and reactive sintering method, respectively. The schematic sintering profile for two-step sintering method is shown in Fig. 3.10.

Figure 3.10 Two-step sintering profile for BZCYYb ceramic.

3.5.3 Two-step Sintering of Ultrafine-grained Barium Cerate Proton Conductor

Fig. 3.11 shows the TEM bright field image of BZCYYb co-precipitated raw particles. Fig. 3.11 inset is the FESEM morphology of the raw powder. It can be seen that fine particles with an average particle size around 30 nm are loosely agglomerated. The co-precipitation method adopted here produces spherical and uniform nano-sized grains,

which is advantageous for the decomposition to form BZCYYb phase and the subsequent densification of the BZCYYb ceramics.

Fig. 3.12 are the XRD patterns of the sintered pellets using different sintering methods. All the samples show predominantly orthorhombic perovskite structure similar to that of $BaCeO_3$ (JCPDS No. 22-0074). Since Y^{3+} (0.9 Å) and Yb^{3+} (0.868 Å) have similar ionic radii to that of Ce^{4+} (0.87 Å), a solid solution is expected to form by doping Y and Yb into Ce sites. Trace amount of $(Y,Ce)O_{2-\delta}$ impurity peaks can be found in the conventional and reactive sintered samples, while for two-step sintered samples, this impurity is less and hard to discern. It is noted that there were $(Y,Ce)O_{2-\delta}$ impurities for the calcined samples.

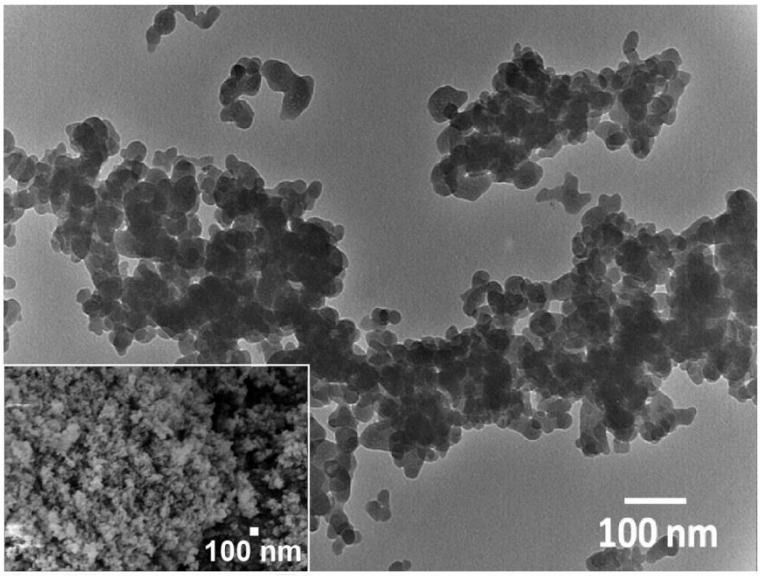

Figure 3.11 TEM bright filed image of BZCYYb raw powder prepared by co-precipitation method. Inset is the FESEM picture of the powder.

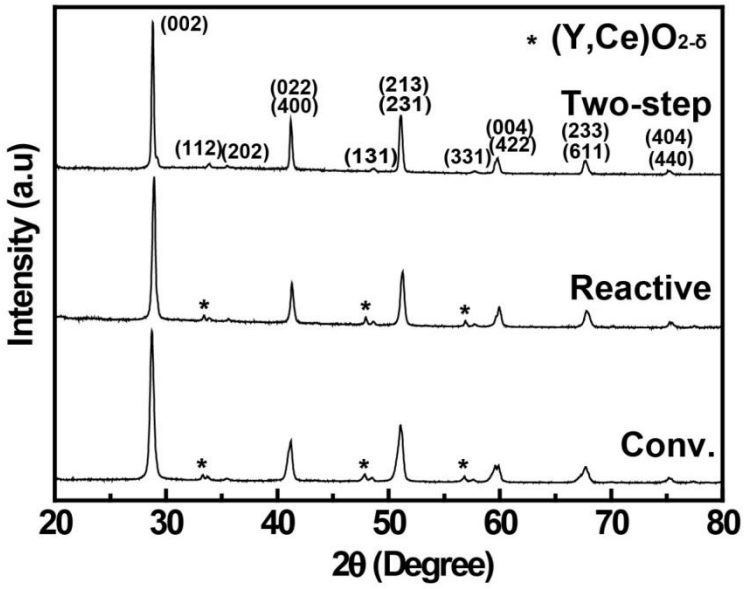

Figure 3.12 XRD patterns of the sintered BZCYYb samples via conventional sintering method (Conv.), reactive sintering method (Reactive) and two step sintering method (Two-step).

Fig. 3.13(A-C) are the surface while Fig. 3.13(a-c) are cross-section FESEM images of BZCYYb sample sintered using conventional sintering, reactive sintering, and two-step sintering, respectively. It can be seen that all the samples are well sintered with sub-micron grain sizes. Two-step sintered BZCYYb sample shows the finest grain size of 184 nm and a porosity of 3.13% measured by mercury porosimetry, compared with that of 445 nm with a porosity of 1.91% for conventional sintered sample. It is thus clearly seen that the activation energy for grain boundary migration is not satisfied while the grain boundary diffusion is active for BZCYYb by this two-step sintering profile. The detailed grain sizes and porosity distribution of the samples are shown in Fig. 3.14.

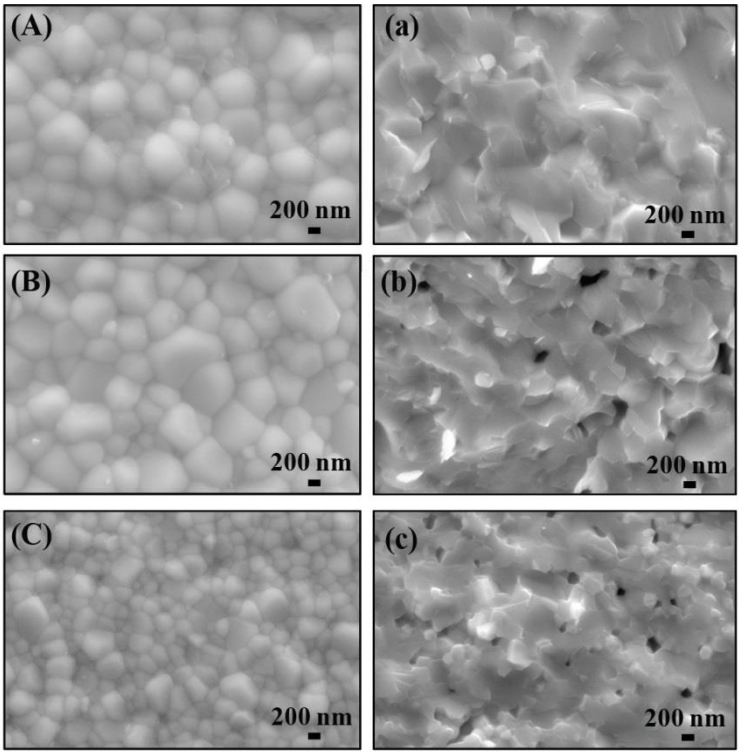

Figure 3.13 FESEM pictures of BZCYYb sample pellets sintered via different profiles. Left: Surface morphologies; Right: Cross-sectional morphology; (A,a) Conventional; (B,b) Reactive; (C,c) Two-step.

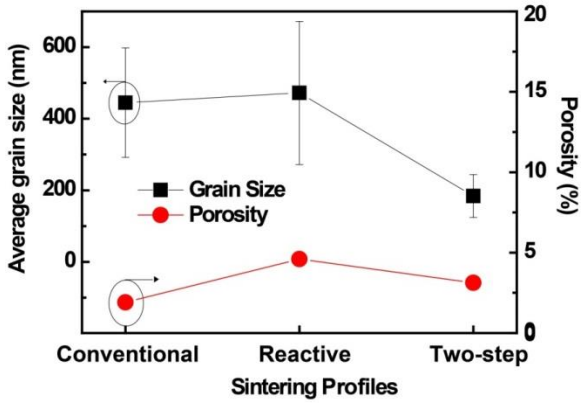

Figure 3.14 Grain size and porosity distribution of BZCYYb ceramics with different sintering profiles.

The sintering behaviors of the samples were investigated by the dilatometry. Calcined samples were pressed into cylinders and sintered via two-step sintering and conventional sintering methods in the dilatometer. For reactive sintered samples, the raw powders were directly pressed into cylinders and measured by the dilatometer. Fig. 3.15 shows the dilatometric curves of BZCYYb samples with different sintering profiles. Inset is the expanded view of the linear shrinkage rate dL/dt. From the linear shrinkage curve dL/L_0 it can be seen that the sample from the reactive sintering method had the largest shrinkage during the sintering process. This is expected because in addition to the shrinkage at high temperature as a result of phase formation and densification process, considerable shrinkage took place at low temperature range (below 600^oC) due to removal of absorbed water and decomposition of the carbonates. Both the conventional sintering and two-step sintering methods showed similar trend up to 1450^oC since they have the same sintering profile. After the sample reached 1450^oC for 1 min, fast cooling rate helped prevent additional grain growth, thus enabling further shrinkage for two-step sintered sample, consistent with modeling prediction that relatively fast cooling rate is preferred for two-step sintering method [82]. During this stage, the linear shrinkage percentage (dL/L_0) increased from 18.2% for conventional sintered samples to 19.4% for the two-step sintered ones. From the linear shrinkage rate shown in the inset, the maximum shrinkage rate $(dL/dt)_{max}$ occurred around 398 min (at 1370^oC) for all the samples. A peak temperature of 1450^oC as the first sintering step is appropriate for sample two-step sintered BZCYYb, since an intermediate density higher than 70% is necessary to guarantee the disappearance of supercritical pores while the other pores

become subcritical and unstable against shrinkage to ensure a subsequently densified body at a lower holding temperature at 1300^{o}C [83].

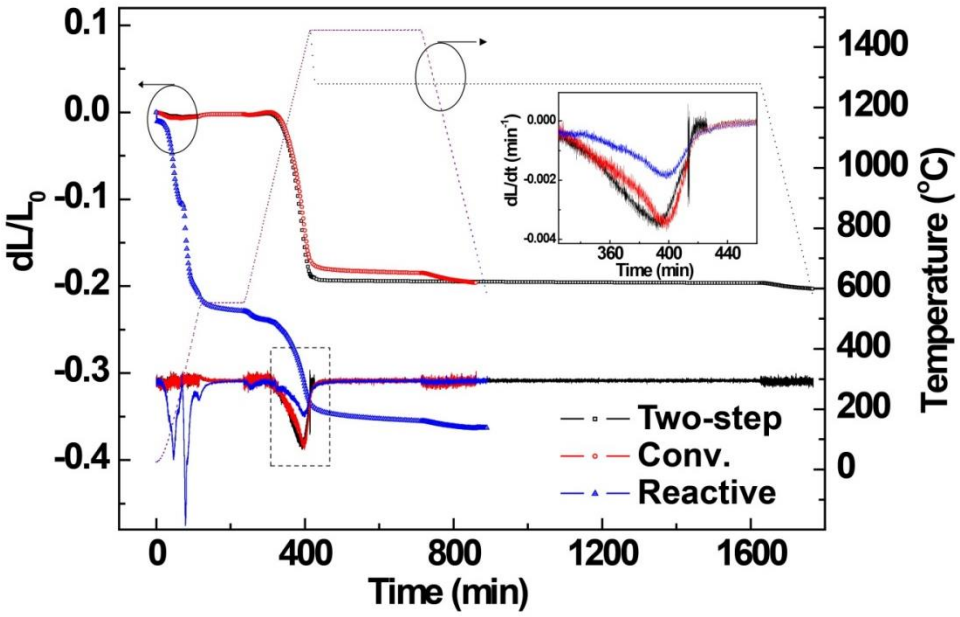

Figure 3.15 Dilatometric curves of BZCYYb samples with different sintering profiles. Inset is the expanded view of the rate of change in linear shrinkage.

3.6 PREPARATION OF $BA_3CA_{1.18}NB_{1.82}O_{9-\Delta}$ BASED CERAMICS BY SOLID STATE REACTION METHOD

3.6.1 Introduction

As mentioned before, although the barium cerates based proton conductors possess the highest level of proton conductivities, they are readily decomposed in CO_2 and/or humid atmospheres at elevated temperatures due to their thermodynamically structural instability [58, 73]. Two strategies have been exploited to overcome this problem. The first is to partially replace Ce ions with other cations such as Ta to form solid (Ce,Zr) solution to improve the chemical stability [73]. Alkine earth zirconate are

much more stable but the introduction of Zr into Ce site also greatly deteriorates the total conductivity [58, 88]. The second strategy is to explore novel proton conductors with good chemical stability while still maintaining high proton conductivity. Several novel structured compounds have so far been reported as proton conducting oxides. Acceptor-doped $LaNbO_4$ based orthoniobates was reported pure proton conductivity at temperatures below 700^oC [40]; β-K_2SO_4 structured $La_{1-x}Ba_{1+x}GaO_{4-x/2}$ containing GaO_4 tetrahedral unites was found to possess significant proton conductivity as well as fast oxide-ion conductivity [41]; The perovskite related oxygen deficient brownmillerite structured $Ba_2In_2O_5$ demonstrated significant proton conductivity because of its intrinsic oxygen vacancies [89]; and the cation off stoichiometric complex perovskite structured $Ba_3Ca_{1.18}Nb_{1.82}O_{9-\delta}$ (BCN18) showed a proton transport number close to unity for pO_2 $<10^{-5}$ bar [28]. Unfortunately, the proton conductivity values of the above mentioned compounds are fairly low compared to their peer simple perovskite proton conductors. Nevertheless, some of the novel proton conductors show unique properties. Among them, the complex perovskite structured BCN18 show excellent chemical and structural stability in CO_2 and/or water atmospheres [90]. Consequently, if the electrical conduction behavior can be improved without sacrificing its chemical stability, this material can be of a very promising potential for field applications. In this study, we systematically evaluated the effect of partial replacement of Ca and Nb ions by Ce ions and Y ions on the phase structure, structural ordering and electrical conductivity for BCN18 system. The chemical stability in water and/or CO_2 containing atmosphere was also characterized.

3.6.2 Experimental

The samples were prepared by a conventional solid state reaction method [59, 91, 92]. Stoichiometric amount of $BaCO_3$ (Alfa Aesar, 99.8%), $CaCO_3$ (Alfa Aesar, 99.5%), Nb_2O_5 (Alfa Aesar, 99.9%), CeO_2 (Alfa Aesar, 99.9%) and/or Y_2O_3 (Alfa Aesar, 99.9%) were mixed together by ball-milling in ethanol for 24 h. After drying, the obtained powders were pressed into pellets, followed by calcining at 1200^{o}C for 5 h in air with a heating rate of 3^{o}C min^{-1}. The pellets were then grinded into powders which were subsequently mixed with 5 wt% polyvinyl alcohol (PVA) binder and uniaxially pressed into pellets under a pressure of 400 MPa. The green pellets were sintered at 1550^{o}C for 5 h in air with a heating rate of 2 ^{o}C min^{-1}.

3.6.3 Phase structure and morphology revolution

3.6.3.1 Effect of Ce doping on $Ba_3Ca_{1.18}Nb_{1.82}O_{9-\delta}$

Fig. 3.16(a) shows the XRD patterns of different samples prepared at 1200^{o}C for 4 h. The calcined powders are composed primarily of the cubic perovskite phase, with $BaCeO_3$ impurity phase present upon doping of Ce ions in the B sites, as noted in Fig. 1(a) with arrows. The majority perovskite structure may thus be Ba deficient due to the formation of $BaCeO_3$ secondary phase. As the calcination temperature increases, Ce ions gradually dissolve into the complex perovskite structure. As an example, XRD patterns of BC(NC0.2) calcined at different temperatures are shown in Fig. 3.16(b). The result indicates that the solubility of dopants can be tuned to a higher extent by increasing the calcination temperature, similar to that of $BaCeO_3$ based proton conductors [70]. The peak split of the XRD patterns indicative of two phase structures may be caused by the

coexistence of unhydrated and hydrated phases of the powders. As the calcination temperature is further increased, the unhydrated phase will be dominant. Similar phenomena on $Ba_3Ca_{1.18}Ta_{1.82}O_{8.73}$, $Ba_{0.5}In_{0.5}ZrO_{3-\delta}$ and $Sr_3Ca_{1+x}Nb_{2-x}O_{9-\delta}$ systems have also been reported [93, 94].

Fig. 3.17 shows the XRD patterns of the samples sintered at 1550^{o}C for 5 h. Single cubic complex perovskite structure with no secondary phases are obtained for all the samples, showing that $BaCeO_3$ has reacted with the nonstoichiometric perovskite phase completely. The small (111) peaks at 2θ angle around 18.2^o is an indication of B site 1:1 ordering of the perovskite structure for all the samples (shown in Fig 2 inset for the (111) step scan). The lattice parameters for the samples are 8.4095, 8.4149, 8.433 and 8.442 Å for BCN18, B(CC0.1)N, BC(NC0.1) and BC(NC0.2), respectively, consistent with step scan results of (220) peaks which shows a peak shift to a lower 2θ degree (shown in Fig. 3.17 inset). For pure BCN18, it is B site 1:1 ordering mixed with random ordering [28]. The introduction of Ce^{4+} (0.87 Å) into either Ca^{2+} (1.00 Å) sites or Nb^{5+} (0.64 Å) sites would promote the B-sites-disordering of the structure, which would be expected to increase the ion mobility and consequently enhance the ionic conductivity [32]. However, for sample B(CC0.1)N, a decrease in lattice parameter, with expectation of Ce^{4+} (0.87 Å) substitution on Ca^{2+} (1.00 Å), has not been observed. Th increase of the lattice parameter may probably be due to the valence change of Ce^{4+} ions into Ce^{3+} ions (1.01 Å) for charge compensation consideration. Ce^{3+} is more likely to substitute into Ca^{2+} site because its ionic radius is more closely matched to that of Ca^{2+}. This will in turn deteriorate the disordering status of BCN18 structure and results in a decreased conductivity. For BC(NC0.1) and BC(NC0.2) samples, it is consistent with the

expectation that the increase in the lattice parameters is a consequence of large Ce ions (either 3+ or 4+ oxidation states) substituted into small Nb^{5+} sites and an enhancement of the conductivity has been observed.

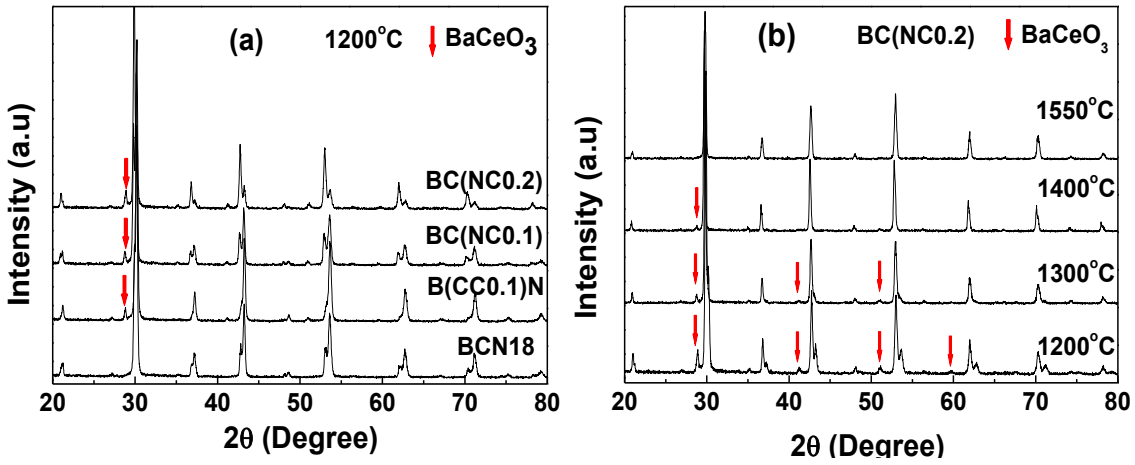

Figure 3.16 (a) XRD patterns of samples calcined at 1200°C for 5 h; (b) XRD patterns of BC(NC0.2) calcined at different temperatures. The arrows correspond to the $BaCeO_3$ impurity peaks.

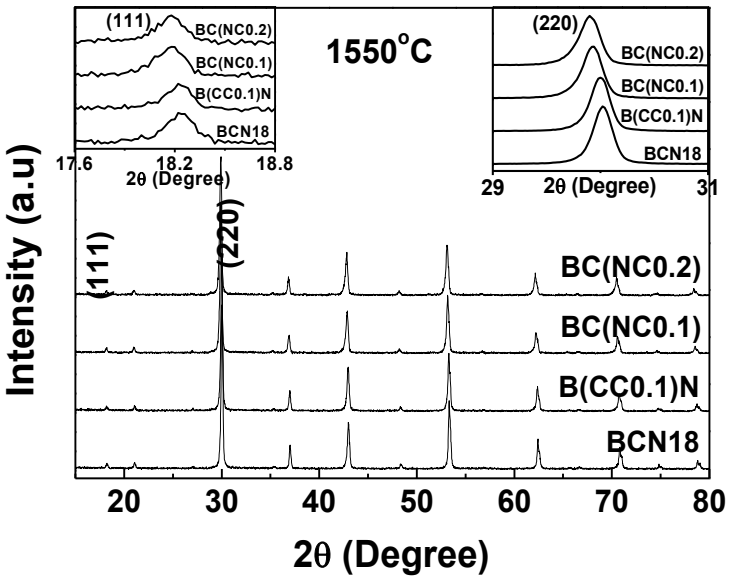

Figure 3.17 XRD patterns of samples sintered at 1550°C for 5 h, with step scan of (111) and (220) peaks in the inset pictures.

To further determine the Ce-ions' oxidation states because of the doping effect, XPS measurements were employed to obtain the Ce 3d spectra for sample B(CC0.1)N and BC(NC0.1) shown in Fig. 3.18. The Ce 3d spectra for CeO_2 and $BaCe_{0.85}Y_{0.15}O_{3-\delta}$ (denoted as BCY) were also collected as references. It can be seen that for both B(CC0.1)N and BC(NC0.1) samples, the Ce-ions show a mixture of 3+ and 4+ oxidation states, indicating Ce^{3+} and Ce^{4+} ions co-exist for both samples. For example, for Ce-ions substituted into Nb^{5+} ions as supposed, there are Ce^{3+} ions that might either doped into Nb^{5+} or Ca^{2+} sites. Compared with B(CC0.1)N, the peak intensities for BC(NC0.1) are stronger at binding energy of 881 eV and 915.5 eV, which are characteristic of Ce^{4+} spectrum (starred peaks in Fig. 3.18) [95]. This is indicative of more Ce^{4+} ions exhibited in BC(NC0.1) than in B(CC0.1)N. The XPS results confirmed with the XRD experiments that the Ca^{2+} sites are more favorable for Ce^{3+} substitution while smaller Nb^{5+} sites are more favorable for Ce^{4+} ions substitution. It is also noted that even for $BaCe_{0.85}Y_{0.15}O_{3-\delta}$, the Ce 3d spectrum shows a mixture of 3+ and 4+ oxidation states, probably because of the iconicity in perovskite structures with large covalent characteristics [96].

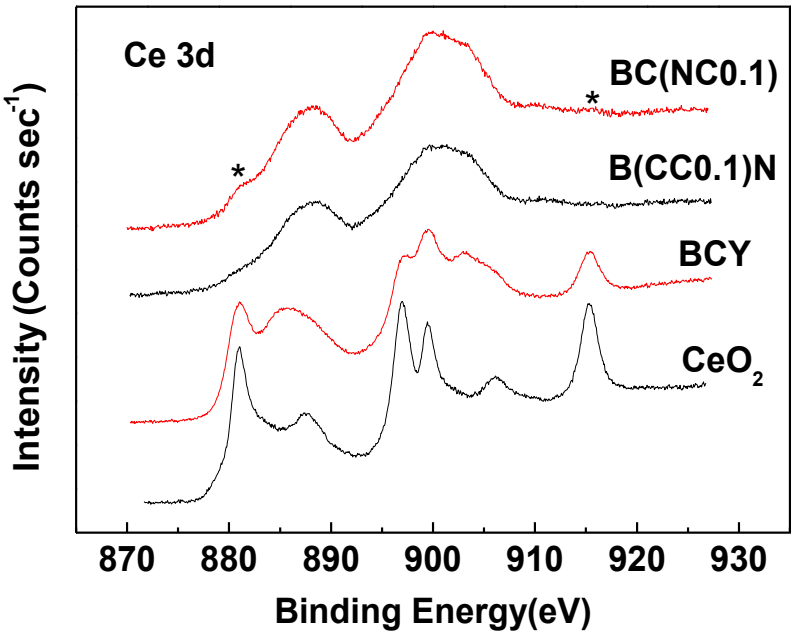

Figure 3.18 XPS spectra of Ce 3d for samples BC(NC0.1), B(CC0.1)N, $BaCe_{0.85}Y_{0.15}O_{3-\delta}$ (BCY) and CeO_2 collected at room temperature.

The microstructures of the sintered pellets are presented in Fig. 3.19. The top images reveal the surface morphologies while the bottom images are the corresponding cross-sectional view of the same samples. All the samples show dense microstructures, consistent with the Archimedes density tests that all the samples have greater than 94% relative densities. The average grain sizes measured from the surface images for the sintered pellets are 3.14±1.18, 2.41±0.90, 3.57±1.19 and 4.20±1.60 μm, respectively, indicating that the introduction of cerium into Ca^{2+} sites will inhibit the grain growth, while the introduction of Ce ions into Nb^{5+} sites will promote the grain growth and consequently reduce the density of grain boundaries [49]. Therefore, the doping of Ce ions into either B' or B'' sites shows a clear effect on the grain growth of the sintered samples which would in turn affect the electrical performance.

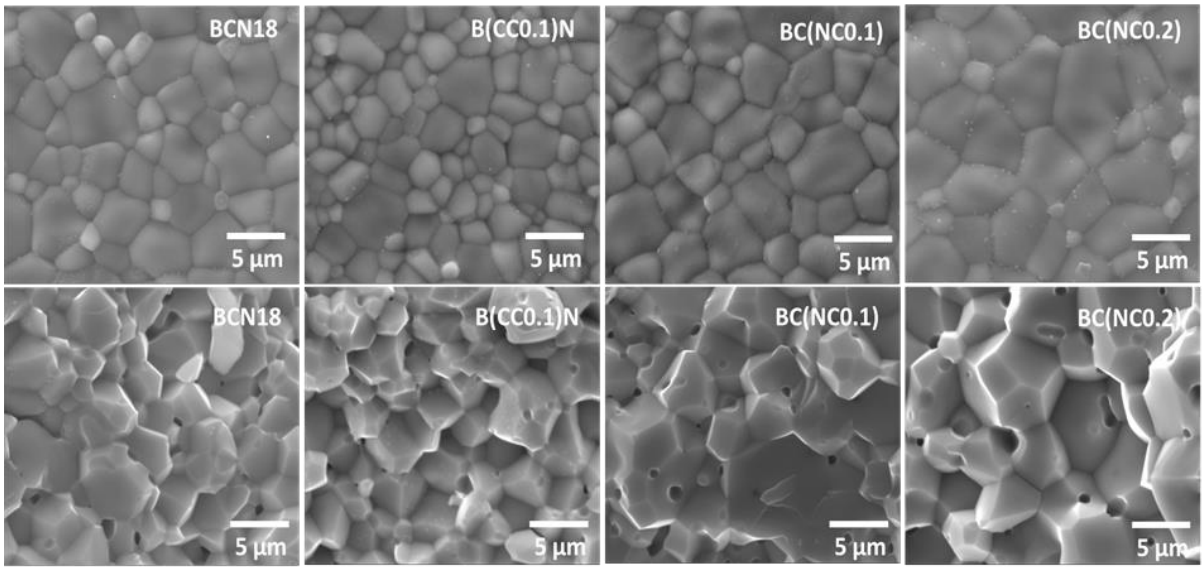

Figure 3.19 SEM images of the sintered pellets; top images: surface morphology of the pellets; bottom images: cross-section view of the pellets.

3.6.3.2 Doping limits for $Ba_3Ca_{1.18}Nb_{1.82-x}Y_xO_{9-\delta}$

XRD patterns of the samples obtained from the surface of the pellet samples sintered at 1550^{o}C for 5 h are shown in Fig. 3.20. Only peaks corresponding to cubic perovskite phase can be found in the patterns for up to 30% Y doped BCNY0.3. For BCNY0.5, BaO_2 and $BaCO_3$ impurities were detected on the surface of the sintered pellet, indicating that excessive barium were segregated at the grain boundaries and/or diffused to the surface of the sample and reacted with CO_2 and O_2 in the environment to form $BaCO_3$ and BaO/BaO_2 [97, 98]. After polishing the surface of the sintered BCNY0.5 pellets with sand paper, the impurities on the surface were removed within XRD resolution. It is noticed that trace amount CaO phase can be identified as the secondary phase in BCNY0.5, which was also detected by the higher resolution neutron diffraction patterns for other compositions.

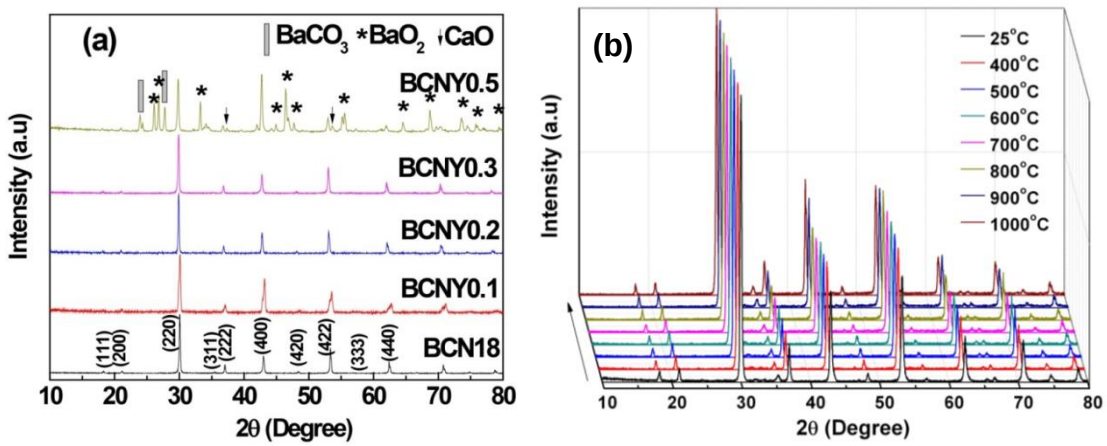

Figure 3.20 (a) XRD patterns of sample pellets sintered at 1550°C for 5 h in air (b) *In-situ* high temperature XRD of BCNY0.3 under N_2 atmosphere.

From the X-ray structure factor information we know the two peaks (111) and (311) around 18 and 35° are indicative of cation ordering for the structures. For fully disordered perovskite, ie., the 4a and 4b sites in the B-site cations are identical, or although different ions occupancy but can move freely, the (111) and (311) peaks will disappear. The intensity ratio for (111)/(022), (311)/(022) and (311)/(222) peaks for selected samples are presented in Table 3.1. It can be seen that as more Y^{3+} are doped, the relative intensity of (111) and (311) peaks are lower. It is as expected since for Y^{3+} doped in either 4b sites for Nb^{5+}, or 4a sites (can be Nb^{5+} or Ca^{2+}), the difference in cation ionic radii decreases, leading to a decreased degree of cation ordering.

As we have detected from the XRD of polished BCNY0.5 sample, it is possible that some of Y^{3+} substituted Ca^{2+} and dissolved into the lattice, resulting in CaO precipitation. From the XRD pattern of other samples the CaO secondary phase could not be detected. However, from the neutron diffraction patterns of the samples, it can be seen that extra peaks other than Fm-3m based cubic BCN18 related peaks, can be identified as

Fm-3m structured CaO phase ,with lattice parameter a=4.8140 nm. The refined structural parameters are shown in Table 3.2. For sample BCNY0.2, 20% introduction of Y leads to 0.163 wt% CaO precipitation; while 30% introduction of Y amount results in 0.695 wt% of CaO precipitation. Although we intended to substitute Y with Nb, the precipitation o CaO is due to the solubility limit of Y into the structure, which is related with the ionic radius tolerance (tolerant factor *t*) and charge neutrality law. The lattice parameter increases with the doping level of yttrium due to the larger yttrium ions compared with the niobium ions. The atomic occupancies for selected samples are calculated and presented in Table 3.2. It shows that the slight substitution of Ca^{2+} and oxygen vacancies give the compensatory charge from the difference of Y^{3+} and Nb^{5+}.

Table 3.1 Relative intensity of selected BCNY samples which indicates the degree of cation ordering of the samples.

Intensity ratio	**(111)/(022)**	**(113)/(022)**	**(113)/(222)**
BCN18	0.02458	0.01315	0.09456
BCNY0.3	0.02293	0.00726	0.06066
BCNY0.5	0.01680	0.00489	0.04174

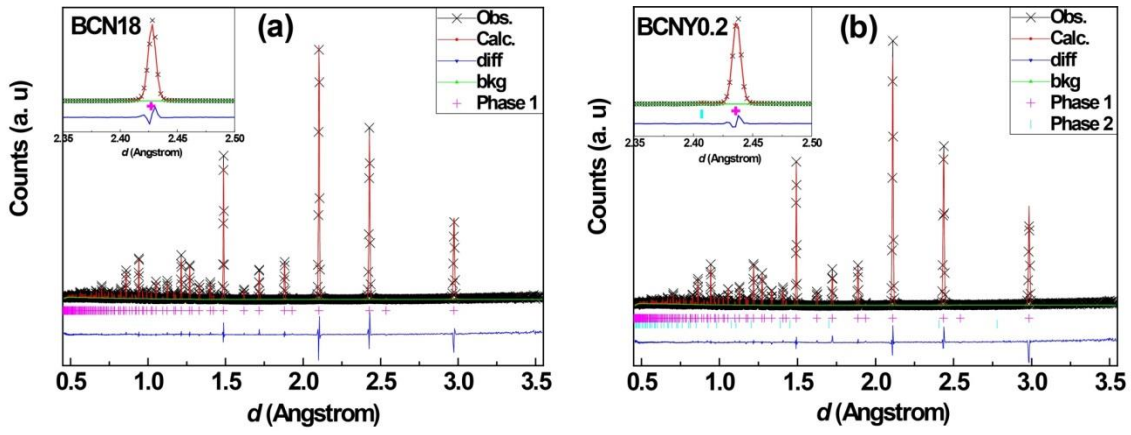

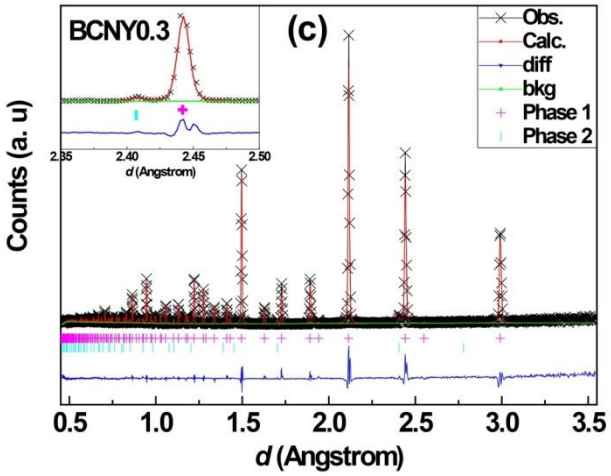

Figure 3.21 Neutron diffraction Reitveld refinement of (a) BCN18, (b) BCNY0.2 and (c) BCNY0.3 sintered sample powders.

XPS was employed to determine the oxidation states of the elements in the samples. Ba 3d, Ca 2p, Nb 3d and Y 3d spectra for BCNY0.3 are shown in Fig. 3.22(a). It can be seen that the spectra of Ba and Nb can be fitted using single lines for both $3d_{5/2}$ and $3d_{3/2}$ levels. In contrast, both the calcium and yttrium spectra can only be fitted using two doublets with four features, resulting from two different oxidation states. The $3d_{5/2}$ binding energy for barium is 779.2 eV, which is characteristic of the +2 oxidation state; the $3d_{5/2}$ binding energy for niobium is 205.8 eV, obviously lower than that of niobium in Nb_2O_5 (~207.2 eV) [99], indicating that Nb ions possess a nominal valence of less than +5. For Ca and Y ions, the existence of two different oxidation states indicates that they reside in two different local chemical environments. As discussed in Neutron diffraction measurement results, besides the substitution of Nb by Y as expected, small amount of Y substituted into Ca sites resulted in CaO precipitation. Different phases of Ca^{2+} and different local environment of Y^{3+} contributed to the multiple oxidation states for Ca and

Y. The large variation of oxidation states is a consequence of the incorporation of oxygen vacancies. Other samples also show similar spectra.

The amount of oxygen vacancies can be increased by doping with aliovalent dopants. The trivalent metal ion such as Y^{3+} doped into Nb^{5+} site would create an oxygen vacancy:

$$Y_2O_3 \xrightarrow{Nb_2O_5} 2Y''_{Nb} + 3O_O^{\times} + 2V_O^{\cdot\cdot} \qquad (3\text{-}2)$$

The defects with positive effective charge usually comprises $V_O^{\bullet\bullet}$. Significant differences should appear in the XPS spectra of O 1s for the different compositions. In order to determine the doping effect on the oxygen vacancy concentrations, the pairs of O 1s peaks has also been collected for selected samples as shown in Fig. 3.22(b). The two peaks indicate two types of oxygen presented on the samples' surface, with lower energy peak (~529 eV) attributed to the lattice oxygen, and higher energy peak (~531 eV) assigned to the surface adsorbed oxygen-containing species typically in the form of carbonate and hydroxyl species [100, 101]. It can be seen that the ratio of the higher energy peak increases as Y-doping increases, indicating that the surface absorbed oxygen increases with increasing Y-doping as a result of the creation of more oxygen vacancies in the bulk area [102]. It should be noted that although the oxygen vacancies increased by the substitution of Nb with Y, there is possibility that the concentration of the point defect complex/associates ($V_O^{\cdot\cdot}Y''_{Nb}$) derived from the columbic attraction between $V_O^{\cdot\cdot}$ and Y''_{Nb}, may also increase with the increment of yttrium content, resulting in a decrease of effective/free oxygen vacancy concentration. Consequently, even though BCNY0.5 is expected to produce more oxygen vacancies, it is possible that the oxygen vacancies available for proton conduction may be less than that of BCNY0.3.

Table 3.2 Parameters for the neutron diffraction Rietveld refinement.

Parameters	**BCN18**	**BCNY0.2**	**BCNY0.3**
***a* (Å)**	8.4077	8.4378	8.4594
Occup. Nb^{5+} (*4a*)	0.148	0.08	0.013
Occup. Ca^{2+} (*4a*)	0.852	0.815	0.808
Occup. Y^{3+} (*4a*)	0	0.105	0.178
Occup. O^{2-} (Cal.)	0.939	0.907	0.901
Occup. O^{2-} (For.)	0.940	0.895	0.873
Position of O^{2-} (*x*)	0.26215	0.264281	0.265005
Rwp	0.0728	0.0694	0.0763
Rp	0.0573	0.0525	0.0604
χ^2	12.78	10.85	13.73
CaO wt%	0	0.163%	0.695%

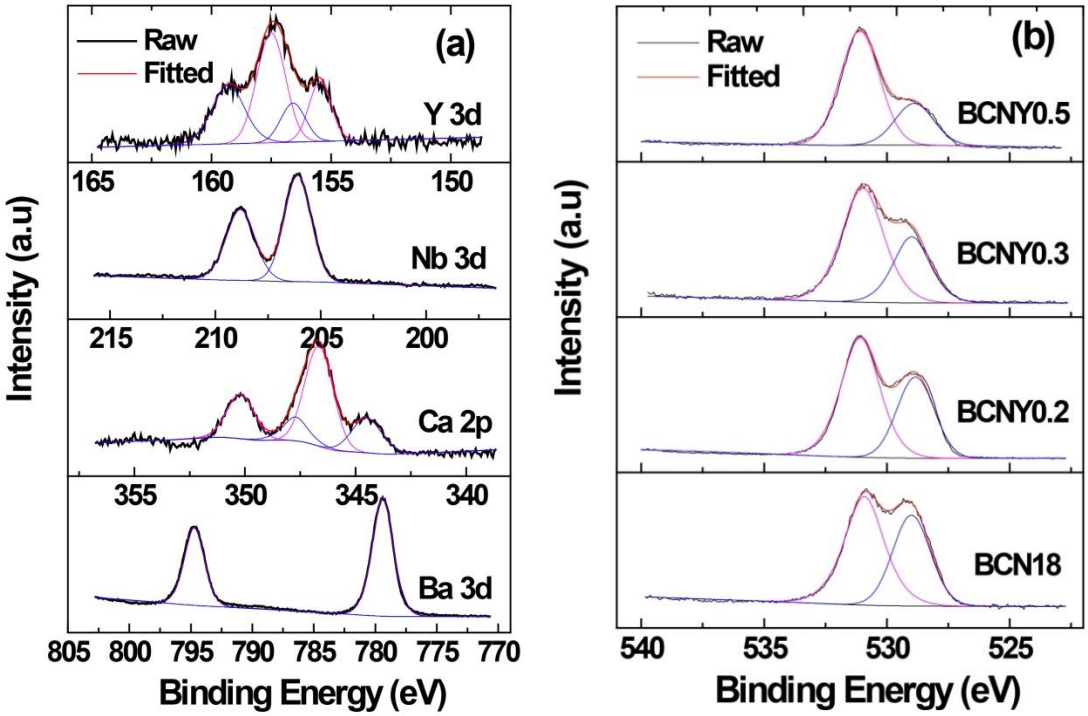

Figure 3.22 XPS spectra of Ba 3d, Ca 2p, Nb 3d and Y 3d for sample BCNY0.**3;** (b) XPS spectra of O 1s for selected samples.

Fig. 3.23 shows SEM cross-sectional micrographs and the grain size distributions of the sintered pellets. It can be seen that all the samples are well sintered, consistent with the results of density measurement using Archimedes method (higher than 96%). The average grain size is determined by counting the adjacent grains in the surface SEM micrographs. It can be seen that the introduction of Y into Nb site significantly promotes the grain growth, while the effect is much more obvious for 50% Y doping, probably due to the existence of liquid phases during sintering for BCNY0.5.

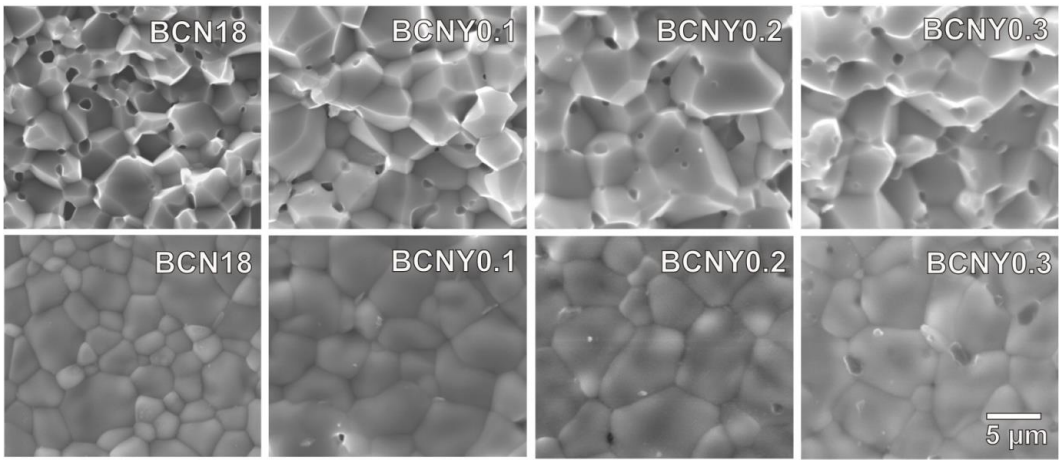

Figure 3.23 SEM micrographs of the sintered pellets; top images: cross-section view of the pellets; bottom images: surface view of the pellets.

The selected area electron diffraction (SAED) patterns and high resolution TEM images were then collected for the sintered BCNY0.2 and BCNY0.3 powder samples to check the crystal structure and ordering of the samples. The patterns have been indexed according to perovskite structure-type cell and the lattice parameters were calculated based on the SAED patterns and TEM images. The SAED pattern of BCNY0.2 is characteristic of a classic cubic perovskite along the [111] zone axis of the sample aligned parallel to the electron beam, with calculated $d_{(220)}$=0.288 nm, consistent with the XRD and NPD results for the structure configuration of the sample. In addition to the Bragg reflections characteristic of the perovskite unit cell, superlattice reflections are observed (indicated by arrows in the pattern), indicating the presence of extra domains. The extra nano-domains have been confirmed when observing the corresponding HRTEM image and magnified areas shown in Fig. 3.24(c-i). The chessboard and stripe typed patterns observed are often attributed to the short-range ordering in the structure, which may be caused by displacement of atoms, by variation in the occupancy of atomic

sites, or by both. In our case it is mainly caused by the cation B-site ordering due to the differences of ionic radius and charges among the Ca^{2+}, Nb^{5+} and Y^{3+}.

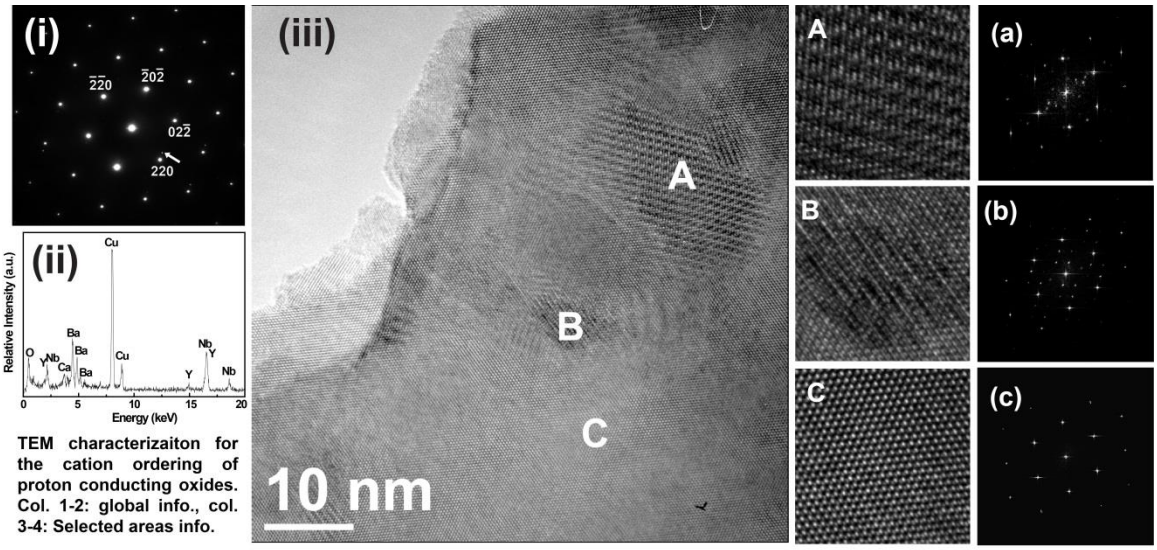

Figure 3.24 (i) SAED pattern of BCNY0.2 sintered pellet along the [111] zone axis of the sample powder aligned parallel to the electron beam, (ii) EDS spectra of the selected area (iii) HRTEM image corresponding to the [111] zone axis of the sample, and (A-C) magnifications of A, B, C domains, respectively, (a-c) fast fourier transform (FFT) of the magnificated domains, respectively.

The SAED pattern along the [100] zone axis of BCNY0.3 shows no extra spot besides the ideal perovskite unit cell as shown in Fig. 3.24. However, differences in brightness of the spots are indicative of a superlattice reflection because the material is ordered such that the actual real-space unit cell is larger and thus the reciprocal-space cell is smaller. The reconstruction of the reciprocal space from the SAED pattern lead to a superstructure of the cell, with a'=√2/2(a). The superstructure of the cell parameter is clearly observed on the HRTEM image by the domains displayed in Fig. 3.25 (A-B). Distances of 0.30 nm between characteristic rows of bright lines are observed in Fig. 3.25(A) and (a). Lattice fringes along in Fig. 3.25(B), indicating a √2 a_p periodicity along

this direction, is an reflection of ordering in B area. The EDX nanoanalysis performed on the crystal areas in STEM mode did not show differences in the chemical composition between domains of the crystals as shown in Fig.3.24(ii) and Fig. 3.25(ii), with more Y and less Nb concentrations in BCNY0.3 samples.

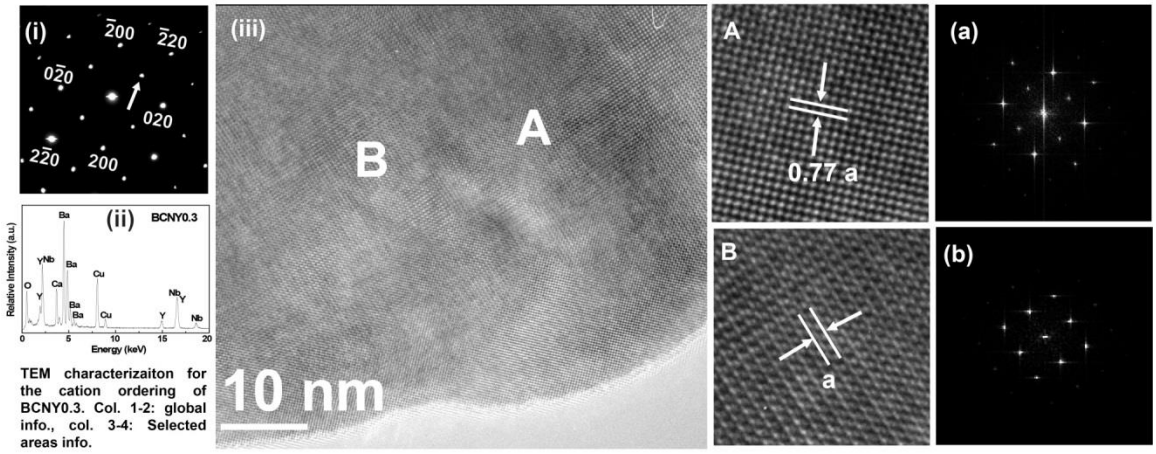

Figure 3.25 (i) SAED pattern of BCNY0.3 sintered pellet along the [100] zone zone axis of the sample powder aligned parallel to the electron beam, (ii) EDS spectra of the selected area (iii) HRTEM image corresponding to the [100] zone axis of the sample, and (A-B) magnifications of A and B domains, (a-b) fast fourier transform (FFT) of the magnificated domains, respectively.

3.7 FEASIBILITY OF TWO-STEP SINTERING METHOD TO FABRICATE $BA_3CA_{1.18}NB_{1.82}O_{9-\Delta}$ PROTON CONDUCTING CERAMICS

Fig. 3.26 shows the sintering profile and dilatometry study of the two-step sintering method applied to the BCN18 sample pretreated at 1100^{o}C. The sintering behavior for BCN18 using conventional sintering method has also been included for comparison. For the conventional sintering, the sample was heated at 1450^{o}C and held for 5 h. While for the two-step sintering, the BCN18 material was preheated at 1450^{o}C for 1 min followed by rapid cooling to 1300^{o}C and then held for 20 h. Although the sample

sintered using the conventional sintering method exhibits higher linear shrinkage, the temperature at which the maximum linear shrinkage rate $(dL/dt)_{max}$ appears is similar to that of the two-step sintering method . The sample sintered by the two-step sintering method exhibits larger $(dL/dt)_{max}$ as shown in the inset in Fig. 3.26, probably caused by the suddenly cooling down of the sample immediately after 1450°C. After applying TS-CS method to the anode-electrolyte bi-layer, the electrolyte membrane is densified (as shown in the SEM pictures of the single cells in chapter 5) with the assistance of the driven force originated from the shrinkage of the anode substrate during the co-sintering process.

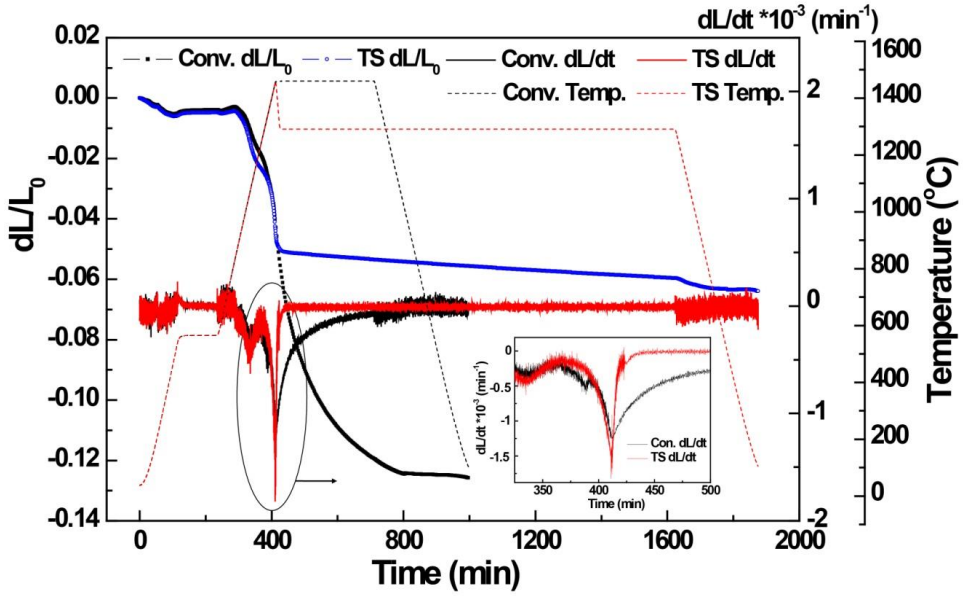

Figure 3.26 Sintering profiles and dilatometric curves of BCN18 electrolyte material with conventional (Conv.) sintering and two-step (TS) sintering method, inset is expanded view of the linear shrinkage rate (dL/dt).

3.8 SUMMARY

Several preparation methods including solid state reaction method, modified Pechini method, co-precipitation method, and two-step sintering method were selectively adopted to fabricate proton conducting ceramics for different purposes.

Modified Pechini method has been applied to prepare $Ba_{1-x}Sr_xCe_{0.8}Y_{0.2}O_{3-\delta}$ and BZCYYb proton conducting ceramics. It is feasible to prepare pure phased BaCe0.8Y0.2O3, while Y_2O_3 and Sr_2CeO_4 existed with higher concentration of Sr content for $Ba_{1-x}Sr_xCe_{0.8}Y_{0.2}O_{3-\delta}$. $BaCe_{0.7}Zr_{0.1}Y_{0.1}Yb_{0.1}O_{3-\delta}$ pure phase powder has been successfully prepared from the modified Pechini method with calcination temperatures $\geq$ 1000^{o}C, showing fluffy morphology with very low filled density. The subsequent sintering temperature plays an important role on the microstructure of the sintered pellets. The densification of the pellets started at 1400^{o}C, showing rapid gain growth of the ceramic pellets.

Co-precipitation method produced spherical and uniform nano-sized grains, which is advantageous for the densification of the BZCYYb ceramics. Two-step sintering method was examined on such co-precipitated BZCYYb proton conducting ceramics and ultrafine grained dense BZCYYb proton conductor was successfully prepared with a holding temperature of 1300^{o}C for 20h. Compared with conventional sintering methods, higher sinterability was observed from the dilatometric study for samples sintered by two-step sintering method.

Solid state reaction method was adopted to prepare $Ba_3Ca_{1.18}Nb_{1.82}O_{9-\delta}$ based ceramics, with either Ce or Y doping into A site or B site. By sintering at 1550^{o}C for 5h, single phase complex perovskite structure has been formed for all the samples studied. Ce

ions were mixed oxidation states for both substitutions, with more 4+ oxidation states for Nb substitution. Ce substituted with Nb ions promoted the grain growth. Partial substitution of Nb by Y in BCN18 shows a space group of Fm-3m, with trace amount of CaO evaporated as detected by neutron powder diffraction. XPS results showed that Y-doping introduced multi-oxidation states for Ca and Y, and +4 oxidation states for Nb. It is expected to introduce oxygen vacancies, which is beneficial for the proton conduction. Microstructure analysis of the sintered samples indicated that Y-doping enhanced the grain growth of the pellets sintered at 1550^{o}C for 5 h. The degree of B-site cation ordering is reduced due to the Y substitution for $Ba_3Ca_{1.18}Nb_{1.82-x}Y_xO_{9-\delta}$system. The two-step sintering method was also tried on $Ba_3Ca_{1.18}Nb_{1.82}O_{9-\delta}$ based ceramics which showed larger maximum linear shrinkage rate than those prepared via conventional solid state reaction method.

CHAPTER 4

PROPERTY CHARACTERIZATION OF PROTON CONDUCTING CERAMICS

4.1 INTRODUCTION

Among various properties for the proton conducting ceramics, the proton conductivity, chemical stability and the thermal expansion coefficient are closely related with their applications and performances as proton-conducting solid oxide fuel cells and hydrogen separation membranes. The electrical conductivity, especially the proton conductivity is related with the ohmic resistance and maximum power output for the PC-SOFCs, and the hydrogen flux for the gas separation membranes. The chemical stability is related with the long term stability of the devices and systems. The thermal expansion coefficient is related with the thermal cycle stability in terms of thermal compatibility for the components for the devices.

For the applications, we aim at finding a proton conducting ceramic that possesses both high proton conductivity and excellent chemical stability. In this chapter, the electrical conductivity for the proton conductors is measured and the corresponding bulk and grain boundary conductivity are separated. The natures of the bulk and grain boundary conductivities are discussed from the defect chemistry point of view. The chemical stability of the proton conductors towards water and/or CO_2 are tested and the parameters that affecting the chemical stability are discussed. The TECs for selected

materials are measured as comparisons to the state-of-the-art proton conductor electrolyte materials as well as the electrode materials.

4.2 EXPERIMENTAL

In the conductivity measurements, both surfaces of the sintered pellets were polished, painted with platinum paste (Heraeus, CL11-5349) and baked at 950^{o}C for 30 min. Platinum wires were then attached to the surface of the platinum layer. Electrical conductivity was measured using A.C. impedance method. A.C. impedance responses were collected with A.C. amplitude of 10mV in the frequency range from 0.1 Hz to 1 MHz using an electrochemical station with built-in impedance analyzer (Versa STAT3-400, Princeton Applied Research). The conductivity measurement was carried out in wet air and wet H_2 atmospheres (3% water partial pressure, introduced by passing the gas through a water bubbler at room temperature) at a temperature range of 450-800^{o}C. The TEC of the material was carried out on samples sintered at 1400^{o}C using a NETZSCH DIL 402C pushrod dilatometer measured from room temperature to 1200^{o}C with a heating rate of 5^{o}C min^{-1}.

For the stability tests towards water and CO_2, experiments were carried out in atmospheres containing water and/or CO2. The sintered pellets were exposed into boiling water for several hours to evaluate the stability towards liquid water in hard environment. The stability tests were also conducted in pure CO_2 atmosphere as well as in wet 3 vol% CO_2 atmosphere (air as the balance gas, 3 vol% H_2O) to mimic operating conditions.

4.3 PROPERTIES OF $BA_{1-X}SR_XCE_{0.8}Y_{0.2}O_{3-\Delta}$ SYSTEM

4.3.1 Electrical conductivity of BSCY

Electrical conductivity data of the samples in wet H_2 in the temperature range of 450-800^oC are shown in Fig. 4.1 (a) and (b). Fig. 4.1(a) shows the conductivities of BSCY measured at different temperatures as a function of Sr concentration. It can be seen that the conductivity drops with the addition of Sr^{2+} ions into the Ba sites. Given that the conductivity of doped $SrCeO_3$ is lower than that of doped $BaCeO_3$, it is not surprising that the introduction of Sr into the latter should result in a reduction in its conductivity. Furthermore secondary phases such as Sr_2CeO_4 and/or Y_2O_3 formed due to phase segregations, as presented above, would also adversely affect the total conductivity. Fig. 4.1(b) presents the Arrhenius plot of the conductivities as a function of testing temperature. The activation energies of the samples are 30.28, 34.98, 44.45 and 56.0 kJ mol^{-1} for BSCY1, BSCY2, BSCY5 and SCY, respectively. There is a clear trend that the activation energy increases with the increase in Sr content. The conduction phenomena in these materials may be explained by an appropriate defect model (here we use the Kröger–Vink notation). Oxygen vacancies are generated through yttria-doping of the cerate. Under humidified conditions, hydroxide species can be produced by the oxidation of water vapor as shown in Reaction (2-1). Protons could then migrate by hopping from the $OH_O^{\bullet}$ site to oxide ion site at a normal lattice site nearby causing this material to exhibit the proton conductivity [68]. In the presence of hydrogen, hydrogen can react with oxide ions in the lattice producing hydroxide groups and electrons as in Reaction (4-1)

$$\frac{1}{2}H_{2(g)} + O_O^{\times} = OH_O^{\bullet} + e^{'} \qquad (4\text{-}1)$$

In the presence of oxygen, the conduction phenomena should depend on the partial pressure of oxygen. Under wet hydrogen environment, the oxygen partial pressure is relatively low and oxide ions may leave the lattice creating oxygen vacancies and electrons as expressed in Reaction (4-2):

$$O_O^{\times} = \frac{1}{2}O_{2(g)} + V_O^{\bullet\bullet} + 2e^{'} \qquad (4\text{-}2)$$

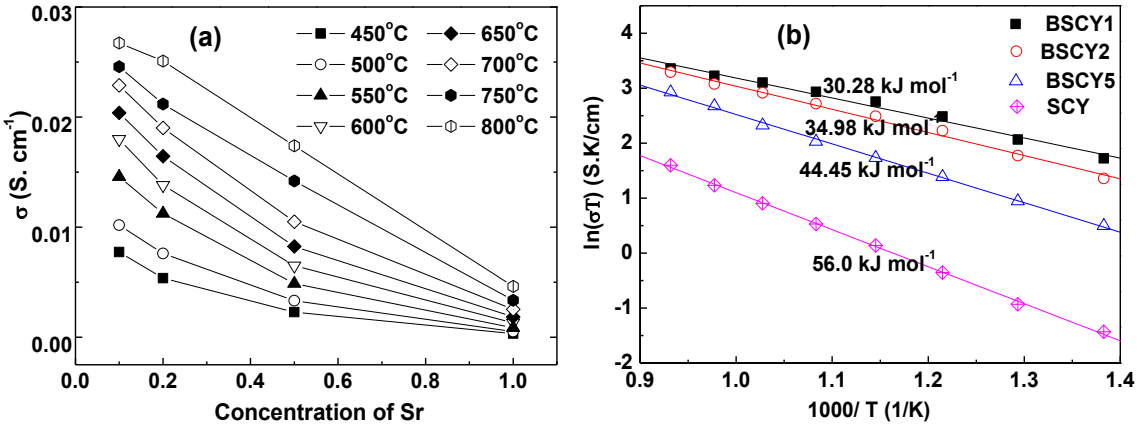

Figure 4.1 (a) Electrical conductivities in wet H_2 atmosphere for BSCY samples as a function of Sr concentration measured at different temperatures; (b) Arrhenius plots of the electrical conductivities for BSCY samples in wet H_2 atmosphere.

Consequently, doped $BaCeO_3$ shows mixed protonic and electronic conductivity in wet H_2 [103, 104], resulting in relatively lower activation energies. Further, BSCY samples with more Ba content will exhibit lower activation energy, constant with the previous study [32]. The data for $BaCe_{0.8}Y_{0.2}O_{3-\delta}$ did not show this kind of tendency. This difference may be due to the fact that $BaCe_{0.8}Y_{0.2}O_{3-\delta}$ is not as stable as BSCY in water containing atmospheres, thus leading to deterioration in conductivity when tested for extended period under high vapor pressure environment at elevated temperatures. Considering both the stability and the conductivity testing results, it can be concluded

that BSCY50 is an optimum composition by balancing the stability and electrical conductivity.

4.3.2 Chemical stability of BSCY

It has been demonstrated that $BaCeO_3$ is thermodynamically unstable in a water-containing atmosphere at elevated temperatures with the decomposition reaction shown in Equation (2-6) and (2-7) [105]. Thermodynamic calculation was conducted using HSC Chemistry Process Calculation Software [97]. Our thermodynamic calculation results on Gibbs free energy change, ΔG for reaction (2-6) also indicate that $BaCeO_3$ is thermodynamically unstable below 450^{o}C. Some doped $BaCeO_3$ based materials, such as 20 mol% Gd-doped $BaCeO_3$, are shown to be stable in water vapor at 600 and 700^{o}C for 1000 h but are unstable when heated in liquid water at 85^{o}C [18]. When considering the stability test, it is thus necessary to explore the possible effect of the sample treated in water vapor at high temperature, as well as treated at low temperature. Hung *et al.* have recently reported that $Ba_{0.9}Sr_{0.1}Ce_{0.8}Y_{0.2}O_{3-\delta}$ is kinetically stable in water rich environment at 80^{o}C. This information, however, is not definitive to conclude that $Ba_{0.9}Sr_{0.1}Ce_{0.8}Y_{0.2}O_{3-\delta}$ is stable in heated liquid water. The mechanism for $BaCeO_3$ based material to react with water can be understood in Equation (2-6). When $BaCeO_3$ based material is submerged in liquid water, the reaction product $Ba(OH)_2$ is soluble in water (though the solubility is modest), and the reaction product CeO_2 is insoluble, forming a porous layer on the surface of the $BaCeO_3$ based material. Besides, the formation of $Ba(OH)_2$ can result in a substantial volume expansion, thus cracks will be formed in the surface. The subsequent water penetration into the material will occur via the cracking

path and through the porous CeO_2 layer to react with the remaining $BaCeO_3$ [66]. However, in the presence of water vapor, after water reacting with a few surface mono-layers of $BaCeO_3$, since fewer water molecules penetrate into the grain boundaries compared with those in liquid water environment, the dissolution of $Ba(OH)_2$ in water vapor would be very slow, and the subsequent reaction rate for the forward direction of reaction (2-6) would be expected to be much slower than that in liquid water. Consequently, the two sets of data obtained by Hung [65] and Zhong [56] cannot be directly compared.

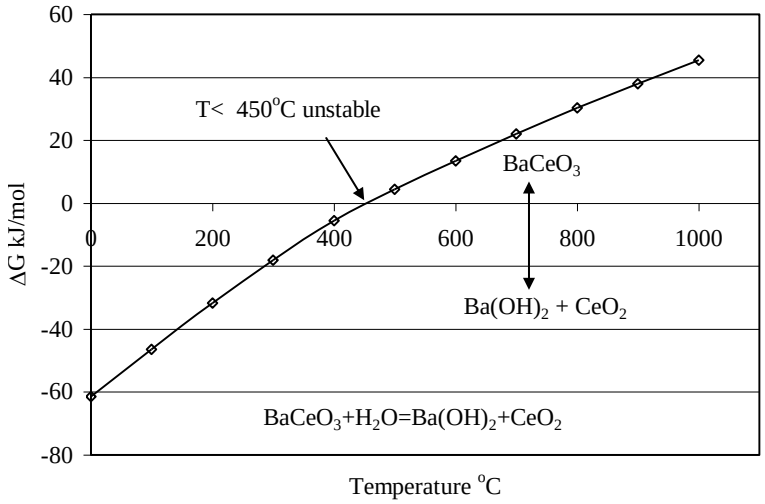

Figure 4.2 Thermodynamic calculations on Gibbs free energy change as a function of temperature for the decomposition of $BaCeO_3$ in water.

To evaluate the stability of BSCY in boiling water, sintered pellets with different contents of Sr were tested in boiling water for 4 h. Fig. 4.3(a) shows the XRD patterns of the pellets after treated in boiling water. The XRD pattern of BSCY1 before exposure to boiling water was presented for comparison. It can be seen from Fig. 4.3(a) that the XRD pattern for BCY changed significantly after treatment. After boiled in water for 4 h, BCY

pellet, at least on the surface of the sample, reacted with H_2O and CO_2 to form $Ba(OH)_2$, CeO_2 and $BaCO_3$, as indicated in Fig. 4.3(a). The formation of $Ba(OH)_2$ and CeO_2 can be understood by Equation (2-6), and the formation of $BaCO_3$ may be attributed by the reaction of $BaCeO_3$ with CO_2 dissolved in water or from air. Such impurity peaks could also readily be indexed for BSCY1 and BSCY2. For BSCY5 and SCY, however, these impurity peaks are insignificant, or at least not strong enough to be indexed. In other words, for BSCY samples with higher Sr content, the stability in water is enhanced. It can also be concluded from Fig. 4.3(a) that when placed in boiling water, $SrCe_{0.8}Y_{0.2}O_{3-\delta}$ will be more chemically stable than $BaCe_{0.8}Y_{0.2}O_{3-\delta}$.

The stability tests in carbon dioxide atmosphere at 900^{o}C for 2 h and in wet 3vol% CO_2 (air as the balance gas, 3vol% H_2O) at 700^{o}C for 12 h, respectively, were conducted to determine the stability of BSCY in CO_2 containing atmospheres. Fig. 4.3(b) shows the XRD patterns of the sintered BSCY pellets after exposure to wet CO_2 at 700^{o}C for 12 h. The XRD diffraction peaks after the CO_2 stability testing indicated that all the samples reacted with CO_2, with no observable reaction preference to either BCY or SCY. Based on chemical stability of BCY and SCY in CO_2, it is unlikely to expect that any composition of the mixture of BCY and SCY would be resistant to reactions with CO_2 at elevated temperatures.

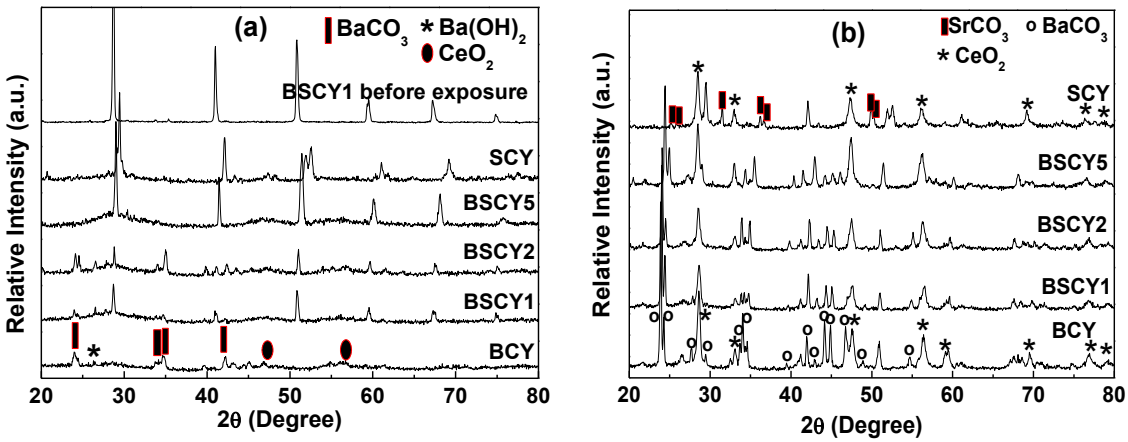

Figure 4.3 (a) XRD patterns of the sintered BSCY pellets after exposure in boiling water for 4 h, (b) XRD patterns of the sintered BSCY pellets after exposure in wet CO_2 at 700^{o}C for 12 h.

4.4 PROPERTIES OF $BACE_{0.7}ZR_{0.1}Y_{0.1}YB_{0.1}O_{3-\Delta}$ SYSTEM

4.4.1 Electrical conductivity of BZCYYb

The conductivity tests were conducted on the as prepared BZCYYb sample pelltes sintered at different temperatures. Fig. 4.4 shows the Arrhenius plots of the conductivities as a function of testing temperature for BZCYYb samples in wet air (Fig. 4.4(a)) and wet H_2 (Fig. 4.4(b)), respectively. Among the different samples tested in this work, sample 1400 shows the highest conductivity while sample 1550 shows the lowest conductivity. For samples sintered at lower temperatures, the existence of pores and pinholes as can be seen from Fig. 3.8(a) and Fig. 3.8(b) can result in a reduction in the conductivity. While for the samples sintered at 1500^{o}C and higher, segregation of secondary phases in the grain boundary areas deteriorates the conductivity, consistent with the reported conductivity results for $BaCe_{0.45}Zr_{0.45}Y_{0.1}O_{3-\delta}$, indicating that an optimum sintering temperature exists to obtain the maximum conductivity value as a result of achieving optimum values of density, grain size and phase purity [106]. The

activation energies measured in wet air are 36, 38, 35, 43 and 44 kJ mol^{-1} for sample 1350, 1400, 1450, 1500 and 1550, respectively, which are favorably close to the reported values [57]. In wet H_2 atmosphere (Fig. 4.4(b)), there is a clear tendency of decrease in the activation energy with the increase in testing temperature, reflecting the temperature dependence on proton concentration. The proton concentration in BZCYYb would decrease with an increase in temperature, caused by the dehydration of the materials due to the exothermic nature of the reaction in Equation (2-2) [107]. The bowed shapes for the conductivity curves can also be found in other proton conducting materials such as $BaZr_{0.1}Ce_{0.7}Y_{0.2}O_{3-\delta}$ and $BaZr_{0.9}Y_{0.1}O_{3-\delta}$ [42, 108]. It is noted that enhancement of conductivity in wet H_2 for the samples tested at reduced temperatures (below 600^oC) is observed, indicative of higher proton mobility leading to significant enhancement of proton conductivity at reduced temperatures [88]. As an example, for the sample sintered at 1400^oC shown in the inset in Fig. 4.4(a), the conductivity at 550^oC increased from 0.013 S cm^{-1} in wet air to 0.015 S cm^{-1} in wet H_2. The conductivity values are comparable to those reported for $BaZr_{0.1}Ce_{0.7}Y_{0.1}Yb_{0.1}O_{3-\delta}$ (about 0.018 S cm^{-1} in wet oxygen at 550^oC [59]) and $BaZr_{0.1}Ce_{0.7}Y_{0.2}O_{3-\delta}$ (about 0.01 S cm^{-1} in wet 4% H_2 at 550^oC [42]). Since the conductivity data were measured in different atmospheres, a slight deviation can be expected.

To further investigate the effect of the sintering temperature on the grain boundary conductivity, the impedance measurements are extended to lower temperatures where the grain boundary contribution can be readily recognized. Fig. 4.5 shows the typical Nyquist plots of sample 1400 measured at low temperature range in wet air. The inset pictures are expanded views of high frequency regions for the corresponding

impedance spectra. The impedance spectra typically have three semi-circles corresponding to the bulk, grain boundary and electrode responses from high to low frequencies. With an increase in the testing temperature, the semi-circle corresponding to the bulk conduction response gradually disappears. The bulk resistance is then derived from the high frequency intercept of the intermediate arc with the real axis. When the testing temperature was further increased, it became difficult to derive the bulk conduction from grain boundary conduction and only the total conductivity is recorded as shown in Fig. 4.4(a) and (b).

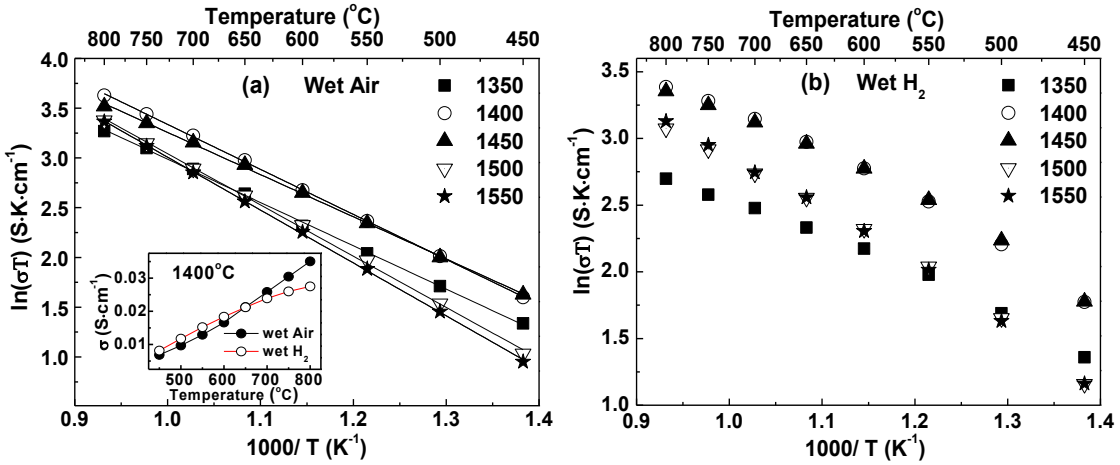

Figure 4.4 Arrhenius plots of conductivity for BZCYYb samples in (a) wet air and (b) wet H_2. Inset in (a) is the conductivity measured in wet air and wet H_2 of the samples sintered at 1400°C.

Fig. 4.6(a) shows the Arrhenius plots of the bulk conductivity of the sintered samples tested in wet air. It is observed the bulk conductivity values of the samples are very similar. A slight decrease of bulk conductivity can be seen for samples sintered at lower temperatures, probably due to the slightly lower sintered densities similar to the reported results on YSZ [109]. Fig 4-6(b) shows the grain boundary conductivity of

selected samples. It can be seen that when sintered at higher temperature, the grain boundary conductivity decreases, showing a combination effect of the grain size and phase impurity levels.

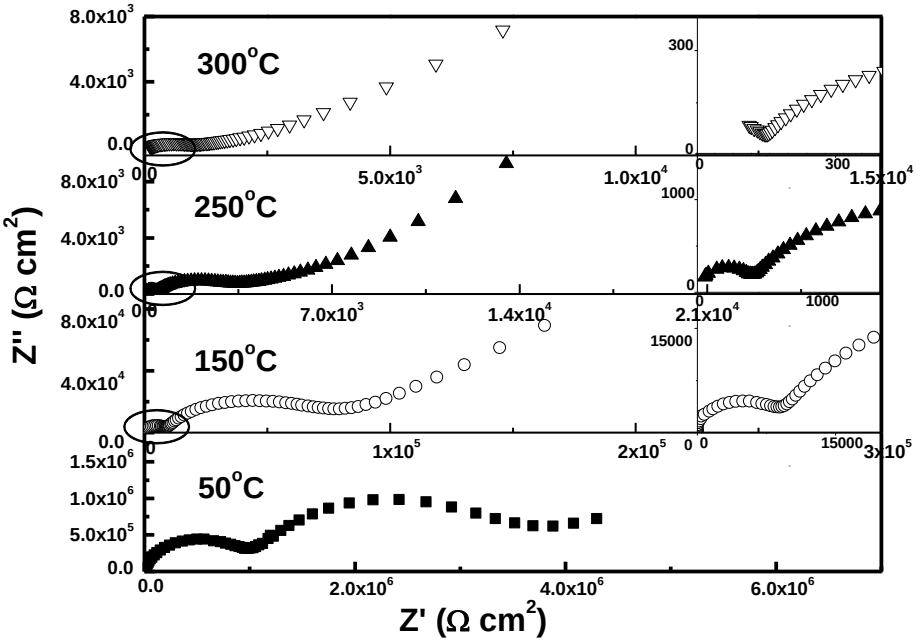

Figure 4.5 Nyquist plots of sample 1400 measured at different temperatures in wet air. Inset pictures are expanded views of the high frequency regions.

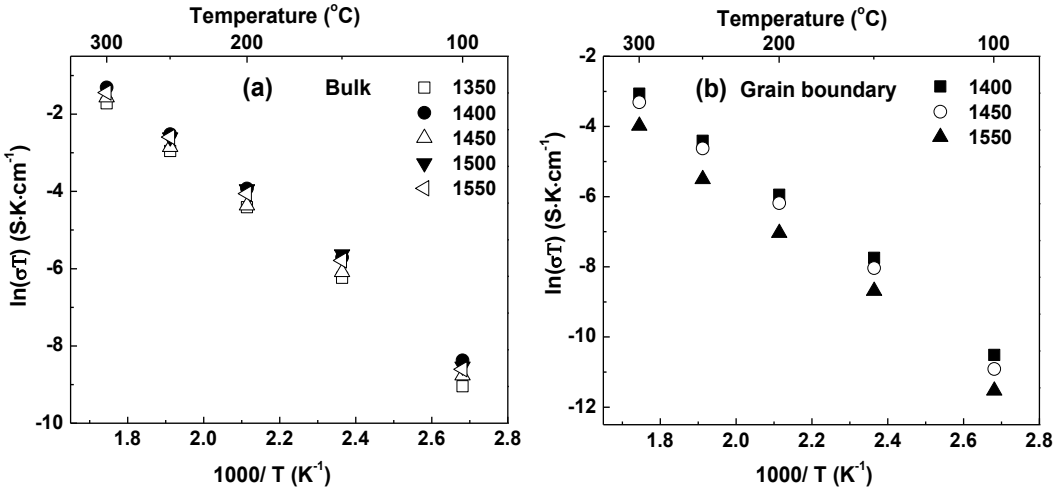

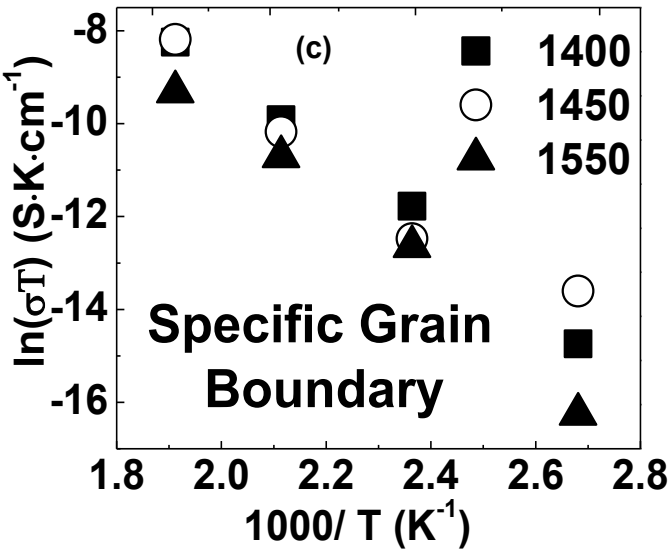

Figure 4.6 Arrhenius plots of (a) bulk, (b) grain boundary conductivity for BZCYYb sintered samples in wet air, (c) Arrhenius plots of specific grain boundary conductivity for BZCYYb sintered samples in wet air.

To eliminate the grain size effect, the specific grain boundary conductivity is calculated using brick-layer model [110]. Assuming that the dielectric constant of the bulk and the grain boundary is the same and not affected by temperature and the bulk conductivity is much higher than that of the specific grain boundary; the grain boundary thickness can be then calculated by the following Equation (4-3)

$$t = D\frac{C_{bulk}}{C_{gb}} \quad (4\text{-}3)$$

where D is the average grain size, C_{bulk} and C_{gb} are the capacitances of bulk and grain boundary conduction, respectively [111]. The capacitances were calculated by the AC impedance measurement by holding

$$2\pi fRC = 1 \quad (4\text{-}4)$$

for each semi-circle [24]. The specific grain boundary can be then obtained without knowing the microstructure of the material from the following Equation (4-5)

$$\sigma_{spgb} = \sigma_{gb}\left(\frac{t}{D+t}\right) = \sigma_{gb}\left(\frac{C_{bulk}}{C_{bulk}+C_{gb}}\right) \qquad (4\text{-}5)$$

Fig. 4.6(c) presents the specific grain boundary conductivity of some of the samples. The values of the specific grain boundaries are about three orders of magnitude smaller than that of the bulk conductivity, thereby blocking the total conductivity for the materials. The sample sintered at 1550^{o}C shows the lowest specific grain boundary conductivity, probably due to the increased impurity and secondary phase levels segregated in the grain boundaries. The main reason of the increase in impurities may be due to the Ba vaporization during higher temperature sintering process, leading to a variation in local stoichiometry on the surface of BZCYYb, thus resulting in a decreased conductivity [112]. Barium oxide has high volatility and the high temperature sintering process facilitates BaO vaporization, as has been extensively investigated by many research groups for the $BaCeO_3$ and $BaZrO_3$ systems [49, 113].

4.4.2 Electrical conductivity of two-step sintered BZCYYb sample

Fig. 4.7 presents the Arrhenius plot of the conductivity for co-precipitated $BaCe_{0.7}Zr_{0.1}Y_{0.1}Yb_{0.1}O_{3-\delta}$ powders sintered via two-step sintering method, conventional sintering method, and reactive sintering method, in wet air and wet hydrogen, respectively. The activation energy can be calculated through the Arrhenius equation (2-4), E_a can be calculated from the slopes in Fig. 4.7 [114]. The defect chemistry for proton conduction can be described as where $O_O^{\times}$ represents oxygen lattice, $V_O^{\bullet\bullet}$ denotes oxygen vacancy, and equation (2-2) represents proton charge carrier formed within the structure

by attaching to the oxygen lattice. It can be seen in Fig. 4.7 that for all the samples, the activation energy in wet air is higher than that in wet H_2, indicative of different conducting mechanisms. In wet air, the proton conductors are believed to be mixed conductions with the oxygen ion conduction competing with the proton conduction. The electronic hole conduction ($h^{\bullet}$) may also exist at high P_{O2} and high temperatures via equations (2-3) and (2-4). While in wet H_2, more protons tend to be active and mobile and are involved in the conduction process. There is also electronic conduction ($e^{'}$) at reduced atmospheres and high temperatures via equation (4-1). The activation energies of proton and electronic conduction are smaller than those of oxygen ion and electronic hole conduction, leading to less gradient curves as shown in Fig. 4.7(b). In wet H_2, there is a decrease in the activation energy at high temperature regime (higher than 600^{o}C), which might be caused by the decrease in proton concentration due to the exothermal nature of proton defect formation in equation (2-2) [1]: the reaction tends to shift to the left side with increasing temperatures, resulting in a decreased proton concentration. Alternatively, it can be understood that water will evaporate at high temperatures, leading to a decrease in $OH_O^{\bullet}$ concentration. Although the proton mobility increases with temperature, the compensation effect leads to a decrease of the activation energy [115]. The activation energies of the BZCYYb samples prepared in this study show good agreement with those of samples prepared by glycine nitrate process [116], but are higher than those of samples prepared by solid state reaction method and modified Pechini method [59, 117]. In general, activation energy can be influenced by several factors such as major charge carriers, phase transitions, or even sample degradation [43]. Different preparation methods may introduce different grain sizes and grain boundaries, and impurity levels in

grain boundaries also play an important role to affect the activation energy [116]. In this study, conventional sintering, reactive sintering, and two-step sintering methods have been used to prepare the samples. Consequently, different grain sizes were shown for the samples from the different sintering methods. The impurity levels in grain boundaries were different as discussed previously, which would affect the concentrations of charge carriers, although competing effects may appear for the final activation energy value. In wet air atmosphere (Fig. 4.7(a)), the increased activation energy for two-step sintered samples is mainly due to the improved electronic hole conductivity in the grain boundary region (via eq. (2-3) and (2-4), where electronic hole conduction ($h^{\bullet}$) shows higher activation energy than that of proton conduction). While in wet H_2 atmosphere (Fig. 4.7(b)), at high temperatures (above 600^{o}C), the improved electronic conductivity in the grain boundary area (via eq. (4-1) and (4-2), where electronic conduction ($e^{'}$) shows lower activation energy than that of proton conduction) may lead to a lower activation energy for the two-step sintered sample.

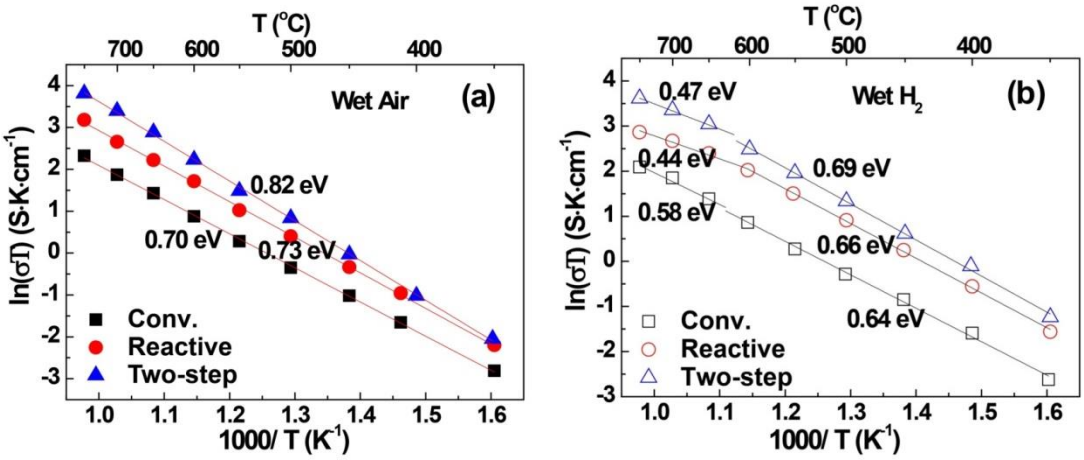

Figure 4.7 (a) Conductivity of BZCYYb samples measured in wet air, (b) Conductivity of BZCYYb samples measured in wet H_2.

In both air and H_2, the samples sintered by two-step sintering method show the highest conductivity, with 1.0×10^{-2} and 1.4×10^{-2} S cm^{-1} at 600^{o}C in wet air and wet H_2, respectively, followed by samples sintered via the reactive sintering method, while the samples sintered using the conventional sintering method have the lowest conductivity at the same testing conditions. The reason for the increase in conductivity may be attributed to the grain size effect on conductivity, and largely attributed to the improved grain boundary conductivity as a result from fewer amounts of impurity defects in the grain boundaries. The intrinsic grain boundary resistance may also play an important role to influence the grain boundary conductivity based on the space-charge model reported elsewhere [118, 119]. It is noted the sample sintered by two-step sintering method shows similar conductivity compared with literature results [117], while the conventional sintered samples using powders prepared by a co-precipitation method exhibits lower conductivity compared with samples prepared by solid state reaction method and Pechini method [59, 117], probably because of the secondary phases segregated in the grain boundaries which will deteriorate grain boundary conductivity and thus the total conductivity.

4.4.3 Thermal expansion measurement of BZCYYb ceramics

Thermal expansion matching among the cell components is critical for SOFC applications. Mismatch in the thermal expansion behavior between the electrolyte and the cathode can lead to the spallation of the cathode or cracking in the electrolyte-electrode interface, causing severe cell performance degradation. Fig. 4.8 shows the thermal expansion curves of the BZCYYb sample prepared via modified Pechini method and

sintered at 1400^{o}C in dynamic air, wet air and 5% H_2/N_2 atmospheres, respectively. It can be seen from Fig. 4.8 that at around 500-700^{o}C, there is a clear change in slope for the thermal expansion curves, probably due to a phase transformation from orthorhombic to rhombohedral for BZCYYb, very similar to the studies on doped or undoped $BaCeO_3$ proton conductor showing transformation to higher symmetry phases with increase in temperature [113, 120, 121]. The TEC values are 9.1×10^{-6}, 9.8×10^{-6}, and 9.2×10^{-6} K^{-1} in air, wet air, and 5% H_2 (balanced with 95% N_2) from room temperature to 1200^{o}C, respectively. These TEC values are lower than those of the typical cathode materials such as Sr-doped $LaMnO_3$ (11-12$\times10^{-6}$ K^{-1} [122, 123]) and $La_{0.6}Sr_{0.4}Co_{0.8}Fe_{0.2}O_{3-\delta}$ (20.6$\times10^{-6}$ K^{-1} [124]). However, Pr based perovskite such as $Pr_{0.8}Sr_{0.2}MnO_{3-\delta}$ shows a TEC value of 9.5-10.1$\times10^{-6}$ K^{-1} [125] which is closely matched to that of BZCYYb. Consequently, Pr-based perovskite oxide may be used as potential cathode for SOFCs using BZCYYb electrolyte.

4.5 PROPERTIES OF CE DOPED COMPLEX PEROVSKITE $BA_3CA_{1.18}NB_{1.82}O_{9-\Delta}$

4.5.1 Electrical conductivity of Ce doped BCN18

The AC impedance spectra for the samples are conducted to measure the bulk and grain boundary conductivity of the samples. Typical Nyquist plots of the impedance spectra for sample BC(NC0.2) in wet air at 122 and 200^{o}C are shown in Fig. 4.9(a) and (b), respectively. The insets are the expanded views of the high frequency regions. The impedance spectra typically have three semi-circles corresponding to the bulk, grain boundary and electrode responses from high to low frequencies. As shown in the inset of Fig. 4.9(a) that at 122^{o}C, a semicircle related to the bulk conduction process in the high

frequency range (capacitance ~ 10^{-12} F cm^{-1}) can be clearly seen. With the temperature increased to 220°C, as shown in the inset of Fig. 4.9(b), only a portion of the semicircle corresponding to the bulk conduction response is observable in the high frequency range. When the temperature was further increased, the semicircle corresponding to the bulk conduction response can no longer be well defined and the bulk resistance can be then derived from the high frequency intercept of the intermediate frequency semicircle with the real axis. The semicircle in the intermediate frequency range is attributed to grain boundary responses (capacitance ~ 10^{-9} F cm^{-1}) while the spectrum in the low frequency range is due to the electrode response (capacitance ~ 10^{-4} F cm^{-1}) [58]. The other samples also have similar impedance spectrum evolution as a function of the testing temperature to that of BC(NC0.2).

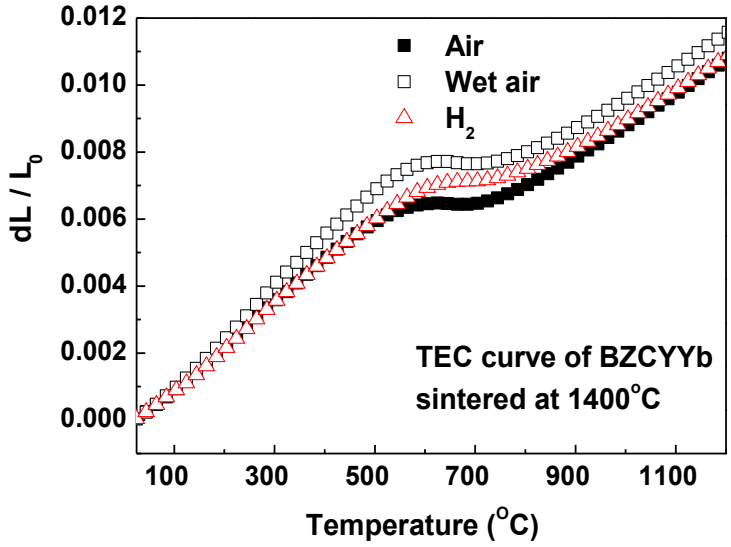

Figure 4.8 Thermal expansion behavior of BZCYYb sintered pellets in dynamic air, wet air and 5% H_2 balanced with 95% N_2.

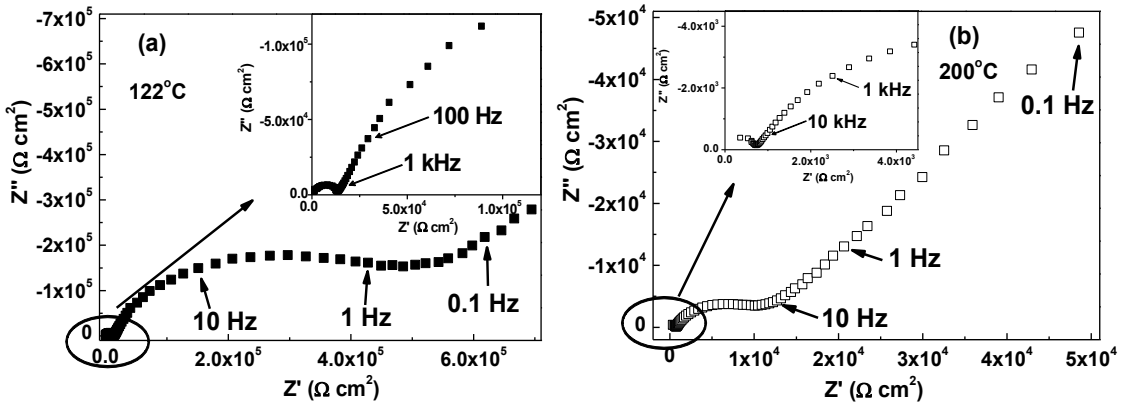

Figure 4.9 Nyquist plots for BC(NC0.2) in wet air at (a) 122°C, and (b) 200°C. Inset pictures are expanded views of high frequency regions.

Fig. 4.10(a) and (b) show the total conductivities of the samples in wet air and wet H_2, respectively. It can be seen that the introduction of Ce ions into either Ca or Nb sites presents a distinct effect on the conduction behavior. Sample B(CC0.1)N shows the lowest conductivity among the different samples both in air and in H_2 at the same testing conditions. As discussed above in the XRD and XPS analysis, most Ce^{4+} ions may probably be reduced to Ce^{3+} ions to be substituted into Ca^{2+} sites. A decrease in the grain size has also been observed for B(CC0.1)N (as shown in Fig. 3.19), resulting in an increase in grain boundary numbers and consequently an expected reduction in the total electrical conductivity. Another important factor that influences the electrical conductivity is the concentration of oxygen vacancies generated through doping. Substituting Ca^{2+} with either Ce^{4+} or Ce^{3+} will not lead to an increase of oxygen vacancies. Thus the decrease in conductivity for sample B(CC0.1)N can be viewed as a collective result of the above correlations. As for samples BC(NC0.1) and BC(NC0.2), the electrical conductivity are increased compared with the undoped BCN18, with sample BC(NC0.2) showing the highest conductivity among the different samples tested at

similar conditions (an enhancement of 78% in electrical conductivity is achieved). Doping Ce ions (either Ce^{4+} or Ce^{3+}) into Nb^{5+} sites will result in an enhancement of the B-sites disordering and an increase in the concentration of oxygen vacancies. In addition, as shown in Fig.3.19, an increase in grain size has been observed for BC(NC0.1) and BC(NC0.2) compared with that of BCN18. All these factors are expected to lead to an increase in the electrical conductivity, which has been confirmed by the conductivity data in Fig. 4.10.

In Fig. 4.10(a), by linearly fitting the slopes of the Arrhenius plots, the activation energies for samples BCN18, B(CC0.1)N, BC(NC0.1) and BC(NC0.2) in wet air are calculated to be 0.77, 0.73, 0.63, and 0.47 eV, respectively, clearly showing the effect of Ce doping on the crystal structure and consequently influence on the electrical conductivity. A larger decrease in activation energy is observed with Nb sites doped samples. This can be understood that more B-sites ions are disorderly distributed ("randomly" distributed) rather than ordered because of the Ce ions doping, thus the charged ions can move more easily, consistent with the reported data [32]. A tendency of decreased activation energy with increasing unit cell volume has also been observed for proton conductors with simple perovskite structure [54].

For samples tested in wet H_2 atmosphere as shown in Fig. 4.10(b), a decrease in activation energy at high temperature range (higher than 550^oC) has been observed, indicative of change in conduction mechanism. When the testing temperature increases, a decrease in proton conductivity is anticipated as a result of the dehydration of the oxide lattice due to the exothermal nature of reaction (2-1) [107]. A gradual change from proton conduction into mixed oxygen ion and proton conduction is expected. Electronic

conduction may also exist under high temperature regime [103]. Other proton conducting materials such as BCN18, $BaZr_{0.1}Ce_{0.7}Y_{0.2}O_{3-\delta}$, $BaZr_{0.9}Y_{0.1}O_{3-\delta}$, and $Sr_3CaZr_{0.5}Ta_{1.5}O_{8.75}$ also show change of shapes in the conductivity Arrhenius plots in wet H_2 atmospheres [24, 25, 42, 108].

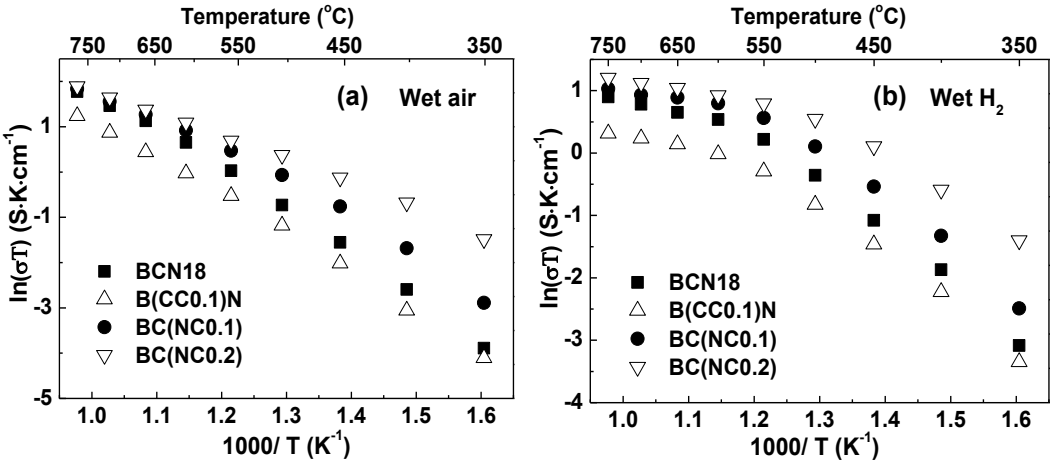

Figure 4.10 Arrhenius plots of total conductivity for samples (a) in wet air, and (b) in wet H_2.

Table 4.1 Summary of structural and electrical properties of the sintered samples.

Sample Denotation	Lattice Parameter (Å)	Average Grain Size (μm)	Conductivity @550°C (S·cm⁻¹)	
			Wet air	Wet H_2
BCN18 ($Ba_3Ca_{1.18}Nb_{1.82}O_{9-\delta}$)	8.4095	3.14	1.25×10^{-3}	1.51×10^{-3}
B(CCN0.1) ($Ba_3Ca_{1.08}Ce_{0.1}Nb_{1.82}O_{9-\delta}$)	8.4149	2.41	0.719×10^{-3}	0.905×10^{-3}
BC(NC0.1) ($Ba_3Ca_{1.18}Nb_{1.72}Ce_{0.1}O_{9-\delta}$)	8.4330	3.57	1.95×10^{-3}	2.13×10^{-3}
BC(NC0.2) ($Ba_3Ca_{1.18}Nb_{1.62}Ce_{0.2}O_{9-\delta}$)	8.4420	4.01	2.42×10^{-3}	2.69×10^{-3}

By separating the bulk and grain boundary conductivity, it is able to obtain detailed information on different contributions to the total conductivity. To evaluate the effect of introduction of Ce ions into Nb sites on the bulk and grain boundary conduction mechanisms, Fig. 4.11(a) and (b) show the Arrhenius plots of the bulk and grain boundary conductivity for samples BCN18 and BC(NC0.1) in wet air and wet H_2, respectively. Typically it is difficult to separate the grain boundary conductivity from the bulk conductivity when the testing temperature is high, however, in our experiments, because of the unique microstructure and characteristic of the BCN18 based samples, they can be separated up to 700^{o}C (See Fig. 4.11(a) inset). In wet air the activation energies for BCN18 bulk, BC(NC0.1) bulk, BCN18 grain boundary, and BC(NC0.1) grain boundary conduction are 0.53, 0.463, 1.10, and 1.12 eV, respectively, showing almost linear behavior in Arrhenius plots. In wet H_2 at temperatures below 550^{o}C, for bulk conduction, the activation energies for BCN18 and BC(NC0.1) are 0.57 and 0.55 eV, respectively. While at elevated temperatures higher than 550^{o}C, a decrease in activation energy for bulk conduction is clearly observed, with activation energy of 0.13 and 0.1 eV, respectively, characteristic of electronic conduction. It should be noted that the slope change of the bulk conduction proceeds gradually while there is little change for that of the grain boundary conduction. The activation energies for grain boundary conductivity are 0.88 and 0.89 eV for BCN18 and BC(NC0.1), respectively. Therefore, it can be concluded that the bowed behavior of the total conductivity plot above 550^{o}C is mainly attributed to the change in the mechanism of the bulk conduction.

In both air and H_2 atmospheres, substitution of Nb^{5+} with Ce ions leads to a decrease in activation energy as well as an increase in bulk conductivity. The activation

energy for grain boundary conduction remains almost the same with different substitution of Ce ions. However, the magnitude of the grain boundary conduction is significantly enhanced because of the substitution. This can be partly reflected by the influence of the grain sizes on grain boundary conductivity, with larger grain sizes showing enhanced grain boundary conductivity. Further, perhaps more importantly, doping Ce^{4+} and/or Ce^{3+} ions in the Nb^{5+} sites may lead to an increase in oxygen vacancies in the grain boundary region, resulting in higher grain boundary conductivity without changing the conduction mechanism. It is also noticed that at temperatures lower than 550°C, improvement of total conductivity in wet H_2 is observed compared with that in wet air for the samples, indicating enhancement of proton conduction in H_2 atmosphere (as shown in the inset in Fig. 4.11) [88]. Table 4.1 lists the conductivity values of the samples tested in different atmospheres at 550°C.

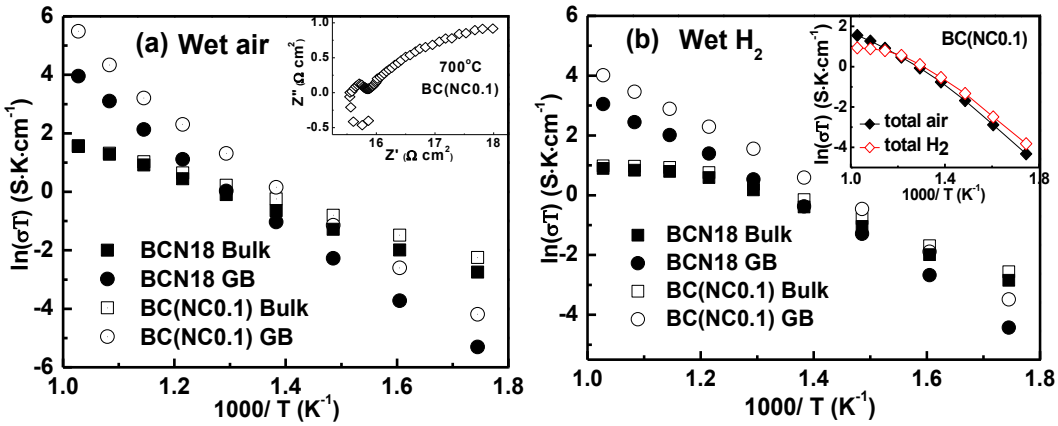

Figure 4.11 Arrhenius plots of bulk and grain boundary conductivity for sample BCN18 and BC(NC0.1) in (a) wet air and (b) wet H_2; Inset (a) is the Nyquist plot for BC(NC0.1) at 700°C in wet air, inset (b) is the Arrhenius plot for BC(NC0.1) in wet air and wet H_2.

4.5.2 Chemical stability of Ce doped BCN18

To evaluate the chemical stability of Ce doped BCN18 materials, the sintered pellets were exposed into boiling water and CO_2 atmosphere at elevated temperatures. Fig. 4.12(a) shows the XRD patterns of the pellets after boiling in water for 7 h. It can be seen that after boiling in water for 7 h, all the samples maintain pure perovskite structure with no detectable impurity phases. It is noticed that the peak intensity decreased after the treatment, especially for sample BC(NC0.2). This may be caused by the absorption of H_2O in the samples during treatment. FTIR spectrum study also confirmed the water adsorption on boiled $Ba_3CaNb_{1.75}Ti_{0.25}O_{9-\delta}$ samples as reported by Thangadurai [126].

The stability tests were also conducted in CO_2 atmosphere at 700^oC for 4 h as well as in wet 3 vol% CO_2 (air as the balance gas, 3 vol% H_2O) at 700^oC for 24 h, both with a flow rate of 50 mL min^{-1} to evaluate the stability in carbon dioxide environments. XRD patterns of the samples after exposures are presented in Fig. 4.12(b) and (c), respectively. It can be seen that no impurity phases have been detected for the samples treated in CO_2 environment, suggesting no reaction taken place between CO_2 and the samples. Inspection of the samples after treatments revealed no apparent change in either color or morphology of the samples, consistent with the XRD results. Consequently, the introduction of Ce ions into either B' site or B'' site did not show any detrimental effect on the chemical stability for BCN18. Combined with the conductivity results, the doped BCN18 system turns to be a very promising intermediate temperature proton conductors, with respect to the stability tests mentioned above for $Ba(Ce,Zr)O_3$ based simple perovskite systems. For instance, $BaCe_{0.7}Zr_{0.2}Y_{0.1}O_{3-\delta}$ will discompose when either treated in boiling water for 6 h or held in carbon dioxide atmosphere for 2 h at 900^oC [56];

even for $BaCe_{0.3}Zr_{0.5}Y_{0.2}O_{3-\delta}$, impurity phase is formed after exposure to CO_2 at 900°C for 3h [57]. $BaCe_{0.45}Zr_{0.45}Sc_{0.2}O_{3-\delta}$ has been reported to be stable in pure CO_2 up to 900°C, but the total conductivity is relatively low, only 4.49×10^{-4} S·cm^{-1} at 600°C in air [58].

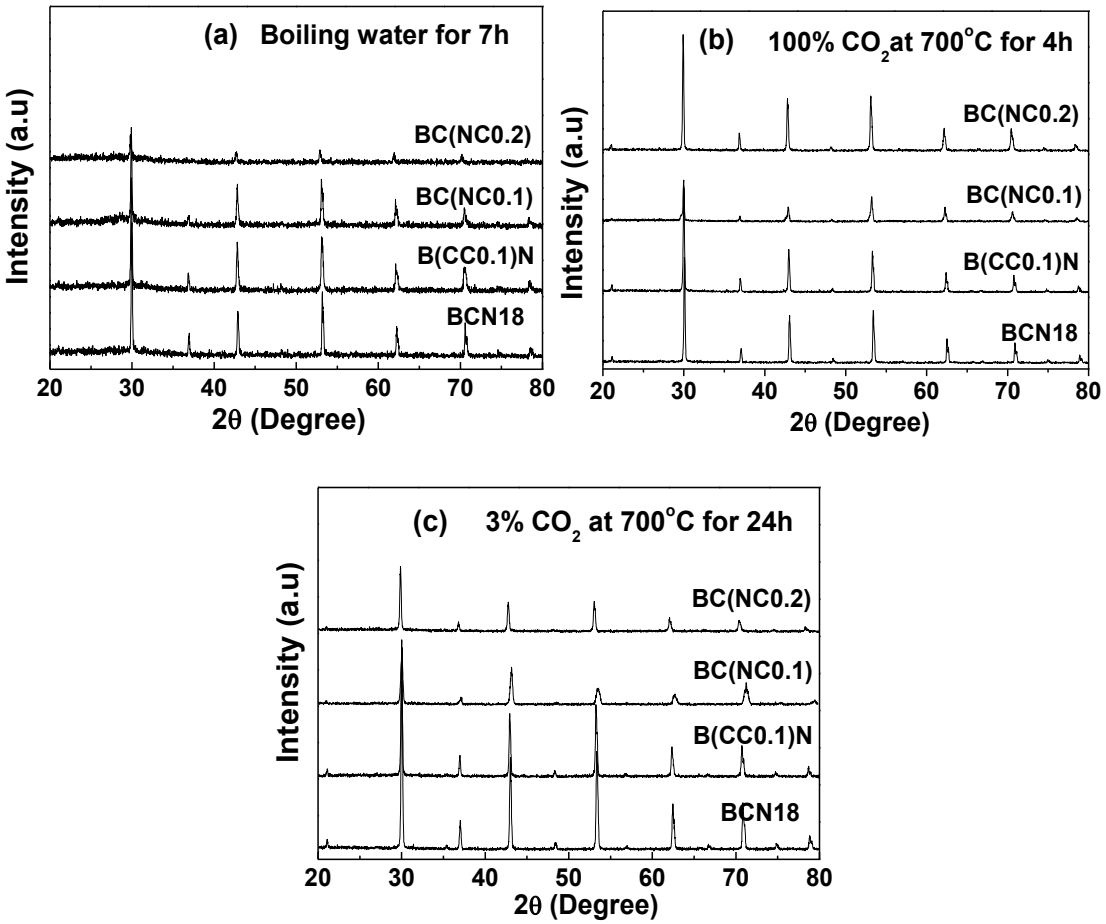

Figure 4.12 (a) XRD patterns of the sintered pellets after exposure in boiling water for 7 h, (b) XRD patterns of the sintered pellets after exposure in 100% CO_2 at 700°C for 4h, (c) XRD patterns of the sintered pellets after exposure in 3% CO_2 + 3% H_2O at 700°C for 24 h.

4.5.3 Thermal expansion measurement of $Ba_3Ca_{1.18}Nb_{1.62}Ce_{0.2}O_{9-\delta}$

The thermal expansion coefficient (TEC) matching among the components in a device is of crucial importance for real applications in order to minimize the thermally induced stresses during the thermal cycling process. For instance, TEC mismatch

between the electrolyte and the cathode in SOFCs can potentially lead to cracking in the electrolyte-cathode interface, and even to the spallation of the cathode from the electrolyte surface. Fig. 4.13 shows the thermal expansion behavior of sample $Ba_3Ca_{1.18}Nb_{1.62}Ce_{0.2}O_{9-\delta}$ (BC(NC0.2)) measured in air and 5% H_2/95% N_2 forming gas from 150 to 1000^oC. Almost linear curves are obtained in the entire temperature range studied, indicating no structural transformation within this temperature range. The TEC value from 150 to 1000^oC for BC(NC0.2) is calculated to be 14.73×10^{-6} and 15.03×10^{-6} K^{-1} in air and in 5% H_2, respectively. The lattice expansion observed at elevated temperatures in reducing atmosphere may be attributed to the loss of lattice oxygen and the formation of oxygen vacancies due to low oxygen partial pressure [127]. The TEC values show good compatibility with typical intermediate temperature cathode materials such as $La_{0.6}Sr_{0.4}Co_{0.2}Fe_{0.8}O_{3-\delta}$ (17.5×10^{-6} K^{-1}) and $BaCo_{0.7}Fe_{0.2}Nb_{0.1}O_{3-\delta}$ (14.64×10^{-6} K^{-1} from 200 to 1000^oC) [128, 129], indicating that doped BCN18 can be potentially applied as the electrolytes for intermediate-temperature SOFCs.

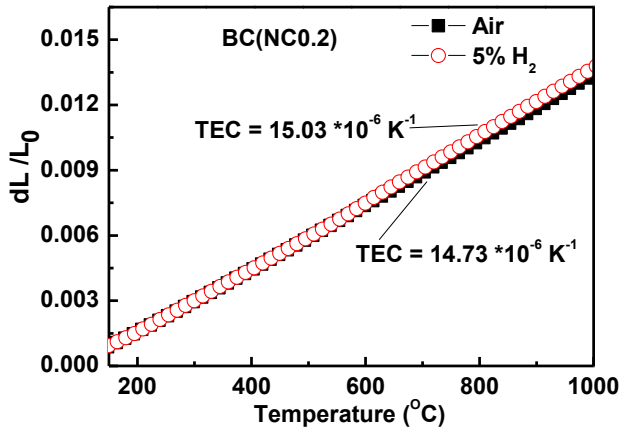

Figure 4.13 Thermal expansion behavior of BC(NC0.2) sintered pellets in air and in forming gas with 5% H_2 balanced with 95% N_2.

4.6 PROPERTIES OF $BA_3CA_{1.18}NB_{1.82-X}Y_XO_{9-\Delta}$ SYSTEM

4.6.1 Electrical conductivity of $Ba_3Ca_{1.18}Nb_{1.82-x}Y_xO_{9-\delta}$ system

Fig. 4.14 shows the Arrhenius plot of the conductivities of the samples in wet air (3vol% H_2O) between 400 and 800^oC. The sample surfaces were polished to remove the surface impurities, especially for sample BCNY0.5, before applying Pt paste on the surface of the samples for electrical measurement. The activation energy values for the samples are 0.75 ±0.02, 0.55 ±0.01, 0.59 ±0.01, 0.54 ±0.01, and 0.52 ±0.01 eV, for BCN18, BCNY0.1, BCNY0.2, BCNY0.3, and BCNY0.5, respectively. The conductivity increased with decreased activation energy when Nb was partially substituted by Y. The total conductivity increased before x reaches 0.3 and then decreased with x=0.5. As it has been reported that in wet atmospheres, protonic defects are formed mainly due to dissociative adsorption of water in the presence of oxygen vacancies [130]. The formation of protonic defects is a prerequisite for the proton transport followed by hopping of protons between two adjacent oxygen ions within the perovskite structure. As discussed before, on the one hand, the precipitation of CaO secondary phase (which is insulator) deteriorated the conductivity; also the introduction of $(V_O^{\cdot\cdot}Y_{Nb}'')$ which not only traps for oxygen vacancies but also as nucleating centers for the formation of ordering vacancy clusters [43]. These defect associations blocked the movement of oxygen vacancies for BCNY0.5. The highest effective oxygen vacancy concentration was therefore determined by the two opposite effects to be x=0.3. The resulting highest conductivity for BCNY0.3 is also indicative of direct connection between free oxygen vacancies and proton conductivity. With the increase in the testing temperature, water desorption occurs, resulting in a decrease in the concentration of charge carriers while the proton mobility increases

because proton conduction is a thermally activated process [131]. The combination of lowered proton concentration and improved mobility leads to the leveling off in the conductivity curves. At the same time the electronic hole and/or oxygen ionic conductions appear and are expected to dominate when temperature further increases [26]. In wet air, oxygen can fill into oxygen vacancies resulting in holes via equation (2-3).

The effects of ionic and electronic hole conduction add up at high temperature range. In all, among the samples examined, BCNY0.3 shows the highest conductivity of 5.3×10^{-3} $S\cdot cm^{-1}$ at 600°C in wet air, a value comparable or sometimes even higher than that of Zr doped $BaCeO_3$ based materials. Table 4.2 compares the conductivity properties for BCNY0.3 and $Ba(Zr,Ce)O_3$ based materials and it can be that BCNY0.3 shows higher conductivity than $BaZr_{0.3}Ce_{0.7}Y_{0.1}O_{3-\delta}$ while exhibits much better stability towards CO_2 and/or water.

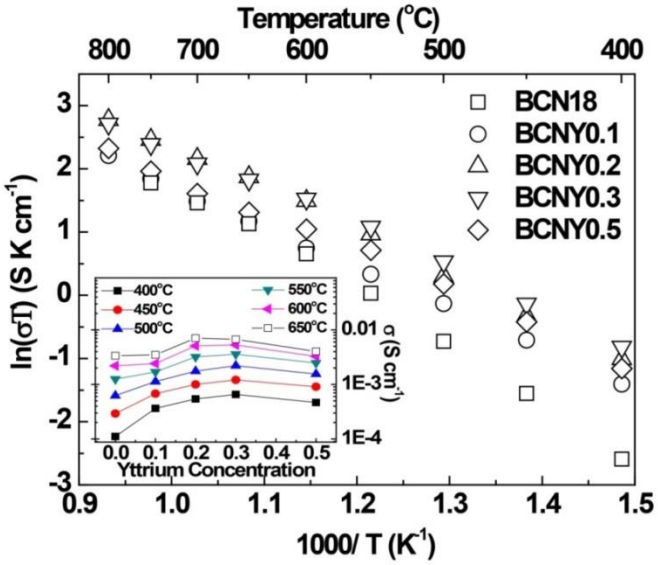

Figure 4.14 Arrhenius plots of the total conductivity of the samples in humidified air. Inset is the conductivity as a function of yttrium concentration.

The bulk and grain boundary (GB) conductivity can be separated at low temperature regime due to different responses with frequency. Fig. 4.15 shows the grain and grain boundary conductivity for sample BCNY0.3 measured at ambient air, wet air and wet H_2, respectively. From Fig. 4.15(a) we can see that the bulk conductivity changed as a function of oxygen partial pressure. The bulk conductivity increases due to the introduction of water, which is indicative of proton conduction in bulk areas for the samples. Activation energy of 0.57 eV is also characteristic of proton conduction. The grain boundary conductivity, on the other hand, does not obey the trend as bulk conduction does. The sample in wet air and wet H_2 does not show higher GB conductivity than in ambient air, which indicates that the proton is not the dominant charge carriers in the grain boundary areas. Rather, *p*-type (electronic hole) conduction should appear at higher oxygen partial pressure under the reaction (2-3) and (2-4).

Higher activation energy in air than in H_2 (0.77 vs. 0.70 eV) for BCNY0.3 is also indicative of the enhancement of electronic hole conduction. In all, the grain boundary activation energy is higher than bulk activation energy, indicating the existence of electronic hole conduction in grain boundaries, in contract with the bulk areas which are dominantly proton conduction. For BCN18 and BCNY0.5 samples, same trend on bulk and grain boundary conductivity were also observed.

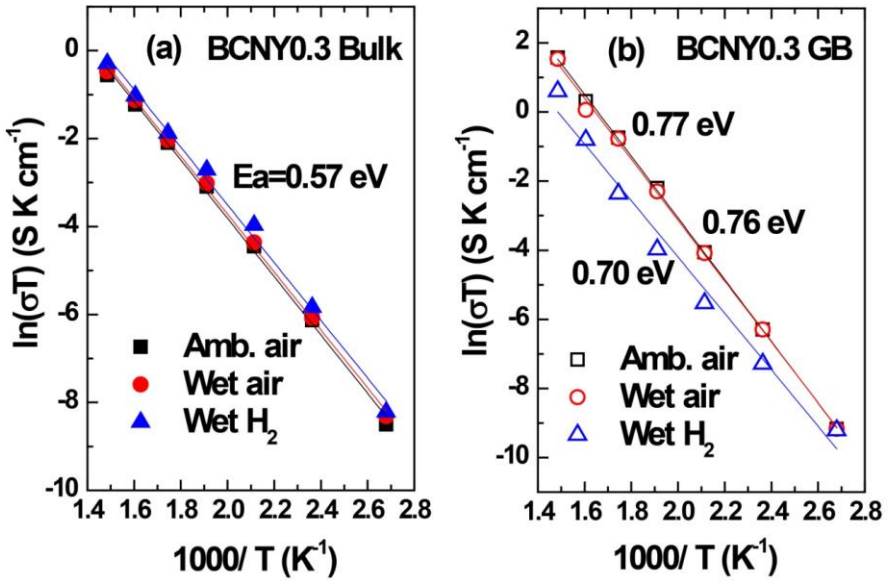

Figure 4.15 Bulk and Grain boundary (GB) conductivity for BCNY0.3 at different atmospheres.

Fig.4.16 shows the bulk and grain boundary conductivity in different atmospheres for selected samples (Ambient air, wet air, and wet H_2). In all it can be seen that BCNY0.3 shows the highest bulk conductivity in all atmospheres, followed by BCNY0.5, with BCN18 shows the lowest bulk conductivity (Fig 4-16(a, c, e)). This can be explained in accordance with previous results that the introduction of up to 30% yttrium into BCN18 (BCNY0.3) introduced more oxygen vacancies into the system thus improved the bulk proton conductivity, while relative less oxygen vacancies exhibited in BCNY0.5 bulk areas, showing lower bulk conductivity.

The activation energy for the bulk conduction ranges from 0.52-0.59 eV, characteristic of proton conduction within error. For the grain boundary conductivity among the samples, the activation energy follows the trend *Ea*:

BCN18<BCNY0.3<BCNY0.5 (Fig. 4.16(b, d, f). The increase of activation energy in ambient and wet air, as mentioned, is caused by the p-type (electronic hole) conductivity induced by Y-doping via reaction (4-6)

$$1/2O_2 + Y_2O_3 \xrightarrow{Nb_2O_5} 2Y_{Nb}^{''} + 4O_O^{\times} + 4h^{\bullet} \qquad (4\text{-}6)$$

From oxidation states point of view, the introduction of Y caused the valence change of Nb^{+5} into Nb^{+4}, leading to a *p*-type electronic conduction, in consistent with XPS results measured. For Fig. 4.16(f), as it has been proved that BCN18 is pure proton conduction at reducing atmospheres [28], the activation energy for proton conduction in the grain boundary area is higher than in bulk area for BCN18. Apparently there is no electronic hole (*p*-type) conduction in reducing atmospheres, thus for BCNY0.3 and BCNY0.5, the increased activation energy, is either due to the materials' intrinsic characteristic for proton conduction, or as a combination of intrinsic proton conduction (with even higher activation energy) mixed with electronic conduction (with much lower activation energy). As a consequence, the improvement of grain boundary conductivity for BCNY0.3 and BCNY0.5 is either due to the intrinsic improved proton conductivity or as a combination of improved proton conductivity mixed with electronic (e^-) conductivity. Thus it can be concluded that the introduction of Y into BCN18 enhanced the proton conductivity, mainly at the bulk areas, due to the increased content of oxygen vacancies. On the other hand, the Y-doping also introduced some level of electronic conductivity, mainly at the grain boundary areas, as a compensation of proton conductivity for the grain boundary conductivity.

The theoretical and measured open circuit voltage values for BCNY0.3 with the configuration of 3vol%H_2O-H_2/Pt │BCNY0.3 │Pt/Air are shown in Fig. 4.17. The

effective ionic transport numbers can be calculated from $T = OCV_{measured}/OCV_{theoretial}$. It can be seen that an almost pure ionic behavior is observed at lower temperatures. The deviation of measured OCV from theoretical OCV (calculated from Nernst equation) increases with temperature, especially at temperatures higher than 600^{o}C, which indicates that the ionic transport number decreases with increasing operating temperature, demonstrating increased influence of electronic conductivity at higher temperatures. This phenomenon can be understood through equation (2-3) and (4-1), where electronic and proton mixed conduction appear. In this case, the materials may suitable for the following applications, that for intermediate temperature SOFC application where pure ionic conduction is needed; and that for high temperature hydrogen separation membranes where proton/electronic mixed conduction is needed.

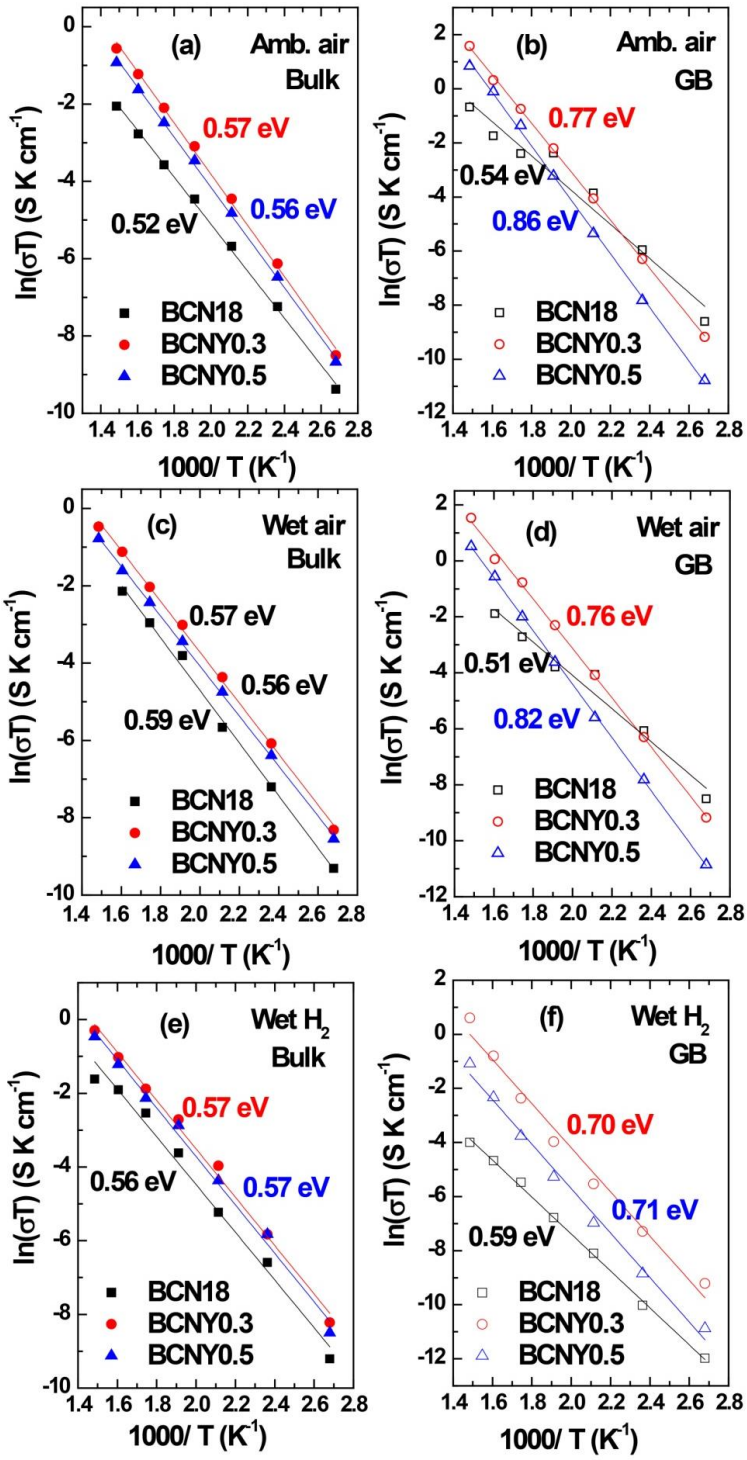

Figure 4.16 Bulk and Grain boundary (GB) conductivity of selected samples measured at different atmospheres.

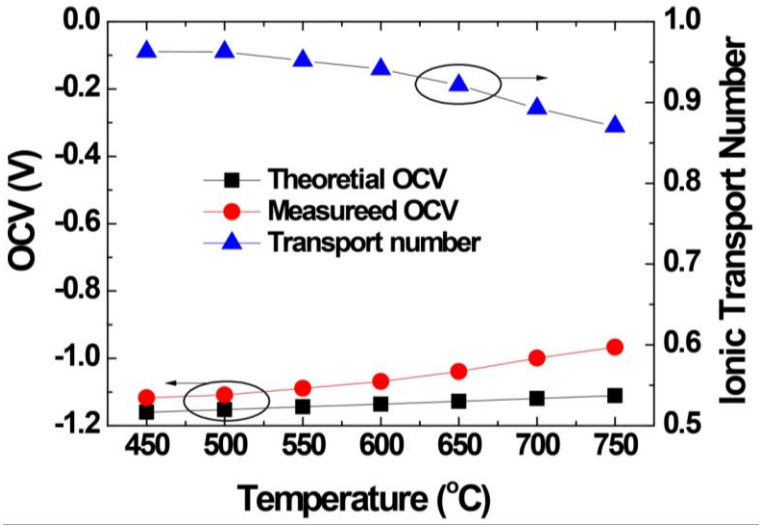

Figure 4.17 Theoretical and measure4d OCV values for BCNY0.3 with 3vol%H_2O-H_2/Pt │BCNY0.3 │Pt/Air and ionic transport number.

4.6.2 Chemical stability of BCNY systems

For each application, a chemical stable material is prerequisite. To investigate the chemical stability of the Y-doped BCN18 compounds, the sintered pellets were ground into powders and then exposed to boiling water for 24 h. The treated powders were examined by XRD, as shown in Fig. 4.18. The XRD pattern of $BaZr_{0.1}Ce_{0.7}Y_{0.1}Yb_{0.1}O_{3-\delta}$ (BZCYYb) powder treated in boiling water for 4 h was compared as reference. As seen in Fig. 4.18, simple perovskite structure $BaCeO_3$ based proton conductors readily decomposed in boiling water via reaction (2-6) and (2-7). $BaCeO_3$ decomposed into prevalent CeO_2 and $BaCO_3$ impurity phase, while $Ba(OH)_2$ was dissolved in water. While complex perovskite structured BCN18 based proton conductors remain pure perovskite structure even after exposure in boiling water for 24 h. Although amorphization may exists after long time treatment due to the leaching of Ba and Ca in the surface layers as studies by T. Schober [96], it is worth mentioning that

BCN18 based proton conductors are thermal-dynamically more stable than BZCYYb when treated in boiling water. And the introduction of Yttrium did not show clear detrimental effect on the stability property.

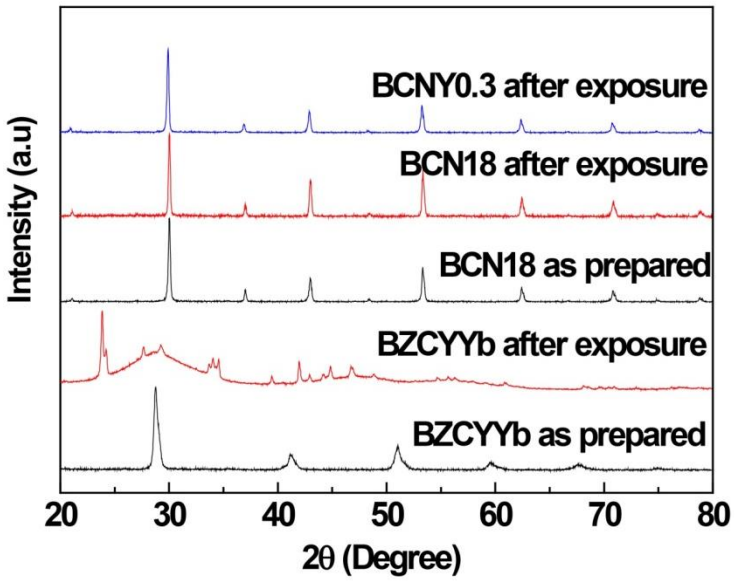

Figure 4.18 XRD patterns of BCN18 and BCNY0.3 sample powders after exposure to boiling water for 24 h. The XRD pattern of $BaZr_{0.1}Ce_{0.7}Y_{0.1}Yb_{0.1}O_{3-\delta}$ (BZCYYb) powder treated in boiling water for 4 h is presented as reference.

The sintered pellets were also exposed to air containing 3vol% CO_2 and 3vol% H_2O at 700°C for 24 h and pure CO_2 at 700°C for 4 h. The XRD patterns of the surfaces of the pellets were collected after the treatments (shown in Fig. 4.19(a) and (b)). The BZCYYb powder samples after same treatment were also added as reference. No secondary phases can be observed for the differently treated BCN18 sintered pellets in all the XRD patterns, consistent with the reported results for BCN18 based system [126]. Considering the environmental atmospheres for field applications, such stability tests

suggest that the Y-doped BCN18 samples show sufficient chemical stability even in harsh conditions and the stability is not affected by the yttrium concentration.

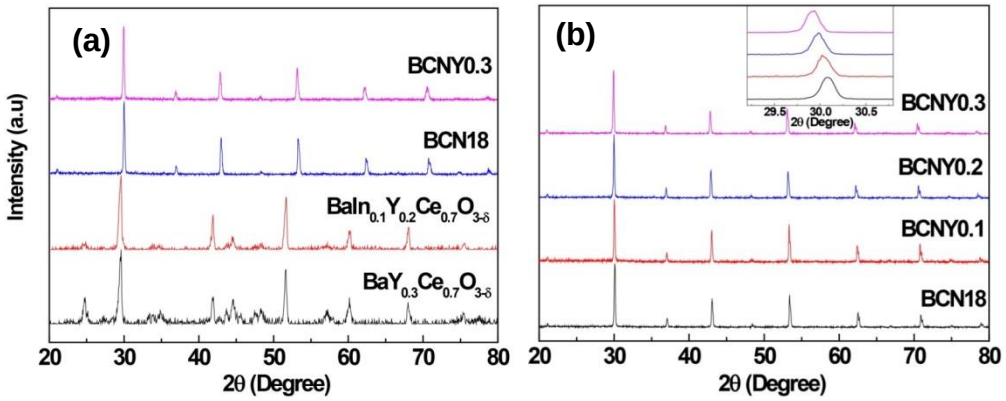

Figure 4.19 (a) XRD patterns of the sintered pellets after exposure to air with 3% CO_2 + 3% H_2O at 700^oC for 24 h, (b) XRD patterns of the sintered pellets after exposure to 100% CO_2 at 700^oC for 4h.

Fig. 4.20 shows the TGA results for BCNY0.3 and BCNY0.5 under exposure of 20% CO_2/80% ambient air. The weight loss during heating is due to the loss of water, firstly external of structure, followed loss of structural water vapor and loss of oxygen at high temperatures. It is noted that starting at 1170 ^oC a weight gaining peak was observed for sample BCNY0.5. The impurities among BCNY0.5, is accounted for the weight gaining, probably due to the absorption of CO_2 by BaO and CaO. Totally, a weight loss of around 2 wt % was observed for the samples. If we consider simple perovskite $BaCe_{1-x}Zr_xY_yO_{3-\delta}$, a weight gaining of 13 wt% was obtained for $BaCe_{0.9}Y_{0.1}O_{3-\delta}$ due to the catching of atmospheric CO_2 and decomposition of the materials to $BaCO_3$ and CeO_2 [105]. A weight gaining of 1.7 wt % was also observed for 20% Zr doped $BaCe_{0.65}Zr_{0.2}Y_{0.15}O_{3-\delta}$ as a compensation of uptake of CO_2 and loss of water vapor and oxygen during heating [88]. It is evident from the TGA results that effect of the decomposition of

the materials into $BaCO_3$ is neglected. It is evident that unlike $BaCeO_3$ based simple perovskite structured proton conducting ceramics which readily react with CO_2 to form CeO_2 and decomposed into $BaCO_3$ under 1100°C, $Ba_3Ca_{1.18}Nb_{1.82-x}Y_xO_{9-\delta}$ based complex perovskite system is thermal-dynamically much more stable in CO_2 containing atmosphere. Considering the environmental atmospheres for field applications, the water and CO_2 stability tests results suggest that the Y-doped BCN18 samples show sufficient chemical stability even in harsh conditions and the stability is not affected by the yttrium doping concentration up to 0.3. Table 4.2 compares the chemical stability properties for selected samples. It can be seen that BCNY0.3 shows very promising chemical stability among the reported intermediate temperature perovskite proton conductors and acceptable conductivity compared with state-of-the-art $Ba(Zr,Ce)O_3$ based proton conductors.

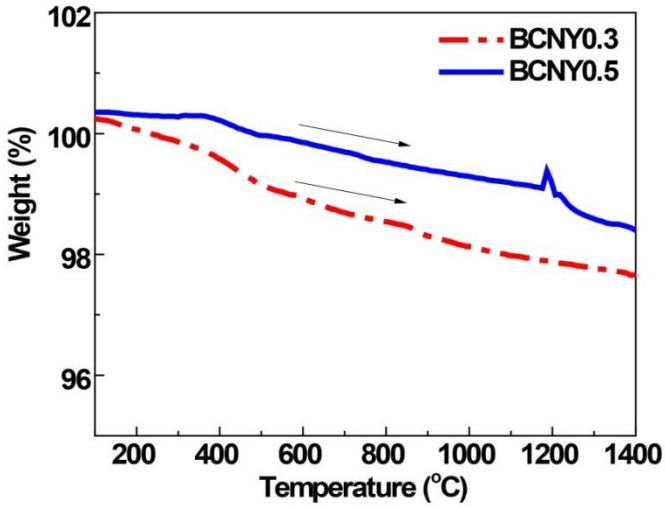

Figure 4.20 TG measurement of BCNY0.3 and BCNY0.5 under 20% CO_2/80% air.

Table 4.2 Stability and conductivity properties for selected proton conductors, *: the test was conducted under 3%CO_2+3%H_2O balanced with air.

Materials	Conductivity@600°C (S cm^{-1})	Resist in Boiling Water	Resist in Pure CO_2	Resist in CO_2 and water vapor	Reported Group
$Ba_3Ca_{1.18}Nb_{1.52}Y_{0.3}O_{9-\delta}$	5.3×10^{-3}, wet air	>24 h	>4 h@700°C	>24 h @700°C*	This work
$BaZr_{0.1}Ce_{0.8}Y_{0.1}O_{3-\delta}$	1.0×10^{-2}, wet H_2	-	<2h@900°C	-	H. Iwahara [103]
$BaZr_{0.2}Ce_{0.7}Y_{0.1}O_{3-\delta}$	-	<6 h	<2 h@900°C	-	Z. Zhong [56]
$BaZr_{0.3}Ce_{0.5}Y_{0.2}O_{3-\delta}$	4.5×10^{-3}, synthetic air	-	<3 h@900°C	-	E. Traversa [57]
$BaZr_{0.4}Ce_{0.4}Y_{0.2}O_{3-\delta}$	-	-	<2 h@650°C		Z. Shao [132]
$BaZr_{0.45}Ce_{0.45}Sc_{0.1}O_{3-\delta}$	4.9×10^{-4}, amb. air	-	<1 h@900°C	-	J. Irvine [58]
$BaTa_{0.1}Ce_{0.7}Y_{0.2}O_{3-\delta}$	-	>3 h	>3 h@900°C	<24 h @700°C*	W. Liu[73]
$BaIn_{0.2}Ce_{0.7}Y_{0.1}O_{3-\delta}$	5.0×10^{-3}, wet air	-	-	<24 h @700°C*	F. Chen [17]

4.7 PARAMETERS INFLUENCING THE ELECTRICAL CONDUCTIVITY

There are many parameters that influence the electrical conductivity for the materials. First of all, the materials selection is the most important part for the conductivity. In our study the $BaCeO_3$ shows the highest conductivity; the $Ba_{1-x}Sr_xCe_{0.8}Y_{0.2}O_{3-\delta}$solid solutions show conductivity values between that of BCY and SCY, and $BaZr_xCe_{1-x-y}Y_yO_{3-\delta}$ possess a conductivity value between that of $BaCeY_yO_{3-\delta}$ and $BaZrY_yO_{3-\delta}$.Complex perovskite structured BCN18 shows the lowest conductivity.

Secondly, for a specific material, the bulk and grain boundary contribute to the total conductivity of the material. Generally for the proton conductors investigated here,

the activation energy of grain boundary conductivity is higher than that of bulk conductivity, which means that at low temperature regime, the grain boundary is the rate limit factor for the total conductivity.

For the bulk conductivity, it is usually assumed there is no impurity in the bulk area. Thus for single phased materials, the bulk conductivity is not related with the trace amount of impurity level. (For composite materials, the bulk conductivity should be affected by both compositions). However, the orientation/ordering of the cations in the structure, should affect the bulk conductivity. It is believed that the oxygen vacancy is more related with B-site cation rather than A-site ion. An oxygen atom forms two-short bonds with B cations, and two long bonds with A cations in the perovskite, which means that an oxygen vacancy is more strongly trapped by a B'-O-B'' pair than by a A-O-A pair in $A(B'B'')O_3$ perovskite [63]. In this case, the ordering of B-site cations will directly lead to the ordering of oxygen vacancies, which will in turn block the oxygen movement and thus deteriorate the proton conductivity.

On the other hand, the impurity of the materials shows a larger impact on the grain boundary conductivity. It is believed that tiny amount of impurities are located in the grain boundary areas, which will sometimes show huge impact on the total conductivity. It is reported the ppm level amount of Si residue in grain boundary area greatly affected the total conductivity [133].

In this case, on the one hand, people are trying to grow larger grains for the materials, and even single crystals to prepare grain-boundary-free materials/thin films to eliminate the grain boundary effect. For example, Traversa reported that the

$BaZr_{0.8}Y_{0.2}O_{3-\delta}$ thin film prepared by pulsed laser deposition on (100)-oriented MgO substrates shows a proton conductivity of 0.11 S cm^{-1} at 500^{o}C [52].

However, if a material itself is not purified enough, showing trace amount of impurity characterized even by instrument XRD (which indicates the impurity level is around or higher than 5 wt%), the above mentioned grain boundary effect on the total conductivity is not always the true. In this case one can assume the total conductivity is a combination of the contributions. The secondary phases segregate at the grain boundaries. However, since there are large amount of the secondary phases, the material can be treated as composite materials of the main phase and the secondary phase. Besides the grain boundary conductivity of the main phase, the secondary phases also play a role in the total conductivity.

Sintering temperature can affect the total conductivity by altering the grain size for the material. In our case, the BZCYYb sintered at 1400^{o}C shows higher conductivity than the sample sintered at 1350^{o}C, due to the increased grain sized showing a increased bulk conductivity as well as reduce pores and pinholes. However, further increased sintering temperature on the one hand may improve grain growth of the sample, on the other, it will lead to increased impurity and secondary phase levels segregated in the grain boundary areas due to the element vaporizations during higher temperature sintering process (such as Ba vaporization at above 1500^{o}C).

In all, the conductivity of the proton conductors are consists of bulk conductivity and grain boundary conductivity. The bulk conductivity can be influence by the intrinsic ordering of the cations, the grain size distribution of the materials and the densification of the materials. The grain boundary conductivity is mainly affected by the impurities

segregated in the grain boundary areas. The species of the impurities, the charge carrier the impurities bring, and the amount of the impurities will influence the exhibit grain boundary conductivity and thus the affect the total conductivity.

4.8 DISCUSSION CONCERNING THE CHEMICAL STABILITY

For chemical stability of a material, it can be categorized into thermal dynamic stability and kinetic stability. Thermal dynamic stability is the intrinsic chemical stability property for a material, which is related with the thermal dynamic behaviors of the metal oxides. The HSC Chemistry software can be used to calculate the thermal dynamic equations for many common reactions by providing the database for Enthalpy (H), Entropy (S) and Specific Heat Capacity (C) [97].

For some of the materials, although it is thermal dynamically not stabile, it could be kinetic stable. For example, in our study [80], for $BaCeO_3$ based proton conductors, it is thermal dynamically not stable below 450^{o}C. However in the presence of water vapor, after water reacting with a few surface monolayers of $BaCeO_3$, since fewer water molecules penetrate into the grain boundaries compared with those in liquid water environment, the dissolution of $Ba(OH)_2$ in water vapor would be very slow, and the subsequent reaction rate for the decomposition of $BaCeO_3$ would be expected to be much slower than that in liquid water.

For the search of chemical stable proton conducting materials, the ultimate goal is to find materials that are thermal dynamically stable. While sometimes, it is difficult to find a proton conductor which possesses both high conductivity and excellent thermal dynamic stability. In this case, people are trying to modify the materials to be kinetic

stable in specific situations and conditions; one of such example is the $BaZr_{0.1}Ce_{0.7}Y_{0.1}Yb_{0.1}O_{3-\delta}$ proton conductor, which shows remarkable chemical stability under certain conditions [59].

4.9 SUMMARY

We measure the electrical conductivity property, including the bulk and grain boundary conductivities, the chemical stabilities towards water and/or CO_2, as well as the thermal expansion properties of selected proton conductors.

For $Ba_{1-x}Sr_xCe_{0.8}Y_{0.2}O_{3-\delta}$ system prepared from modified Pechini method, the conductivity tests indicated that $Ba_{1-x}Sr_xCe_{0.8}Y_{0.2}O_{3-\delta}$ possessed the electrical conductivity between $BaCe_{0.8}Y_{0.2}O_{3-\delta}$ and $SrCe_{0.8}Y_{0.2}O_{3-\delta}$. The conductivity decreased and the activation energy increased with the increase in Sr content in $Ba_{1-x}Sr_xCe_{0.8}Y_{0.2}O_{3-\delta}$. The stability tests indicated that the resistance to boiling water for $Ba_{1-x}Sr_xCe_{0.8}Y_{0.2}O_{3-\delta}$ was between that of $BaCe_{0.8}Y_{0.2}O_{3-\delta}$ and $SrCe_{0.8}Y_{0.2}O_{3-\delta}$. Contrary to the reported data, $Ba_{1-x}Sr_xCe_{0.8}Y_{0.2}O_{3-\delta}$ was less stable than $BaCe_{0.7}Zr_{0.2}Y_{0.1}O_{3-\delta}$ when exposed to boiling water. Due to the feasibility of the reaction with CO_2 for both $BaCe_{0.8}Y_{0.2}O_{3-\delta}$ and $SrCe_{0.8}Y_{0.2}O_{3-\delta}$, it was not surprising that $Ba_{1-x}Sr_xCe_{0.8}Y_{0.2}O_{3-\delta}$ was also not stable in CO_2 containing atmospheres.

The conductivity as a function of sintering temperature for $BaCe_{0.7}Zr_{0.1}Y_{0.1}Yb_{0.1}O_{3-\delta}$ proton conductor has been investigated. An optimum sintering temperature of 1400^oC has been obtained, resulting in a compromise between densification of samples which will improve the conductivity, and segregation of secondary phases which will deteriorate the conductivity when sintered at high

temperatures. The thermal expansion coefficient values for $BaCe_{0.7}Zr_{0.1}Y_{0.1}Yb_{0.1}O_{3-\delta}$ are 9.1-9.8$\times 10^{-6}$ K^{-1} from 25 to 1200^{o}C, which is favorably matched to that of Pr based cathode materials such as $Pr_{0.8}Sr_{0.2}MnO_{3-\delta}$ for SOFC applications. The conductivity property of co-precipitated $BaCe_{0.7}Zr_{0.1}Y_{0.1}Yb_{0.1}O_{3-\delta}$ powders sintered via two-step sintering method has also been investigated. Since there are trace amount of impurities in the as prepared powders, compared with conventional sintering methods, improved conductivity was obtained for the two-step sintered sample pellet, which was largely attributed to the improved grain boundary conductivity as a result from fewer amounts of impurity defects in the grain boundaries.

The effects of Ce ions substituted with either Ca or Nb for complex perovskite $Ba_3Ca_{1.18}Nb_{1.82}O_{9-\delta}$ on the conductivity have also been investigated. Ce substituted with Nb ions enhances electrical conductivity, especially the grain boundary conductivity. The introduction of Ce ions into Ca and/or Nb sites does not show any detrimental effect on the chemical stability for BCN18 system, demonstrating very satisfactory chemical stability compared with that of cerate based simple perovskite proton conductor systems. The thermal expansion coefficient value is larger than conventional electrolyte materials, showing good compatibility with typical intermediate temperature cathode materials in SOFC area.

We further investigated the $Ba_3Ca_{1.18}Nb_{1.82-x}Y_xO_{9-\delta}$ system. The conductivity increased with decreased activation energy when Nb was partially substituted by Y. The total conductivity increased before x reaches 0.3 and then decreased with x=0.5. The introduction of Y into the BCN18 system improved the bulk proton conductivity, as well as introducing electronic conductivity in the grain boundaries. As an optimum

composition, $Ba_3Ca_{1.18}Nb_{1.52}Y_{0.3}O_{9-\delta}$ shows predominantly proton conduction below 600^{o}C. The improved proton conductivity, coupled with high chemical stability, makes $Ba_3Ca_{1.18}Nb_{1.52}Y_{0.3}O_{9-\delta}$ a promising electrolyte material for intermediate-temperature solid oxide fuel cells.

CHAPTER 5

SOFC APPLICATION EVALUATION FOR PROTON CONDUCTING CERAMICS PERFORMED AS ELECTROLYTE MEMBRANES

5.1 INTRODUCTION

Proton-conducting solid oxide fuel cells (PC-SOFCs) have the unique property of conducting protons from the anode (hydrogen electrode) to the cathode (oxygen electrode), while producing water at the cathode side which avoids fuel dilution problems for SOFCs as compared to conventional oxygen-ion-conducting electrolytes. Furthermore, solid oxide electrolysis cells (SOECs) using proton-conducting electrolyte can produce pure and dry hydrogen on the hydrogen electrode, a significant advantage compared with those using oxygen-ion-conducting electrolytes where hydrogen is produced concurrently with steam requiring further drying steps [2]. In addition, the lower activation energy and relatively high proton conductivity at intermediate temperatures attainable from proton conducting oxides enables reduced operating temperature PC-SOFCs, potentially lowering the cost and enhancing the durability and reliability of SOFC systems [1].

For the fabrication of the SOFC single cells, there are several considerations that need to be considered, such as the compatibility among the components, which includes the chemical compatibility, i.e., the reaction between the anode/cathode and the electrolyte, and the thermal expansion coefficient compatibility among the components; the catalytic activity for the electrode materials is also an active area of interest; the

sintering profile for the fuel cells, which will thus influence the microstructures of the components, in also of crucial importance for the performance of the fuel cells. In this chapter, we demonstrated the fabrication of proton conducting SOFCs by applying the studied proton conducting ceramics as electrolyte membranes. A novel two-step co-sintering method has been adopted for the fabrication of the preparation of the single cells and had been proved promising.

5.2 EXPERIMENTAL

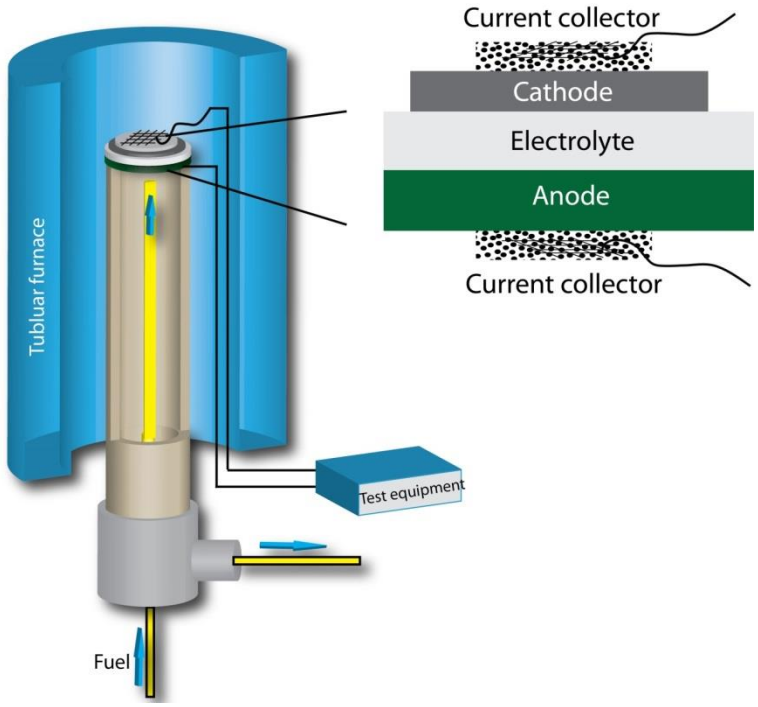

Figure 5.1 A schematic diagram showing the experimental arrangement for the solid oxide fuel cell performance test.

Anode supported BZCYYb fuel cells were prepared for the electrochemical property measurements. The anode substrate containing NiO (J.T. Baker, 99%),

BZCYYb and graphite (Alfa Aesar, 99.8%) with weight ratio of 3:2:1 was fabricated by die pressing at 100 MPa, followed by adding BZCYYb powder to the anode substrate and co-pressing the BZCYYb electrolyte powder onto the anode substrates at 300 MPa to form anode-electrolyte bi-layers [134]. Two-step sintering method with the same sintering profile as the two-step sintered BZCYYb pellets (discussed in Chapter 3) was used to sinter the anode-electrolyte bi-layer. The anode supported half cells were heated at $5^oC\ min^{-1}$ to 600^oC and held for 2 h to remove the organic PVA bonder, followed by heating at a rate of $5^oC\ min^{-1}$ to a peak temperature at 1450^oC and held for 1 min to achieve an intermediate density, then cooled at $15^oC\ min^{-1}$ to 1300^oC and held for 20 h, during which the ceramic densification was achieved while grain growth was suppressed. $Ba_{0.9}Co_{0.7}Fe_{0.2}Nb_{0.1}O_{3-\delta}$ (BCFN) cathode ink [135] was prepared by ball-milling BCFN powders with V-006 organic solvent (Heraeus Materials, Germany) and then pasted on the BZCYYb electrolyte surface of the sintered NiO-BZCYYb bi-layers, followed by firing at 1000 ℃ for 2 h to form single cells. The two-step sintered anode supported BZCYYb single cells with the configuration of Ni-BZCYYb|BZCYYb|BCFN were sealed on alumina tubes by a ceramic bond (Ceramabond^{TM} 552, Aremco Products Inc.). Single cells were tested with hydrogen (3vol% H_2O) as the fuel with a flow rate of 40 mL min^{-1} and ambient air as the oxidant. Fig. 5.1 shows the schematic of the testing facility for the single cells. The cells were first stabilized at 750^oC to allow the fully reduction of NiO to Ni. Cell current and voltage characteristics were evaluated by a Versa STAT3-400 electrochemical station in the temperature range of 600-750 ℃. AC impedance spectra were measured under open circuit conditions with A.C. amplitude of 10mV in the frequency range from 0.1 Hz to 1 MHz. The cross-section images of the single cells after

electrochemical tests were taken using a field emission scanning electron microscopy (FESEM, Zeiss Ultra). The conventional sintered anode supported BZCYYb single cells with the same configuration were also tested for comparison. For BCN18 based fuel cell fabrication, powder samples of $Ba_3Ca_{1.18}Nb_{1.82}O_{9-\delta}$ (BCN) electrolyte were prepared by conventional solid state reaction method. Pure BCN18 powder was finally obtained after calcination at 1200^oC for 5 h in air with a heating rate of 3^oC min^{-1}. NiO-$BaZr_{0.1}Ce_{0.7}Y_{0.1}Yb_{0.1}O_{3-\delta}$ composite was adopted as the anode and $Ba_{0.9}Co_{0.7}Fe_{0.2}Nb_{0.1}O_{3-\delta}$ was chosen as the cathode material. The same co-sintering profile and characterization methods were applied to NiO-BZCYYb|BCN18|BCFN fuel cells.

5.3 BZCYYB BASED PROTON CONDUCTING SOFCS

The cross-sectional images of the single cell fabricated by two-step sintering method after electrochemical measurements are presented in Fig. 5.2(a-c). Fig. 5-2(d) shows the cross-sectional image of a single cell via conventional sintering method as a comparison. For both methods, the electrodes are well bonded to the electrolyte membranes. As shown in Fig. 5.2(a), for the cells fabricated by the two-step sintering method, the electrolyte is around 15 μm thick, with average grain sizes of 0.5 μm, compared to grains larger than 5 μm for the electrolyte sintered via conventional sintering method. The anode particles shown in Fig. 5.2(b) are also much smaller than those via the conventional sintering method (shown in Fig. 5.2(d) anode), advantageous to increase the triple-phase boundary (TPB) sites in the anode, where the electrochemical reaction occurs to produce protons [136].

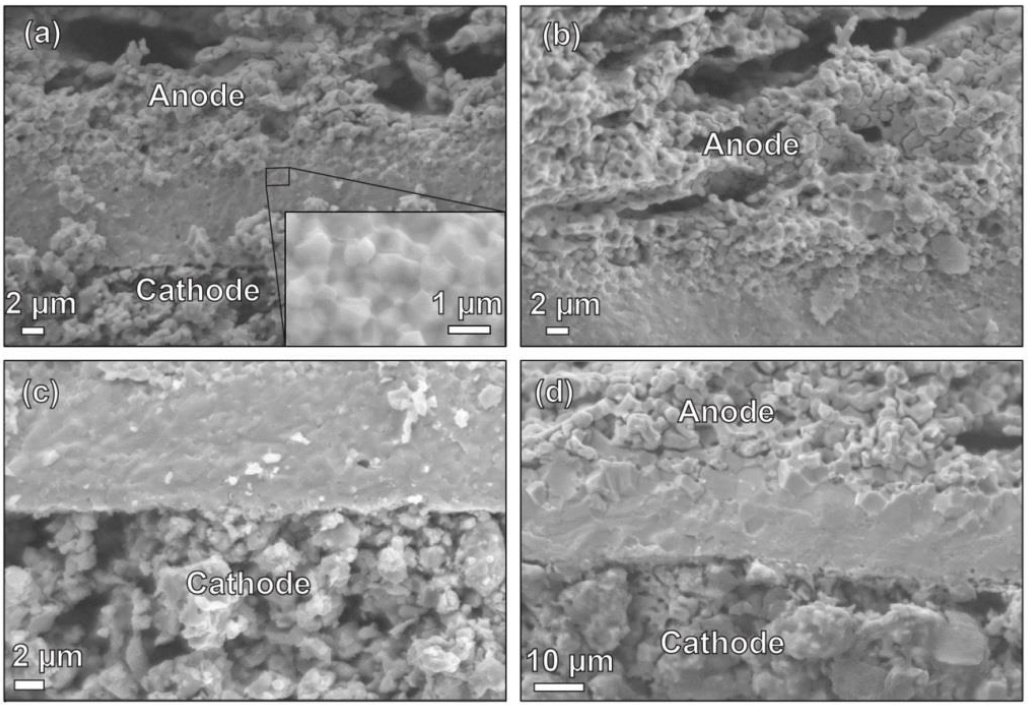

Figure 5.2 Cross-sectional FESEM images of post-tested Ni-BZCYYb|BZCYYb|BCFN SOFC fabricated via two-step sintering method: (a) single cell, (b) anode-electrolyte interface, (c) cathode-electrolyte interface, and (d) single cell fabricated via conventional sintering method.

Fig. 5.3 shows the I-V curves and power densities of the BZCYYb cell fabricated by two-step sintering method. Maximum power densities of 193, 273, 349, and 418 mW cm^{-2} with the open circuit voltage (OCV) values of 1.05, 1.03, 1.0 and 0.97 V were obtained at 600, 650, 700 and 750^{o}C, respectively. The OCV values are consistent with the reported data indicative of the formation of sufficiently dense and gas tight electrolyte membrane [59, 137]. Fig. 5.4 shows the impedance spectra of the cell measured under open circuit conditions. The ohmic resistance (R_o) of the cell was determined from the intercept of the spectra with the real axis at high frequency while the total cell resistance (R_t) was determined by the intercept at low frequency. The polarization resistance (R_p) is

determined by subtraction of the cell ohmic resistance from total cell resistance. The R_o, R_p and R_t values and their ratios are presented in Table 5.1. The increase of the measuring temperature resulted in a significant reduction of both the R_o and R_p. From R_o/R_t and R_p/R_t it can be seen that at temperatures higher than 700^{o}C the performance is strongly affected by the ohmic resistance, while at lower temperatures (such as 600^{o}C) the cell performance is limited by both ohmic and polarization resistances. The area specific resistance (ASR) contributed from the 15 μm BZCYYb electrolyte can be calculated based on the conductivity results through the equation ASR=L/σ, where L = 15×10^{-4} cm, σ is taken from the conductivity results (where we chose the lower conductivity value between σ_{air} and σ_{H_2}). The ASRs at different temperatures are also presented in Table 5.1. It can be seen that the ASR is about one order of magnitude smaller than the cell ohmic resistance, suggesting that the contact resistance between the electrolyte and the electrode dominates the total cell ohmic resistance. Thus to obtain a higher cell performance at intermediate temperature range, resolving the contact resistance is critical.

Table 5.1 The ohmic resistance R_o, polarization resistance R_p, total resistance R_t, and their ratios obtained from the impedance spectra for Ni-BZCYYb|BZCYYb|BCFN single cell by two-step sintering method.

Temperature (^{o}C)	**R_o (Ω cm^2)**	**R_p (Ω cm^2)**	**R_t (Ω cm^2)**	**R_o/R_t**	**R_p/R_t**
600	0.73	0.76	1.49	49.0%	51.0%
650	0.59	0.27	0.86	68.6%	31.4%
700	0.51	0.11	0.62	82.3%	17.7%
750	0.45	0.05	0.50	90.0%	10.0%

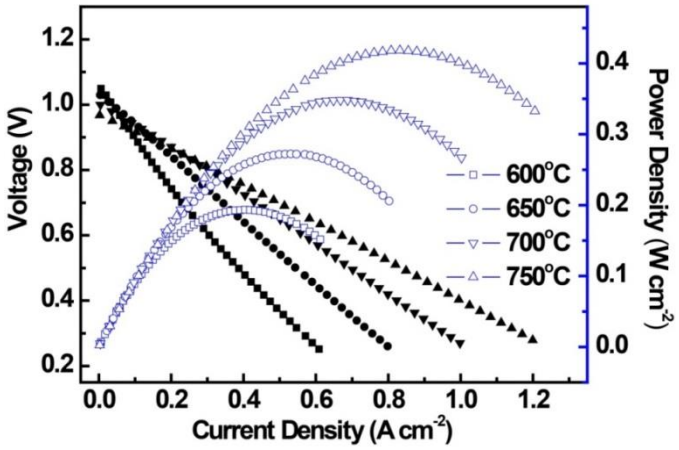

Figure 5.3 Cell voltage and power density as a function of current density for Ni-BZCYYb|BZCYYb|BCFN single cell via two-step sintering method.

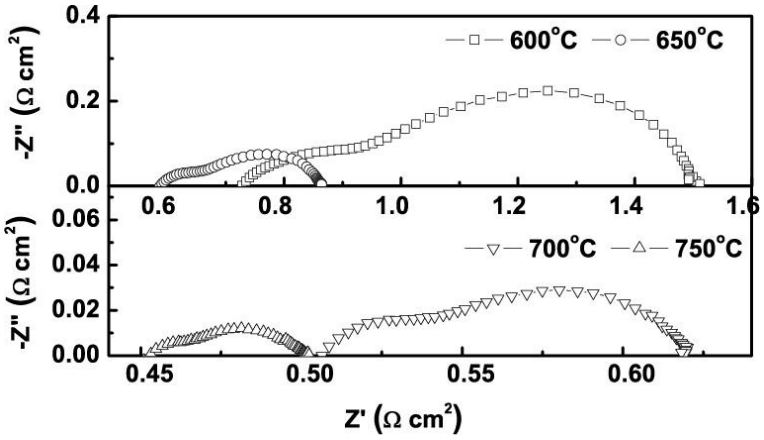

Figure 5.4 Impedance spectra and resistances under open-circuit conditions of the single cell via two-step sintering method.

Fig. 5.5(a) shows the cell voltage and power output for BZCYYb samples sintered via two-step sintering and conventional sintering methods at 700°C. Cell impedance spectra under open-circuit conditions are shown in Fig. 10(b). The open circuit voltages are around 1.0 V for both samples, while the maximum power output for BZCYYb

sample sintered via two-step sintering is much higher than that via conventional sintering. For the cell prepared by two-step sintering, on one hand, the electrolyte membrane is thinner, on the other, the conductivity of the electrolyte itself is higher. The conductivities of the electrolyte films under fuel cell operation conditions were calculated to eliminate the effect of electrolyte thickness. Assuming the ohmic resistance is caused solely by electrolyte resistance, the BZCYYb electrolyte membrane in the cell via two-step sintering exhibited a conductivity of 0.0029 S cm^{-1}, compared with 0.0022 S cm^{-1} for the membrane in the cell prepared via conventional sintering. The conductivity is not directly comparable with that in conductivity measurement environment since we neglect the contact resistance, but it still suggests that enhanced electrolyte conductivity can be achieved via two-step sintering in fuel cell conditions, which is consistent with the conductivity results in this study. Overall, the two-step sintering method is a simple and effective way to fabricate Ni-based anode-supported proton conducting BZCYYb fuel cells with enhanced electrochemical performances.

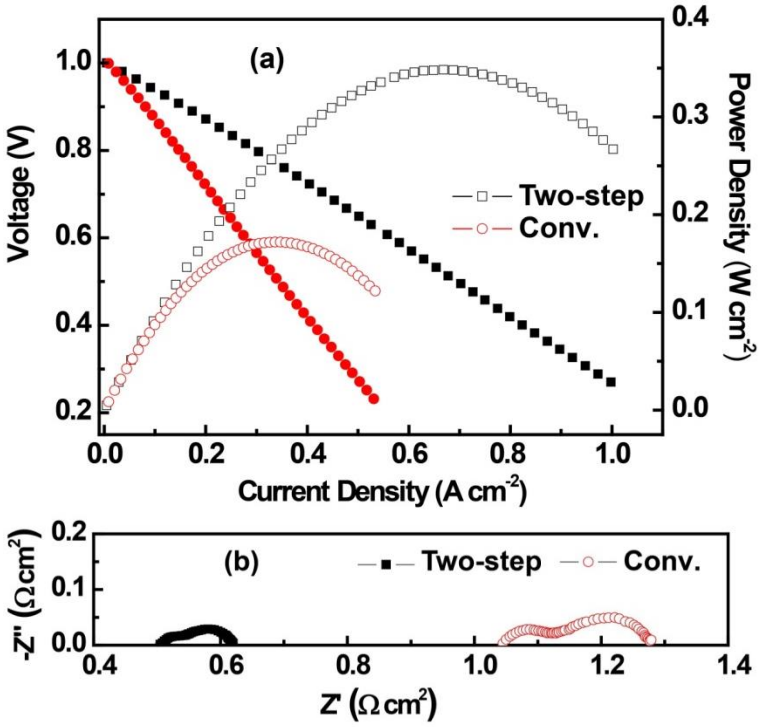

Figure 5.5 (a) Comparison of cell voltage and power density at 700^{o}C for Ni-BZCYYb|BZCYYb|BCFN single cell via two-step sintering method (Two-step) and conventional sintering method (Conv.); (b) Comparison of Impedance spectra and resistances of the single cell under open-circuit conditions.

5.4 TWO-STEP CO-SINTERING METHOD TO FABRICATE ANODE-SUPPORTED $BA_3CA_{1.18}NB_{1.82}O_{9-\Delta}$ PROTON CONDUCTING SOLID OXIDE FUEL CELLS

5.4.1 Components compatibility test

To check the chemical compatibility between the electrolyte and the cathode, BCN18 and BCFN with weight ratio of 1:1 were mechanically mixed and heated to 1100^{o}C for 2 h. Fig. 5.6(a) shows the XRD patterns of BCN18 and BCFN and their mixture after heat treatment. No observable secondary peaks can be detected, implying that BCN18 and BCFN are chemically compatible during the fuel cell fabrication and testing processes. XRD patterns for the anode composite NiO-BZCYYb after co-sintering

at 1400^{o}C for 5 h exhibit predominantly NiO and BZCYYb phases, while minor peaks corresponding to $BaNiO_x$ secondary phase are found, as shown in Fig. 5.6(b), indicating that trace amount of BaO-NiO solid solution might be formed during the high temperature co-sintering process [137]. A NiO-BCN18 composite was not chosen as the anode since CaO in BCN18 reacts with NiO to form CaO-NiO solid solutions at the co-sintering temperatures [138, 139]. In BCN18 ($Ba_3Ca_{1.18}Nb_{1.82}O_{9-\delta}$), the inclusion of extra CaO results in oxygen vacancies and thus enhanced ionic conductivity for the material [28]. The solid solution of CaO-NiO formed in the anode will thus be detrimental to the electrical conductivity of BCN18 in the anode due to the loss of CaO. The overall electrochemical performance for fuel cells with NiO-BCN18 as an anode might not be as good as the NiO-BZCYYb materials system. To confirm this, a NiO-BCN18 composite was sintered at 1400^{o}C for 5h and the back-scattered electron (BSE) image and spot scan of the EDS patterns for the grains were taken. Two phases were clearly formed as shown in Fig. 5.7(a). However, nickel peaks can be found from the spot scan of EDS patterns for the ceramics phases ("light" grains in the BSE images) as shown in Fig. 5.7(b), indicating that NiO dissolved into BCN18. EDS patterns for nickel phases ("dark" grains in the BSE images) shown in Fig. 5.7(c) also suggest that trace amount of BaO and CaO dissolved into NiO. NiO-BCN18|BCN18|BCFN fuel cells were fabricated and showed a fairly low power output of 46 mW cm^{-2} at 700^{o}C, similar to the reported data [140], mainly due to the relatively large ohmic resistance (shown in Fig. 5.8).

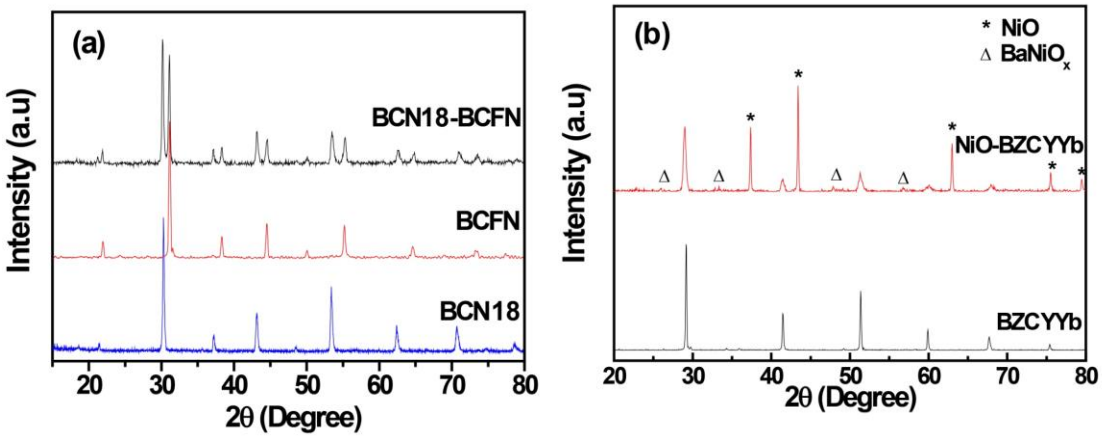

Figure 5.6 XRD patterns for (a) BCN18 electrolyte, BCFN cathode and BCN18-BCFN powder mixture heated at 1100^{o}C for 2 h; (b) BZCYYb, and NiO-BZCYYb powder mixture heated at 1400^{o}C for 5 h.

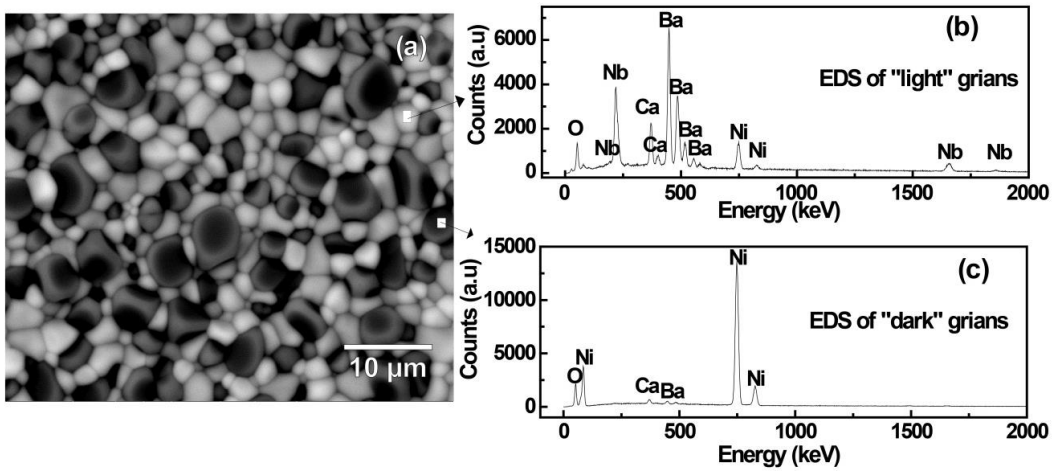

Figure 5.7 Back-scattered Electron (BSE) image of NiO-BCN18 composite sintered at 1400^{o}C for 5 h, EDS pattern of "light" grains (b) and "dark" grains (c).

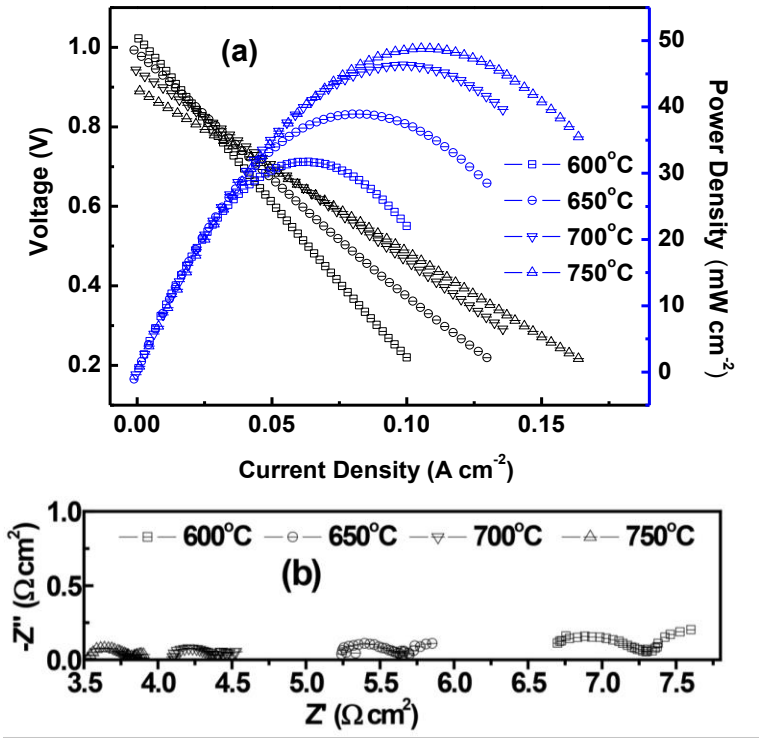

Figure 5.8 (a) Cell voltage and power density as a function of current density for Ni-BCN18|BCN18|BCFN single cell fabricated by conventional sintering method at 1400°C for 5h, and (b) impedance spectra of the single cell under open-circuit conditions.

Shown in Fig. 5.9(a) is the I-V curves and power density of the BCN18 cell fabricated by TS-CS method at different temperatures. Maximum power densities of 56, 79, 97, and 106 mW cm^{-2} with open circuit voltage (OCV) values of 1.04, 1, 0.95 and 0.91V were obtained at 600, 650, 700 and 750°C, respectively. The OCV values are consistent with the reported data, indicating that the electrolyte membrane is sufficiently dense [140]. The OCV values are lower than Nernst potentials, especially at high temperatures, which is caused by the increased electronic conduction for the proton conducting BCN18 electrolyte membranes. With testing temperature increases, the electronic conductivity increases and can be understood through Equation (2-3) and (4-1). At high temperatures the electrolyte may show p-type conduction near cathode side and

n-type conduction near anode side. The maximum power output obtained in this study is more than doubled compared with those using BCN18 electrolyte fabricated by an *in-situ* method (48 mW cm^{-2} at 700^{o}C) [140]. The significantly enhanced cell performance is attributed to the adoption of the TS-CS method to lower the co-sintering temperature as well as judicious choice of anode configuration. This processes resulted in dense, fine-grained electrolyte membranes, combined with an anode composite with small particles and high porosity, resulting in a significant reduction in the ohmic polarization resistance. Fig. 5.9(b) shows the electrochemical impedance spectra of the cell measured under open-circuit conditions at different testing temperatures. The R_o, R_p and R_t obtained from the impedance spectra are plotted in Fig. 5.9(c) and summarized in Table 5.2. The increase in the testing temperature resulted in a significant reduction of both the R_o and R_p, with the ratio of R_o to R_t increased from 78.7% to 92.5% (See Table 5.2), implying that the performance of the cell is strongly limited by the ohmic resistance. The area specific ohmic resistance (ASR) contributed from the 25 μm thick BCN18 electrolyte membrane can be estimated based on the conductivity results where $\sigma=2\times10^{-3}$ S cm^{-2} at 600^{o}C in air [92]. The expected ohmic resistance from the electrolyte membrane is 1.25 Ω cm^2 at 600^{o}C, compared with 3.74 Ω cm^2 of the R_o obtained from the impedance spectra. It seems that ohmic resistance of the electrodes and contact resistance between the electrolyte and the electrode still plays an important role in the total cell ohmic resistance. Furthermore, the relative low polarization resistance indicates that BCFN may be a suitable cathode candidate for intermediate temperature SOFCs with BCN18 proton conducting electrolytes. Further enhancements in cell performance can be expected by

preparing chemical compatible electrodes with the electrolyte or utilizing electrolyte membranes with high proton conductivity such as rare-earth element doped BCN18 [92].

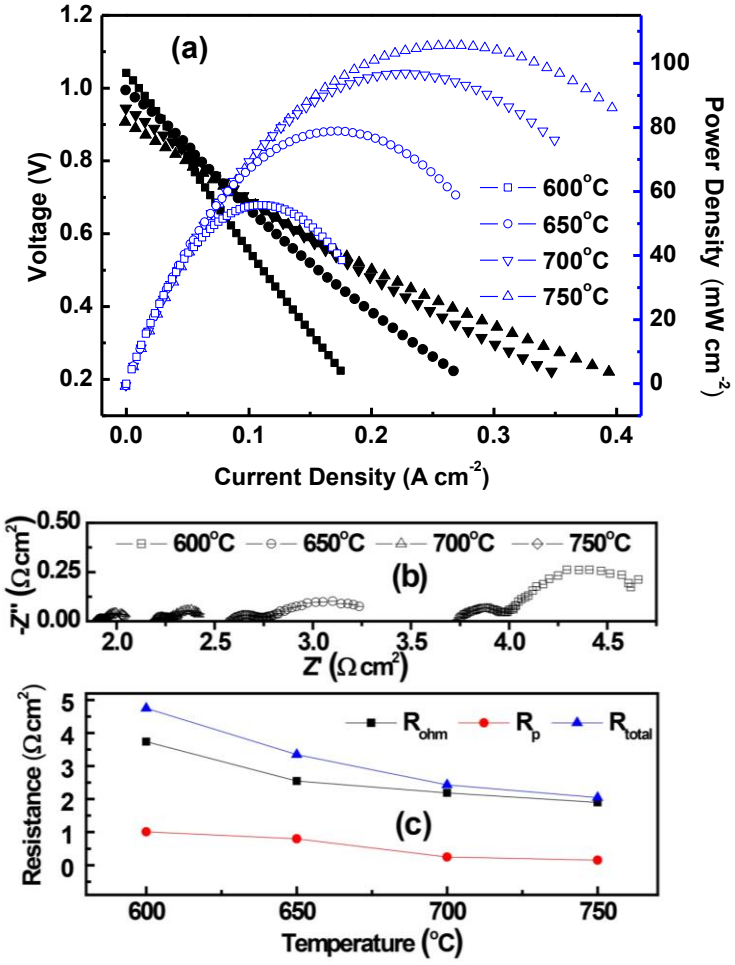

Figure 5.9 Cell voltage and power density as a function of current density for Ni-BZCYYb|BCN18|BCFN single cell at different temperatures, and Impedance spectra and resistances of the single cell under open-circuit conditions: (b) impedance spectra of the single cell at different temperatures, and (c) the ohmic resistance (R_{ohm}), the polarization resistance (R_p) and the total resistance (R_{total}) of the cell as a function of operating temperature.

Table 5.2 The ohmic resistance R_o, polarization resistance R_p and total resistance R_t obtained from the impedance spectra and their ratios.

Temperature (^oC)	**R_o (Ω cm^2)**	**R_p (Ω cm^2)**	**R_t (Ω cm^2)**	**R_o/R_t**	**R_p/R_t**
600	3.74	1.01	4.75	78.7%	21.3%
650	2.55	0.80	3.35	76.1%	23.9%
700	2.19	0.24	2.43	89.9%	9.9%
750	1.90	0.15	2.05	92.5%	7.3%

5.5 AFTER PERFORMANCE MICROSTRUCTURAL EVOLUTION

The cross-sectional images of the single cell after electrochemical measurements are shown in Fig. 5.10(a-c). The electrolyte-anode interface sintered by the conventional sintering method at 1400^{o}C for 5h is also shown in Fig. 5.10(d) for comparison. It can be seen that the electrodes are well adhered to the electrolyte membrane and there are no apparent cracks in the dense BCN18 electrolyte membrane fabricated by the TS-CS method. Compared with the conventional sintering process (Fig. 5.10(d)), the BCN18 electrolyte grains from the TS-CS method are much finer, characteristic of a "frozen" microstructure observed in a two-step sintering process due to the diffusion of grain boundaries without grain boundary migration [83, 85]. Similar to the electrolyte, the anode particles derived from the TS-CS method are much smaller than those from the conventional sintering method. By avoiding Ni-coarsening during the sintering process, the finer anode microstructure obtainable from TS-CS method is advantageous to the cell electrochemical performance due to increased number of the triple phase boundary (TPB) sites in the anode. Selected elemental distributions of the electrolyte-anode interface are shown in Fig. 5.11 through EDS mapping. It can be seen that the element distributions

are homogeneous in confined areas, with Ba distributed in both anode and electrolyte, Ca and Nb only distributed in electrolyte, and Ni constrained only in the anode side, indicating that no elemental diffusions happened during the fuel cell tests. It should be noted that the BCN18 electrolyte membrane fabricated by dry-pressing in the study (about 25 μm in thickness) is about 10 μm thicker than those prepared by an *in-situ* method [140]. Considering the reduced co-sintering temperature combined with 100% improvement in cell output power density, this TS-CS method has demonstrated great potential for the fabrication of anode-supported SOFCs with lower sintering temperatures and higher cell performance.

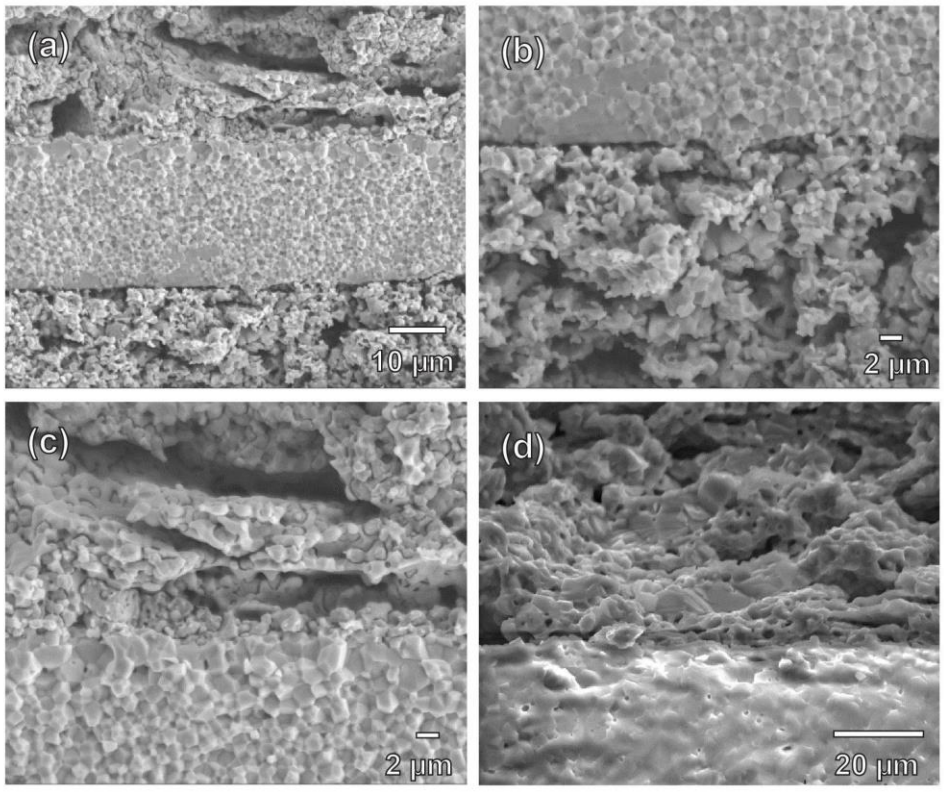

Figure 5.10 Cross-sectional SEM images of post-tested Ni-BZCYYb|BCN18|BCFN SOFC fabricated by two-step co-sintering method: (a) single cell, (b) electrolyte-cathode interface, (c) electrolyte-anode interface, and (d) electrolyte-anode interface sintered by conventional sintering method.

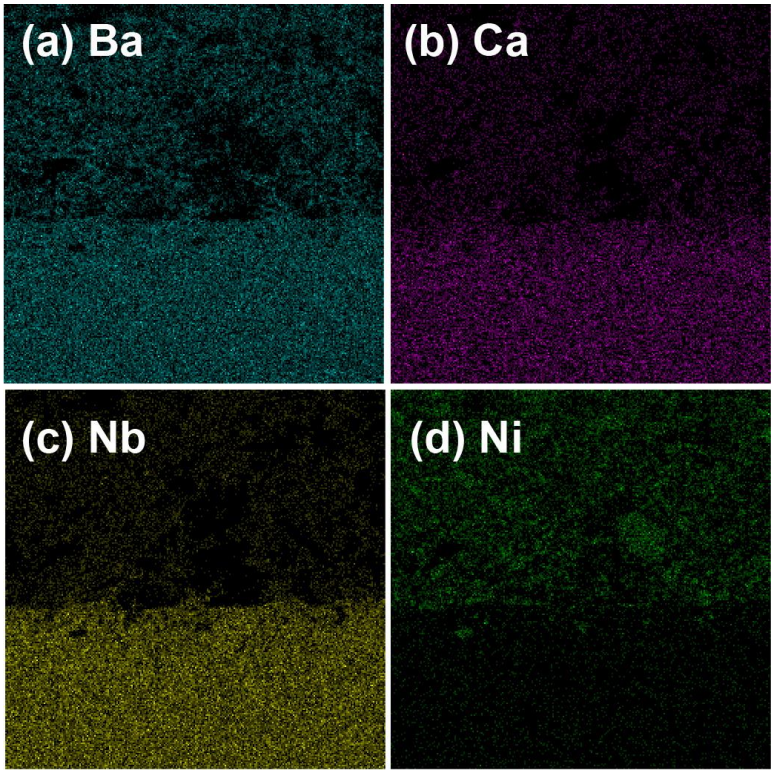

Figure 5.11 EDS elemental mapping of the electrolyte-anode interface for Ni-BZCYYb|BCN18|BCFN SOFC: (a) Ba, (b) Ca, (c) Nb, (d) Ni.

5.6 SUMMARY

Two-step sintering method was examined on BZCYYb proton conducting ceramic and ultrafine grained dense BZCYYb proton conductor was successfully prepared with a holding temperature of 1300^{o}C for 20h. Higher sinterability was observed from the dilatometric study for samples sintered via two-step sintering method. Increased conductivity, as well as lower ohmic resistance and enhanced cell power output was obtained for anode supported solid oxide fuel cells using BZCYYb as the electrolyte in which the anode and electrolyte bi-layers were fabricated from two-step sintering method compared with those from the conventional sintering method. $Ba_3Ca_{1.18}Nb_{1.82}O_{9-\delta}$

(BCN18) proton conductor based SOFC has been successfully fabricated by the two-step sintering method. This method lowered the co-sintering temperature of the anode-electrolyte bi-layer, restricted the grain growth of the particles to obtain fine-grained dense electrolyte and ultrafine anode particles with high porosity. The BCN18 based SOFCs, combined with proper electrode materials, demonstrates the highest ever maximum power densities for these materials. The two-step co-sintering method therefore shows great potential and deserves further study for the fabrication of other anode supported SOFC systems with optimized sintering profiles for improved electrochemical performance.

CHAPTER 6

CONCLUSIONS AND RECOMMENDATIONS

6.1 CONCLUSIONS

In this thesis, several types of high temperature proton conducting ceramics have been synthesized via different methods, and systematically investigated to understand their electrical properties, chemical stabilities, as well as the feasibility applied as electrolyte membranes for solid oxide fuel cells.

To overcome the conductivity-stability compromise issue, several strategies has been applied and have been evaluated such as the A site doping and B site co-doping method for simple perovskite structured $BaCeO_3$ based proton conductors, as well as the development of novel complex perovskite structured $BaCa_{1.18}Nb_{1.82}O_{9-\delta}$ based proton conductors.

A site Sr doping for $Ba_{1-x}Sr_xCe_{0.8}Y_{0.2}O_{3-\delta}$ by modified Pechini method has been evaluated. Dense microstructures were achieved for all the samples upon sintering at 1500^oC for 5 h. The phase structure analysis indicated that perovskite phase was formed for $0 \leq x \leq 0.2$, while for x larger than 0.5, impurity phases of Sr_2CeO_4 and Y_2O_3 appeared. The tolerance to H_2O for the samples improved with the increase in Sr content when exposed to boiling water, while the electrical conductivity decreased from x=0 to 1. However, the resistance to CO_2 attack at elevated temperatures was not improved within the whole x range studied.

For $BaCe_{0.7}Zr_{0.1}Y_{0.1}Yb_{0.1}O_{3-\delta}$ prepared via modified Pechini method, Pure perovskite structured material has been obtained after calcining at temperatures T $\geq 1000^{o}C$. The microstructures of the samples sintered at different temperatures from 1350 to $1550^{o}C$ have been evaluated, revealing denser microstructures with higher sintering temperatures. The sample sintered at $1400^{o}C$ shows the highest conductivity, indicating that the beneficial effects on conductivity from denser samples is counteracted by the segregation of secondary phases in the grain boundaries at higher sintering temperatures. The thermal expansion coefficient (TEC) for $BaCe_{0.7}Zr_{0.1}Y_{0.1}Yb_{0.1}O_{3-\delta}$ is in the range of $9.1\text{-}9.8\times10^{-6}$ K^{-1} from 25 to $1200^{o}C$, favorably matched to that of Pr based perovskite cathode materials for SOFC applications.

Microstructural modification of $BaZr_{0.1}Ce_{0.7}Y_{0.1}Yb_{0.1}O_{3-\delta}$ prepared by co-precipitation method has also been studied via a novel two-step sintering method. Co-precipitation method has been adopted to prepare nano-sized BZCYYb precursors with an average particle size of 30 nm. By controlling the sintering profile, an average grain size of 184 nm was obtained for dense BZCYYb ceramics via the two-step sintering method, compared to 445 nm for the conventional sintered samples. The two-step sintered BZCYYb samples showed less impurity and an enhanced electrical conductivity compared with the conventional sintered ones.

The development of novel complex perovskite structured $BaCa_{1.18}Nb_{1.82}O_{9-\delta}$ based proton conductors has also been investigated. Ce and Y doped into $BaCa_{1.18}Nb_{1.82}O_{9-\delta}$ in different sites have been studied.

The effects of Ce doping on the Ca and Nb sites in complex perovskite $Ba_3Ca_{1.18}Nb_{1.82}O_{9-\delta}$ (BCN18) proton conductor have been evaluated. It has been found

that cerium ions can be doped into both the Ca and Nb sites to form a single-phase complex perovskite structure when the sintering temperature is 1550^{o}C. Ce ions substituted with Nb ions enhances the electrical conductivity, especially the grain boundary conductivity. The highest conductivity has been obtained for a composition of $Ba_3Ca_{1.18}Nb_{1.62}Ce_{0.2}O_{9-\delta}$. The chemical stability tests show that Ce-doped BCN18 samples remain impressive single phase after treated either in boiling water for 7 h or in pure CO_2 for 4 h at 700^{o}C.

For Y doped Complex-perovskite structured $Ba_3Ca_{1.18}Nb_{1.82-x}Y_xO_{9-\delta}$ prepared via solid state reaction method, the crystal structure as Fm-3m ordered perovskite structure and revealed the presence of oxygen vacancies in the as-synthesized materials. The doped Y are located at 4a site, with some of the Y ions replace the Ca ions, leading to trace amount of CaO secondary phase with the increase of doping content. The introduction of Y as a substitution for Nb increased oxygen vacancy concentration and moderated the degree of B-site cation ordering in the structure, which is associated with the ordering of oxygen vacancy. Such tuning of cation ordering led to improved proton conductivity for the Y doped materials, The materials showed remarkable chemical stability towards water and CO_2 and was found non-relevant with the doping level up to 30% Y doping. Open circuit voltage tests showed that $Ba_3Ca_{1.18}Nb_{1.52}Y_{0.3}O_{9-\delta}$ behaved as a predominantly proton conductor below 600^{o}C.

The two-step sintering method was applied to fabricate anode supported solid oxide fuel cells (SOFCs) using selected proton conductors as electrolyte materials. For two-step sintered SOFC with BZCYYb as the electrolyte, dense ultrafine-grained electrolyte membranes and porous anode substrates with fine particles has been obtained.

Due to the reduced ohmic as well as polarization resistances, the maximum power output of the cells fabricated from the two-step sintering method reached 349 mW m^{-2} at 700^{o}C, significantly improved from 172 mW cm^{-2} for the conventional sintered cells, suggesting that two-step sintering method is very promising for optimizing the microstructure and thus enhancing the electrochemical performances for barium cerate based proton-conducting SOFCs.

Anode-supported solid oxide fuel cells (SOFCs) based on complex-perovskite structured $Ba_3Ca_{1.18}Nb_{1.82}O_{9-\delta}$ (BCN18) proton conducting electrolyte membranes have been successfully fabricated by a novel two-step co-sintering method. Dense BCN18 electrolyte membranes with fine grain size have been obtained by a novel two-step co-sintering method at a relatively low sintering temperature of 1300^{o}C, compared to the typical high sintering temperature of 1550^{o}C. Furthermore, the Ni-$BaZr_{0.1}Ce_{0.7}Y_{0.1}Yb_{0.1}O_{3-\delta}$ anode obtained by the novel two-step co-sintering method was composed of small particles with high porosity which is advantageous for electrode performance. Single fuel cells using BCN18 as the electrolyte, Ni-$BaZr_{0.1}Ce_{0.7}Y_{0.1}Yb_{0.1}O_{3-\delta}$ as anode and $Ba_{0.9}Co_{0.7}Fe_{0.2}Nb_{0.1}O_{3-\delta}$ as cathode demonstrated a power density of 106 mW cm^{-2} at 750^{o}C, the best fuel cell performance ever reported for the BCN18 electrolyte.

Y doped $Ba_3Ca_{1.18}Nb_{1.52}Y_{0.3}O_{9-\delta}$ has also been demonstrated for single fuel cell application performed as electrolyte membrane. Single cell demonstrated an electrochemical performance of 103 mW cm^{-2} at 750^{o}C with a voltage of 0.47 V under a current of 220 mA, showing that Y doped $Ba_3Ca_{1.18}Nb_{1.82}O_{9-\delta}$ are promising proton conducting ceramics that possesses both superb chemical stability and enhanced proton

conductivity. Although the demonstrated power output is not high enough compared with other state-of-the-art solid oxide fuel cell systems, such doping strategy illustrates a direction for searching novel proton conducting ceramics to be applied as intermediate temperature devices and facilities.

Above all, although significant progress and extensive knowledge have been achieved, further exploration on novel high temperature proton conductors with high proton conductivity and enhanced chemical stability are still urgently needed for effective hydrogen separation and intermediate temperature solid oxide fuel cells. The search for novel proton conducting ceramics that possess both high proton conductivity and chemical stability will never stop.

6.2 RECOMMENDATIONS

6.2.1 Electrolysis study of proton conducting ceramics

Electrolysis for hydrogen production for proton conducting oxides has been proposed as early as the discovery of proton conducting oxides [1]. However, the development of electrolysis based on proton conducting ceramics is rarely seen until recently due to the development of $BaZrO_3$ based SOFCs when the sintering behavior of $BaZrO_3$ has been greatly improved. First of all, the sintering temperature has been reduced from 1700~1800^oC down to ~1500^oC with the application of sintering aid or reactive sintering method [2, 3], at the same time, the grain growth of the $BaZrO_3$ based proton conductors has been largely improved, leading to higher grain boundary conductivity and the consequent improved total conductivity. The $BaZrO_3$ based proton conducting solid oxide fuel cells are fabricated and a peak power density can be achieved

as high as 360 mW cm^{-2} at 700^{o}C by an anode supported $BaZr_{0.7}Sn_{0.1}Y_{0.2}O_{3-\delta}$ proton conductor [57].

Based on these results, it is thus feasible to fabricate proton conducting solid oxide electrolysis cells for the production of hydrogen. Compared with oxide ion conductors applied for the electrolysis, the proton conductor electrolysis has the advantage that pure hydrogen is produced at the hydrogen electrode, without the dilution problems and do not need to further purification. On the other hand, based on the fuel cell performance for the proton conductor solid oxide fuel cells, it is anticipated that the operating temperature of the electrolysis will be lower than the oxide ion electrolysis process, which will save the cost and be beneficial for the long term stability.

6.2.2 Investigation of thin film based proton conducting oxides

Thin film based proton conductors has been recently attracted more and more attention since from the basic science point of view, if one would like to investigate the bulk conductivity of the materials, single crystal based thin films can be prepared via thin film forms to avoid the existence of grain boundaries. For example, in 2010, Traversa's group prepared epitaxial oriented $BaZr_{0.8}Y_{0.2}O_{3-\delta}$ and a proton conductivity of 0.11 S cm^{-1} at 500^{o}C has been obtained for the thin film without grain boundaries [5]. Actually back to 2008 the $BaZr_{0.8}Y_{0.2}O_{3-\delta}$ epitaxially grown on MgO(100) has been studied at lower temperature and a bulk conductivity of around 0.001 S cm^{-1} at around 250^{o}C has been obtained [6]. The results for other systems, however, are rarely seen. On the other hand, the role grain boundary plays in the thin films are seldom investigated since the grain boundary plays a detrimental influence for the total conductivity. However, by carefully

controlling the grain growth and the electrode surface areas for the thin film based proton conducting ceramic oxide, the direct and quantitative contribution of the grain boundary to the total conductivity can be elucidated.

For above reasons, it is recommended that the investigation on thin film based proton conductors, such as $BaCe_{0.8}Y_{0.2}O_{3-\delta}$ based proton conductors, and the BCN18 based proton conductors, to prepare oriented thin film proton conductors which eliminate the grain boundary contributions, the understanding of the bulk and grain boundary conductions to the total conductivity, as well as the solid oxide fuel cell application of the thin film based proton conductors, are promising directions.

REFERENCES

[1] K.D. Kreuer, Annu. Rev. Mater. Res., 33 (2003) 333-359.

[2] H. Iwahara, H. Uchida, N. Maeda, J. Power Sources, 7 (1982) 293-301.

[3] K. Nomura, H. Kageyama, Solid State Ionics, 178 (2007) 661-665.

[4] E. Fabbri, A. D'Epifanio, E. Di Bartolomeo, S. Licoccia, E. Traversa, Solid State Ionics, 179 (2008) 558-564.

[5] Y.M. Chiang, E.B. Lavik, I. Kosacki, H.L. Tuller, J.Y. Ying, App. Phys. Lett., 69 (1996) 185-187.

[6] M.H. Fathi, M. Kharaziha, Mater. Lett., 63 (2009) 1455-1458.

[7] W. Puin, S. Rodewald, R. Ramlau, P. Heitjans, J. Maier, Solid State Ionics, 131 (2000) 159-164.

[8] K.D. Kreuer, Solid State Ionics, 97 (1997) 1-15.

[9] P. Choi, N.H. Jalani, R. Datta, J. Electrochem. Soc., 152 (2005) E84-E89.

[10] S.M. Haile, D.A. Boysen, C.R.I. Chisholm, R.B. Merle, Nature, 410 (2001) 910-913.

[11] D.A. Boysen, T. Uda, C.R.I. Chisholm, S.M. Haile, Science, 303 (2004) 68-70.

[12] http://addis.caltech.edu/research/solacids.html.

[13] T. Scherban, A.S. Nowick, Solid State Ionics, 53-56 (1992) 1004-1008.

[14] K. Koto, M. Itai, C. Numako, Solid State Ionics, 154-155 (2002) 741-748.

[15] F. Chen, O.T. Sorensen, G. Meng, D. Peng, J. Mater. Chem., 7 (1997) 481-485.

[16] R. Peng, Y. Wu, L. Yang, Z. Mao, Solid State Ionics, 177 (2006) 389-393.

[17] F. Zhao, Q. Liu, S. Wang, K. Brinkman, F. Chen, Int. J. Hydrogen Energy, 35 (2010) 4258-4263.

[18] Z. Wu, M. Liu, J. Electrochem. Soc., 144 (1997) 2170-2175.

[19] J. Wang, L. Li, B.J. Campbell, Z. Lv, Y. Ji, Y.F. Xue, W.H. Su, Mater. Chem. Phys., 86 (2004) 150-155.

[20] S. Yamaguchi, N. Yamada, Solid State Ionics, 162-163 (2003) 23-29.

[21] K. Künstler, H.J. Lang, A. Maiwald, G. Tomandl, Solid State Ionics, 107 (1998) 221-229.

[22] F. Giannici, A. Longo, F. Deganello, A. Balerna, A.S. Arico, A. Martorana, Solid State Ionics, 178 (2007) 587-591.

[23] D.M. Giaquinta, H.-C. zur Loye, Chem. Mater., 6 (1994) 365-372.

[24] H.G. Bohn, T. Schober, T. Mono, W. Schilling, Solid State Ionics, 117 (1999) 219-228.

[25] D.J.D. Corcoran, J.T.S. Irvine, Solid State Ionics, 145 (2001) 307-313.

[26] H.D.A.L. Viana, J.T.S. Irvine, Solid State Ionics, 178 (2007) 717-722.

[27] K. Oikawa, T. Kamiyama, S. Ikeda, T. Shishido, S. Yamaguchi, Solid State Ionics, 154-155 (2002) 641-646.

[28] A.S. Nowick, Y. Du, Solid State Ionics, 77 (1995) 137-146.

[29] S. Valkenberg, H.G. Bohn, W. Schilling, Solid State Ionics, 97 (1997) 511-515.

[30] H.d.A.L. Viana, J.T.S. Irvine, J. Mater. Chem., 20 (2010) 8506-8511.

[31] Y. Du, A.S. Nowick, J Am. Ceram. Soc., 78 (1995) 3033-3039.

[32] A.S. Nowick, Y. Du, K.C. Liang, Solid State Ionics, 125 (1999) 303-311.

[33] I. Animitsa, A. Neiman, A. Sharafutdinov, S. Nochrin, Solid State Ionics, 136-137 (2000) 265-271.

[34] I. Animitsa, A. Nieman, S. Titova, N. Kochetova, E. Isaeva, A. Sharafutdinov, N. Timofeeva, P. Colomban, Solid State Ionics, 156 (2003) 95-102.

[35] L. Malavasi, C.A.J. Fisher, M.S. Islam, Chem. Soc. Rev., 39 (2010) 4370-4387.

[36] J.B. Goodenough, J.E. Ruiz-Diaz, Y.S. Zhen, Solid State Ionics, 44 (1990) 21-31.

[37] K. Kakinuma, A. Tomita, H. Yamamura, T. Atake, J. Mater. Sci., 41 (2006) 6435-6440.

[38] E. Quarez, S. Noirault, M.T. Caldes, O. Joubert, J. Power Sources, 195 (2010) 1136-1141.

[39] T. Norby, N. Christiansen, Solid State Ionics, 77 (1995) 240-243.

[40] R. Haugsrud, T. Norby, Nat. Mater., 5 (2006) 193-196.

[41] E. Kendrick, J. Kendrick, K.S. Knight, M.S. Islam, P.R. Slater, Nat. Mater., 6 (2007) 871-875.

[42] C. Zuo, S. Zha, M. Liu, M. Hatano, M. Uchiyama, Adv. Mater., 18 (2006) 3318-3320.

[43] E. Fabbri, I. Markus, L. Bi, D. Pergolesi, E. Traversa, Solid State Ionics, 202 (2011) 30-35.

[44] J.A. Kilner, R.J. Brook, Solid State Ionics, 6 (1982) 237-252.

[45] G. Ma, T. Shimura, H. Iwahara, Solid State Ionics, 110 (1998) 103-110.

[46] H. Iwahara, T. Esaka, H. Uchida, N. Maeda, Solid State Ionics, 3-4 (1981) 359-363.

[47] T. Higuchi, T. Tsukamoto, H. Matsumoto, T. Shimura, K. Yashiro, T. Kawada, J. Mizusaki, S. Shin, T. Hattori, Solid State Ionics, 176 (2005) 2967-2970.

[48] N. Taniguchi, K. Hatoh, J. Niikura, T. Gamo, H. Iwahara, Solid State Ionics, 53–56, Part 2 (1992) 998-1003.

[49] Y. Yamazaki, R. Hernandez-Sanchez, S.M. Haile, Chem. Mater., 21 (2009) 2755-2762.

[50] J. Tong, D. Clark, L. Bernau, M. Sanders, R. O'Hayre, J. Mater. Chem., 20 (2010) 6333-6341.

[51] J. Tong, D. Clark, M. Hoban, R. O'Hayre, Solid State Ionics, 181 (2010) 496-503.

[52] D. Pergolesi, E. Fabbri, A. D'Epifanio, E. Di Bartolomeo, A. Tebano, S. Sanna, S. Licoccia, G. Balestrino, E. Traversa, Nat. Mater., 9 (2010) 846-852.

[53] L. Bi, E. Fabbri, Z. Sun, E. Traversa, Energy Environ. Sci., 4 (2011) 409-412.

[54] K.H. Ryu, S.M. Haile, Solid State Ionics, 125 (1999) 355-367.

[55] J. Zhang, Z. Wen, J. Han, J. Wu, S. Huang, X. Zhu, J. Alloys Compd., 440 (2007) 270-275.

[56] Z. Zhong, Solid State Ionics, 178 (2007) 213-220.

[57] E. Fabbri, A. D'Epifanio, E. Di Bartolomeo, S. Licoccia, E. Traversa, Solid State Ionics, 179 (2008) 558-564.

[58] A.K. Azad, J.T.S. Irvine, Solid State Ionics, 178 (2007) 635-640.

[59] L. Yang, S. Wang, K. Blinn, M. Liu, Z. Liu, Z. Cheng, M. Liu, Science, 326 (2009) 126-129.

[60] K. Maca, V. Pouchly, P. Zalud, J. Eur. Ceram. Soc., 30 (2010) 583-589.

[61] L. An, A. Ito, T. Goto, J. Am. Ceram. Soc., 94 (2011) 695-698.

[62] K.H. Brosnan, G.L. Messing, D.K. Agrawal, J. Am. Ceram. Soc., 86 (2003) 1307-1312.

[63] K. Huang, R.S. Tichy, J.B. Goodenough, J. Am. Ceram. Soc., 81 (1998) 2565-2575.

[64] T. Yajima, H. Iwahara, H. Uchida, Solid State Ionics, 47 (1991) 117-124.

[65] I.M. Hung, H.W. Peng, S.L. Zheng, C.P. Lin, J.S. Wu, J. Power Sources, 193 (2009) 155-159.

[66] S.V. Bhide, A.V. Virkar, J. Electrochem. Soc., 146 (1999) 2038-2044.

[67] W. Zhou, R. Ran, Z.P. Shao, H. Gu, W. Jin, N. Xu, J. Power Sources, 174 (2007) 237-245.

[68] H. Iwahara, Solid State Ionics, 86–88, Part 1 (1996) 9-15.

[69] P. Pasierb, M. Wierzbicka, S. Komornicki, M. Rekas, J. Power Sources, 173 (2007) 681-687.

[70] N. Bonanos, K.S. Knight, B. Ellis, Solid State Ionics, 79 (1995) 161-170.

[71] D.A. Andersson, S.I. Simak, N.V. Skorodumova, I.A. Abrikosov, B. Johansson, PNAS, 103 (2006) 3518-3521.

[72] M.A. Azimova, S. McIntosh, Solid State Ionics, 180 (2009) 160-167.

[73] L. Bi, S. Zhang, S. Fang, Z. Tao, R. Peng, W. Liu, Electrochem. Commun., 10 (2008) 1598-1601.

[74] E. Fabbri, L. Bi, H. Tanaka, D. Pergolesi, E. Traversa, Adv. Funct. Mater., 21 (2011) 158-166.

[75] F. Chen, O.T. Sørensen, G. Meng, D. Peng, Solid State Ionics, 100 (1997) 63-72.

[76] K. Huang, M. Feng, J.B. Goodenough, J. Am. Ceram. Soc., 81 (1998) 357-362.

[77] D. Ding, L. Li, K. Feng, Z. Liu, C. Xia, J. Power Sources, 187 (2009) 400-402.

[78] T. Cai, Y. Zeng, W. Zhang, C. Guo, X. Yang, J. Power Sources, 195 (2009) 1308-1315.

[79] W. Wang, J. Liu, Y. Li, H. Wang, F. Zhang, G. Ma, Solid State Ionics, 181 (2010) 667-671.

[80] S. Wang, F. Zhao, L. Zhang, K. Brinkman, F. Chen, J. Alloys Compd., 506 (2010) 263-267.

[81] M.J. Scholten, J. Schoonman, J.C. van Miltenburg, H.A.J. Oonk, Solid State Ionics, 61 (1993) 83-91.

[82] M.A. Lourenço, G.G. Cunto, F.M. Figueiredo, J.R. Frade, Mater. Chem. Phys., 126 (2011) 262-271.

[83] I.-W. Chen, X.-H. Wang, Nature, 404 (2000) 168-171.

[84] Y.I. Lee, Y.W. Kim, M. Mitomo, D.Y. Kim, J. Am. Ceram. Soc., 86 (2003) 1803-1805.

[85] L. Zhang, F.L. Chen, C.R. Xia, Int. J. Hydrogen Energy, 35 (2010) 13262-13270.

[86] M. Mazaheri, Z.R. Hesabi, F. Golestani-Fard, S. Mollazadeh, S. Jafari, S.K. Sadrnezhaad, J. Am. Ceram. Soc., 92 (2009) 990-995.

[87] Z. Tian, X. Wang, S. Lee, K.H. Hur, L. Li, J. Am. Ceram. Soc., 94 (2011) 1119-1124.

[88] S. Barison, M. Battagliarin, T. Cavallin, L. Doubova, M. Fabrizio, C. Mortalo, S. Boldrini, L. Malavasi, R. Gerbasi, J. Mater. Chem., 18 (2008) 5120-5128.

[89] J.F. Shin, L. Hussey, A. Orera, P.R. Slater, Chem. Commun., 46 (2010) 4613-4615.

[90] Y. Du, A.S. Nowick, Solid State Ionics, 91 (1996) 85-91.

[91] S. Wang, J. Zhai, X. Chou, L. Zhang, X. Yao, Mater. Chem. Phys., 115 (2009) 200-203.

[92] S. Wang, F. Zhao, L. Zhang, K. Brinkman, F. Chen, J. Power Sources, 196 (2011) 7917-7923.

[93] J.T.S. Irvine, D.J.D. Corcoran, J. Canales-Vazquez, Solid State Ionics, 152-153 (2002) 749-757.

[94] J.T.S. Irvine, M.C. Verbraeken, H. Viana, A.K. Azad, I. Ahmed, S. Eriksson, The 15th International Conference on Solid State Protonic Conductors, (2010) Oral 09.

[95] J.T. Shiue, T.T. Fang, J. Am. Ceram. Soc., 87 (2004) 391-394.

[96] T. Schober, K. Szot, M. Barton, B. Kessler, U. Breuer, H.J. Penkalla, W. Speier, J. Solid State Chem., 149 (2000) 262-275.

[97] HSC Chemistry:Outokumpu Research Oy,Finland, www.outotec.com/hsc.

[98] J.H. Park, Y.S. Cho, K.B. Yi, S.S. Han, S.H. Cho, App. Surf. Sci., 256 (2010) 5528-5532.

[99] M. Ishimaru, Y. Hirotsu, M. Tang, J.A. Valdez, K.E. Sickafus, J. Appl. Phys., 102 (2007) 063532.

[100] X. Dong, S. Ma, K. Huang, F. Chen, Int. J. Hydrogen Energy, 37 (2012) 10866-10873.

[101] A.C. Tavares, M.I. da Silva Pereira, M.H. Mendonça, M.R. Nunes, F.M. Costa, C.M. Sá, J. Electroanal. Chem., 449 (1998) 91-100.

[102] R.S. Lubna, A. Bakhtyar, Z. Hao, W.G. Wang, Y.Q. Song, H.W. Zhang, S.I. Shah, J.Q. Xiao, J. Phys. Condens. Matter, 21 (2009) 486004.

[103] K. Katahira, Y. Kohchi, T. Shimura, H. Iwahara, Solid State Ionics, 138 (2000) 91-98.

[104] E. Fabbri, T.-k. Oh, S. Licoccia, E. Traversa, E.D. Wachsman, J. Electrochem. Soc., 156 (2009) B38-B45.

[105] N. Zakowsky, S. Williamson, J.T.S. Irvine, Solid State Ionics, 176 (2005) 3019-3026.

[106] J. Lv, L. Wang, D. Lei, H. Guo, R.V. Kumar, J. Alloys Compd., 467 (2009) 376-382.

[107] H. Fjeld, D.M. Kepaptsoglou, R. Haugsrud, T. Norby, Solid State Ionics, 181 (2009) 104-109.

[108] G.B. Hans, S. Tilman, J. Am. Ceram. Soc., 83 (2000) 768-772.

[109] P.K. Sekhar, E.L. Brosha, R. Mukundan, M.A. Nelson, D. Toracco, F.H. Garzon, Solid State Ionics, 181 (2010) 947-953.

[110] S.M. Haile, D.L. West, J. Campbell, J. Mater. Res., 13 (1998) 1576-1595.

[111] F. Iguchi, T. Tsurui, N. Sata, Y. Nagao, H. Yugami, Solid State Ionics, 180 (2009) 563-568.

[112] D. Shima, S.M. Haile, Solid State Ionics, 97 (1997) 443-455.

[113] T. Ohzeki, S. Hasegawa, M. Shimizu, T. Hashimoto, Solid State Ionics, 180 (2009) 1034-1039.

[114] R. Pflieger, M. Malki, Y. Guari, J. Larionova, A. Grandjean, J. Am. Ceram. Soc., 92 (2009) 1560-1566.

[115] Z. Sun, E. Fabbri, L. Bi, E. Traversa, J. Am. Ceram. Soc., 95 (2012) 627-635.

[116] X. Zhou, L. Liu, J. Zhen, S. Zhu, B. Li, K. Sun, P. Wang, J. Power Sources, 196 (2011) 5000-5006.

[117] S. Wang, F. Zhao, L. Zhang, F. Chen, Solid State Ionics, 213 (2012) 29-35.

[118] C. Kjølseth, H. Fjeld, Ø. Prytz, P.I. Dahl, C. Estournès, R. Haugsrud, T. Norby, Solid State Ionics, 181 (2010) 268-275.

[119] C.M. Fernandes, A. Castela, F.M. Figueiredo, J.R. Frade, Solid State Ionics, 193 (2011) 52-59.

[120] A.V. Kuzmin, V.P. Gorelov, B.T. Melekh, M. Glerup, F.W. Poulsen, Solid State Ionics, 162-163 (2003) 13-22.

[121] K.S. Knight, Solid State Ionics, 145 (2001) 275-294.

[122] M. Mori, Y. Hiei, N.M. Sammes, G.A. Tompsett, J. Electrochem. Soc., 147 (2000) 1295-1302.

[123] K. Huang, J.B. Goodenough, Solid Oxide Fuel Cell Technology: Principles, Performance and Operations, Woodhead Publishing Ltd., Cambridge, UK, 2009.

[124] Q. Xu, D. Huang, F. Zhang, W. Chen, M. Chen, H. Liu, J. Alloys Compd., 454 (2008) 460-465.

[125] F. Tietz, Ionics, 5 (1999) 129-139.

[126] T.T. Trinh, V. Thangadurai, Electrochim. Acta, 56 (2010) 227-234.

[127] V. Prashanth Kumar, Y.S. Reddy, P. Kistaiah, G. Prasad, C. Vishnuvardhan Reddy, Mater. Chem. Phys., 112 (2008) 711-718.

[128] H. Ullmann, N. Trofimenko, F. Tietz, D. Stöver, A. Ahmad-Khanlou, Solid State Ionics, 138 (2000) 79-90.

[129] Z. Liu, L. Cheng, M. Han, J. Power Sources, 196 (2011) 868-871.

[130] I. Kosacki, H.L. Tuller, Solid State Ionics, 80 (1995) 223-229.

[131] E. Fabbri, D. Pergolesi, E. Traversa, Chem. Soc. Rev., 39 (2010) 4355-4369.

[132] Y. Guo, Y. Lin, R. Ran, Z. Shao, J. Power Sources, 193 (2009) 400-407.

[133] X. Guo, R. Waser, Prog. Mater. Sci., 51 (2006) 151-210.

[134] F. Zhao, S. Wang, L. Dixon, F. Chen, J. Power Sources, 196 (2011) 7500-7504.

[135] Z. Yang, C. Yang, C. Jin, M. Han, F. Chen, Electrochem. Commun., 13 (2011) 882-885.

[136] Q. Liu, X. Dong, C. Yang, S. Ma, F. Chen, J. Power Sources, 195 (2010) 1543-1550.

[137] F. Zhao, C. Jin, C. Yang, S. Wang, F. Chen, J. Power Sources, 196 (2011) 688-691.

[138] D.E. Smith, T.Y. Tien, L.H. Van Vlack, J. Am. Ceram. Soc., 52 (1969) 459-460.

[139] V. Prostakova, J. Chen, E. Jak, S.A. Decterov, Calphad, 37 (2012) 1-10.

[140] L. Bi, S.Q. Zhang, S.M. Fang, L. Zhang, H.Y. Gao, G.Y. Meng, W. Liu, J. Am. Ceram. Soc., 91 (2008) 3806-3809.